Submitted to ApJS 2010 October 11; accepted 2011 April 18
Preprint typeset using LaTeX style emulateapj v. 08/13/06

PROPERTIES OF BULGELESS DISK GALAXIES. I. ATOMIC GAS

Linda C. Watson[1], Eva Schinnerer[2], Paul Martini[1,3], Torsten Böker[4], Ute Lisenfeld[5]

Submitted to ApJS 2010 October 11; accepted 2011 April 18

ABSTRACT

We study the neutral hydrogen properties of a sample of 20 bulgeless disk galaxies (Sd - Sdm Hubble types), an interesting class that can be used to constrain galaxy formation and evolution, especially the role of mergers versus internal processes. Our sample is composed of nearby (within 32 Mpc), moderately inclined galaxies that bracket the circular velocity of $120\,\mathrm{km\,s^{-1}}$, which has been found to be associated with a transition in dust scale heights in edge-on, late-type disks. Here we present H I channel maps, line profiles, and integrated intensity maps. We also derive kinematic parameters, including the circular velocity, from rotation curve analyses and calculate the integrated H I flux and H I mass for each galaxy in the sample. Three of the 20 galaxies in our sample have kinematically distinct outer components with major axes that differ by $30^\circ - 90^\circ$ from the main disk. These distinct outer components may be due to a recent interaction, which would be somewhat surprising because the disks do not contain bulges. We will use the data products and derived properties in subsequent investigations into star formation and secular evolution in bulgeless disks with circular velocities above and below $120\,\mathrm{km\,s^{-1}}$.

Subject headings: galaxies: ISM — galaxies: spiral — ISM: atoms — radio lines: galaxies

1. INTRODUCTION

The formation of disk galaxies has remained an interesting and unresolved question in galaxy evolution for many decades. The basic model is fairly clear: galaxies form in cold dark matter (CDM) halos through the dissipational collapse of gas (White & Rees 1978). However, disks formed in hydrodynamic simulations are generally too highly concentrated and possess both proportionally larger bulges and lower angular momentum than the disks observed in the local universe (Katz & Gunn 1991; Navarro & White 1994; Navarro & Steinmetz 2000). Recent simulations that include feedback and/or high gas fractions have produced disks that survive hierarchical assembly and more closely resemble observed disk galaxies (Abadi et al. 2003; Robertson et al. 2006; Brook et al. 2011), but still some properties of the modeled disks do not match observed values. A coupled problem is that the merger rate in CDM models may be too high for many disk-dominated galaxies to survive to the present day (Toth & Ostriker 1992), and yet observations show that these galaxies are common (e.g., Kautsch et al. 2006; Cameron et al. 2009; Kormendy et al. 2010).

Observations of bulgeless disks, including galaxies termed "flat" or "thin" when viewed edge-on, provide a particularly important benchmark for theories of disk galaxy evolution. Their structural homogeneity is valuable for the direct study of disk properties without the complications associated with removal of a bulge component. A common conception is that because bulges form due to mergers, bulgeless galaxies have evolved in isolation. This view may be changing as simulations are starting to form bulgeless galaxies with relatively rich merger histories (e.g., Robertson et al. 2006; Hopkins et al. 2009; Brook et al. 2011). Nonetheless, the space density of bulgeless galaxies provides a useful constraint on the role of mergers in galaxy formation. In addition, bulgeless disk galaxies are an excellent comparison sample to study secular evolution, that is the role of internal processes in the buildup of bulges (Kormendy & Kennicutt 2004). The properties of bulgeless disks, in comparison to their slightly earlier-type counterparts with pseudobulges, may shed new light on the key processes that drive secular evolution.

Bulgeless galaxies had historically been overlooked in many surveys because they are often relatively low surface brightness objects, but more recent work has begun to identify them in large numbers and demonstrate that these often faint objects are a natural continuation of the sequence of brighter, earlier-type spirals (Matthews & Gallagher 1997). The first large sample of these objects was part of the edge-on Flat Galaxy Catalog compiled by Karachentsev et al. (1993). Demographic studies of edge-on flat disks in the Sloan Digital Sky Survey by Kautsch et al. (2006) provided some of the first measurements of the frequency of these objects and found that on order 15% of all edge-on disk galaxies are thin, bulgeless disks. The demographics of these galaxies may prove to be a useful constraint on simulations of disk galaxy formation, particularly as the sophistication of simulations improves to include major and minor mergers in orbits derived from cosmological simulations (Stewart et al. 2008; Hopkins et al. 2008).

A subset of bulgeless, edge-on galaxies in the Flat Galaxy Catalog was studied in detail by Dalcanton & Bernstein (2000). One extremely interesting result to arise from this study was that less massive,

[1] Department of Astronomy, The Ohio State University, 140 West 18th Avenue, Columbus, OH 43210, USA; watson@astronomy.ohio-state.edu
[2] Max-Planck-Institut für Astronomie, Königstuhl 17, D-69117 Heidelberg, Germany
[3] Center for Cosmology and AstroParticle Physics, The Ohio State University, 191 West Woodruff Avenue, Columbus, OH 43210, USA
[4] European Space Agency, Department of RSSD, Keplerlaan 1, 2200 AG Noordwijk, The Netherlands
[5] Departamento de Física Teórica y del Cosmos, Universidad de Granada, Spain

slowly rotating bulgeless disks with $v_{circ} < 120\,km\,s^{-1}$ do not have the narrow dust lanes characteristic of both earlier-type spirals and more rapidly rotating bulgeless disks (Dalcanton et al. 2004). These authors conclude that disk stability, parametrized by a generalized Toomre Q parameter (Rafikov 2001), is the most important physical property in determining the dust scale height of a galaxy. The scale height of the cold interstellar medium (ISM), and therefore the dust, is set by the balance between the mass surface density of gas and stars in the disk and the velocity dispersion of those components. Dalcanton et al. (2004) postulated that this transition in the cold ISM may correlate with substantial changes in star formation efficiency, metallicity, and bulge formation. Other studies of bulgeless disks have attempted to measure the cold ISM directly, in particular the molecular component (Böker et al. 2003; Matthews et al. 2005). These studies found that late-type spirals follow the same relationships between molecular gas content, galaxy luminosity, and far-infrared luminosity as earlier-type spirals, which reinforces the conclusion that bulgeless disks fall on the end of a continuum of disk galaxy properties, rather than comprise a unique class.

The goal of our study is to investigate the properties of bulgeless disk galaxies as a function of circular velocity, yet with a moderately-inclined sample that is well suited to measurements of star formation rate (SFR) and gas surface densities, the presence of bulges, nuclear star clusters, and stellar bars, and precise kinematic measurements to estimate dynamical masses. Our analysis is based on a sample of 20 nearby Sd galaxies that bracket the $v_{circ} = 120\,km\,s^{-1}$ transition velocity observed by Dalcanton et al. (2004). In the present paper we describe H I observations of the complete sample and derive the circular velocity and atomic gas distribution of each galaxy. In L. Watson et al. (2011, in preparation), we will present an analysis of the star formation properties of this sample, which will draw on CO(1-0) observations from the Institut de Radioastronomie Millimétrique (IRAM) 30 m telescope, Hα data from the 2.4 m Hiltner Telescope of the MDM Observatory, and polycyclic aromatic hydrocarbon emission measured with the *Spitzer Space Telescope* Infrared Array Camera (IRAC). Subsequent papers will focus on the widths of the dust lanes seen in absorption in F606W images from either the Advanced Camera for Surveys (ACS) or Wide-Field Planetary Camera 2 instruments on the *Hubble Space Telescope* (*HST*) and the signposts of secular evolution, such as the presence of pseudobulges, nuclear star clusters, and large-scale stellar bars.

This paper is organized as follows: we present our sample in Section 2 and outline our data reduction method in Section 3. We present channel maps, integrated line profiles, integrated intensity maps, and rotation curve analyses in Section 4. We discuss objects with noteworthy morphology or evidence of interaction in Section 5 and conclude in Section 6.

2. SAMPLE SELECTION

To assemble our sample, we started with all late-type disk galaxies (types Scd to Sm) within about 30 Mpc. This is the maximum distance at which *HST* ACS can resolve features of about 20 pc, which is typical of dust structures in nearby, earlier-type spiral galaxies and molecular cloud scale heights in our Galaxy (Martini et al. 2003; Stark & Lee 2005). We also restricted the selection to galaxies with inclinations between 35 and 55 degrees, such that we can accurately measure the gas and SFR surface densities as well as derive kinematic parameters from rotation curve fitting. Objects near the Galactic plane or with evidence for tidal disruptions and mergers were removed from the sample, as were several of the closest systems where the size of the galaxy is larger than the $202'' \times 202''$ field of view of the wide field channel of ACS. To provide bright stellar emission as the background to study dust lanes in absorption, we selected the 10 highest surface brightness galaxies with $v_{circ} > 120\,km\,s^{-1}$ and the 10 highest surface brightness galaxies with $v_{circ} < 120\,km\,s^{-1}$, with circular velocities primarily estimated from single-dish observations of the H I emission line. Our final sample consists of 20 nearby, moderately inclined Sd to Sdm galaxies that bracket the circular velocity transition for dust scale heights found in Dalcanton et al. (2004). Table 1 provides the basic properties of the galaxies in our sample.

3. OBSERVATIONS AND DATA REDUCTION

Our H I data were obtained with the Very Large Array (VLA), operated by the National Radio Astronomy Observatory[6]. Most of these galaxies were observed between 2006 October and 2009 August for projects AM0873 and AM0942. In addition, we downloaded data from the VLA archive for two objects: NGC 5964 was observed in 2001 August for project AZ0133 and UGC 6446 was observed in 2002 June and November for project AL0575. We most often used the C configuration, where the largest angular structure that can be imaged is about $15'$ and the resolution is about $13''$. We used the CnB configuration, with its extended north arm, to observe four of the southern targets. The B configuration was used for a portion of the archival data for UGC 6446. The L-band observations were generally carried out using spectral line mode 4 with online Hanning smoothing, resulting in four intermediate frequency bands (IFs), each with a bandwidth of 1.5625 MHz, 64 channels, and channel widths of 24.414 kHz ($5.2\,km\,s^{-1}$). We tuned the AC and BD IFs to overlap in frequency, with the line emission approximately centered on the overlap region. The only exception is UGC 6446, which was observed in mode 2AD with online Hanning smoothing. The two IFs were tuned to the same frequency, each with a bandwidth of 1.5625 MHz, 128 channels, and channel widths of 12.207 kHz or $2.6\,km\,s^{-1}$. We include a detailed summary of the observations for each object in Table 2.

The objects in our sample were observed at various stages in the transition from the VLA to the Expanded Very Large Array (EVLA). A number of complications are present in data obtained during the upgrade, two of which are particularly important for our data. First, the EVLA L-band receivers have a wider bandpass than those on VLA antennas, which led to closure phase errors on VLA-EVLA baselines. Second, digital EVLA signals had to be converted into analog signals before being fed

[6] The National Radio Astronomy Observatory is a facility of the National Science Foundation operated under cooperative agreement by Associated Universities, Inc.

into the VLA correlator. A result of this conversion is that flux from frequencies 0.5 MHz below a given IF is aliased into the lower 0.5 MHz of that IF. The transition to the EVLA system was completed in 2010 January with the commissioning of the EVLA correlator. Thus new data from the EVLA are no longer affected by these issues.

We broadly followed the typical reduction procedure for H I spectral line data, except for a few important changes to address the effects of closure errors on VLA-EVLA baselines and aliasing. Our methods for managing the transition problems depended on the number of EVLA antennas in the array, as described in the following three sections.

3.1. *Data Processing with Five or Fewer EVLA Antennas*

For the ten objects observed in or before 2006 November, there were five or fewer EVLA antennas in the array. We simply excluded the EVLA antennas from the entire dataset and the results for these objects are therefore unaffected by closure errors on VLA-EVLA baselines and aliasing. These data were processed with the 31DEC05 version of the Astronomical Image Processing System (AIPS).

We first flagged the calibrator data, looking especially for problems in the first and last scans and for missing or corrupted data in blocks of time or in a single antenna. Next, we carried out the gain amplitude and phase calibration using the "channel 0" dataset, which is a vector average of the inner 75% of the frequency channels in the full spectral dataset. We used 3C48 and/or 3C286 (two of the recommended standard VLA calibrators) as our flux density calibrators and list the phase calibrator used for each object in Table 2. Our phase calibrators were observed approximately every 45 to 60 minutes. For the flux density calibrator, we solved for the antenna gain amplitude and phase corrections by comparing the observed and known amplitude and phase, using only baselines for which the calibrator is known to be a point source. We processed the phase calibrator in the same manner, except in this case we compared the observed amplitude to a constant but unknown intrinsic amplitude. We then applied the gain solution to the phase calibrator. Finally, we interpolated the phase calibrator gain amplitude and phase solutions in time to obtain the appropriate atmospheric correction for the source data.

We derived the bandpass solution by running BPASS on the full spectral dataset of the flux density calibrator. This gives the gain amplitude and phase correction as a function of frequency. We then divided the data into individual object sets, applied the gain and bandpass solutions, and stitched the AC and BD IFs together using SPLIT and UVGL or UJOIN. We performed the continuum subtraction in the uv plane using UVLIN. We determined the continuum level using a zeroth-order fit of at least ten line-free channels on both sides of the line. This low-level fit is appropriate as the average offset between the IFs is less than 2%. Finally, we used IMAGR to create naturally-weighted (using the parameter *robust* = 5) and robustly-weighted (*robust* = 0.5) data cubes, cleaning down to twice the noise. We also created an image from an average of the line-free channels and found that three galaxies have detectable continuum emission. We computed the noise in each data cube by averaging the rms surface brightness in a couple regions in signal-free channels. These values are given in Column 6 of Table 3 and are on average within 15% of the theoretical thermal noise limit. Finally, we converted the frequency axis to velocity and shifted the velocities to the heliocentric reference frame.

We summarize the properties of the final images in Table 3. For all naturally-weighted data cubes, we kept the original resolution, except in the case of NGC 3906, where we averaged two channels together. To achieve sufficient signal-to-noise, we averaged two channels together for over half of the robustly-weighted data cubes to give a final resolution of $10.4\,\mathrm{km\,s^{-1}}$. We produced images that are larger than typical for NGC 3906 and IC 1291 because both fields contain a bright continuum source outside the nominal field of view that was not adequately subtracted. For these objects, we cleaned two boxes: one centered on the galaxy and approximately $30'$ across and the second centered on the bright continuum source.

To obtain moment maps representing the integrated line intensity, the intensity-weighted velocity, and the velocity dispersion, we followed the procedure of Walter et al. (2008). We first convolved the original cube such that the beam major and minor axes are a factor of two to four larger. We then used the AIPS task BLANK to exclude emission fainter than twice the noise in the lower-resolution cube. We also manually blanked the lower-resolution cube to remove any noise peaks remaining after the flux cut. Finally, we used the lower-resolution cube as a mask to blank the original cube. The advantage of this procedure over simply applying a 2σ cut is that our blanked data cube contains real signal below that cut. We performed a primary beam correction on the blanked, naturally-weighted data cube using PBCOR and then created moment maps using XMOM. Note that we did not exclude single-channel emission peaks when creating the moment maps and we did no flux rescaling to correct for the fact that the cleaned data cube contains residual flux that is convolved with the dirty beam (Jorsater & van Moorsel 1995).

3.2. *Data Processing with Fifteen EVLA Antennas*

For the eight objects observed in 2008 May, there were fifteen EVLA antennas in the array. The reductions of these data were carried out with the 31DEC08 version of AIPS. To arrive at calibrated visibility data, we used the valuable reduction recipe developed by the LITTLE THINGS (Local Irregulars That Trace Luminosity Extremes - The HI Nearby Galaxy Survey; PI: Deidre Hunter; D. Hunter et al. 2011, in preparation) collaboration, with only minor adjustments. This recipe includes methods to reduce the effects of closure errors on VLA-EVLA baselines and aliasing[7]. In this section, we highlight the main differences between the reduction procedure described in Section 3.1 and the LITTLE THINGS procedure.

To address the aliasing problem, we excluded EVLA-EVLA baselines in the calibrator and source data. How-

[7] Methods for managing VLA-EVLA transition data are also described on the VLA Website: http://www.vla.nrao.edu/astro/guides/evlareturn/.

ever, this did not completely remove the aliased signal, as we discuss further in Section 3.4. To address the closure error problem, our first major reduction step was to determine the bandpass solution from the flux density calibrator. Applying this solution removes the slope in phase as a function of frequency, which is introduced by the different VLA and EVLA receiver bandpasses. We used AVSPC to apply the bandpass solution and average over frequency to create a new channel 0 dataset. We then carried out the gain amplitude and phase calibration using the new channel 0. The remaining reduction steps were similar to those described in Section 3.1.

3.3. *Data Processing with Twenty-two EVLA Antennas*

The observations of NGC 4519 and UGC 6930 in 2009 July and August were carried out with twenty-two EVLA antennas, leaving only four VLA antennas remaining in the array. We included all functioning EVLA antennas and EVLA-EVLA baselines for calibration as well as in the object data because excluding them would have resulted in an unacceptable loss of signal. We study the effect of this choice in Section 3.4. Otherwise, we used the same reduction method as in Section 3.2, that is we employ the LITTLE THINGS recipe.

3.4. *More on Aliasing*

Aliasing is a result of the digital to analog conversion that was required for EVLA signals to be processed by the VLA correlator. Flux from 0.5 MHz below a given IF is aliased into the lower 0.5 MHz of the IF. Aliasing affects both IFs in the calibrator data because there is continuum emission at lower frequencies relative to each IF. It also affects the object data because we employed band-stitching, where the AC and BD IFs overlap in frequency, and the line emission is centered on the overlap region. The line emission in the lower-frequency IF should be unaffected by aliasing because there is little source continuum emission that could be aliased into the IF and the line emission is almost exclusively in the upper 0.5 MHz of the IF, whereas any aliased signal would affect the lower 0.5 MHz. The higher-frequency IF is affected because line emission from the lower-frequency IF is aliased into the higher-frequency IF.

For the objects observed in May 2008, we expected that excluding EVLA-EVLA baselines would remove the aliased signal because it should not correlate on EVLA-VLA baselines. Surprisingly, the data are still affected, in that we see evidence of aliasing in the antenna-averaged and normalized bandpass correction amplitude determined from the flux density calibrator (described further in the next paragraph). Nevertheless, the effect on the integrated flux is the same or smaller than in the case of the objects observed in 2009, which we describe further below.

We investigated the effect of the aliased signal on the integrated flux using UGC 6930 and NGC 4519, the objects observed with only four VLA antennas remaining in the array. The aliased signal is strongest at the low-frequency end of the IF and decreases with increasing frequency. As a result, the antenna-averaged and normalized bandpass correction amplitude determined from the flux density calibrator spectrum reaches a minimum of about 0.7 to 0.8 in the lowest-frequency channel and reaches 1.0 at about 0.5 MHz higher frequency. We applied this bandpass correction to the object data but it is not necessarily appropriate for correcting the aliased signal from a line source. To illustrate the effect, imagine all the line emission, with a box profile, is in the upper (lower) frequency IF and the bandpass correction is 0.8 for all channels. After bandpass correction, the integrated flux would be underestimated (overestimated) by 20%.

The above illustrates the worst case scenario. The aliased signal drops off with increasing frequency and we always have line emission in the upper and lower IFs. Both these facts decrease the effect of the aliased signal on the integrated flux. We found it difficult to precisely estimate the difference between the final spectrum, including aliased flux, and the intrinsic spectrum. Our best estimate for the contamination of aliased signal to the integrated line flux is 3% - 11%. This estimate is based on the spectrum of NGC 4519, which has a typical line flux and profile. For the upper (lower) bound, we assumed that the peak (minimum) intensity from the upper 0.5 MHz of the lower-frequency IF was aliased into each channel of the lower 0.5 MHz of the upper-frequency IF according to the amplitude of the bandpass correction. Specifically, the estimated aliased intensity for a channel is $I_{\rm peak}(1/BP_i - 1)$, where $I_{\rm peak}$ is the peak intensity from the lower-frequency IF, i is the channel number in the upper-frequency IF, and BP_i is the bandpass correction amplitude at channel i. We then compared the integrated aliased flux to the integrated line flux without bandpass correction. We expect that the contamination of the aliased signal to the intrinsic integrated flux is of similar order.

We do not make any correction for aliasing. Depending on how the line profile is distributed over the IFs, the integrated flux could be overestimated or underestimated by 3% - 11%. We take this into account in our error estimates of the integrated flux. We expect the impact of the aliased signal on the rotation curve analysis to be minimal because any aliased signal should be spatially offset from real emission and we do not see any evidence of this.

4. DATA PRODUCTS

4.1. *Channel Maps*

Figures 1 - 20 show channel maps for the galaxies, with units of mJy beam^{-1}. We created the maps from the naturally-weighted data cubes so low surface brightness features are more visible. The cubes have neither been blanked nor primary beam corrected, so the original noise properties of the image are apparent. We use a linear scaling, with the minimum and maximum surface brightness noted in the caption. Note that the ESO 555-G027 and ESO 501-G023 data cubes have residual imaging artifacts to the north and south of the galaxy that remained after cleaning.

4.2. *Integrated Line Profiles, Integrated Fluxes, and Integrated Intensity Maps*

Figure 21 shows the integrated H I line profiles of the galaxies, which were created by summing the emission in each channel of the naturally-weighted, blanked, and primary beam corrected data cubes. The majority of our

sample shows the double-horned profile that indicates a disk with a flat rotation curve, which generally agrees with our rotation curve analysis in Section 4.3. From these line profiles, we calculated W_{20}, the width of the line at 20% of the peak flux density, and corrected each value for spectral resolution. We make no correction for turbulent broadening, but note that the typical velocity dispersion of H I gas is about $10\,\mathrm{km\,s^{-1}}$. We assign an uncertainty in W_{20} equal to the channel width, which is $5\,\mathrm{km\,s^{-1}}$ for all objects except UGC 6446 and NGC 3906, where the uncertainty is $3\,\mathrm{km\,s^{-1}}$ and $10\,\mathrm{km\,s^{-1}}$, respectively.

Figure 22 compares our W_{20} values to single-dish values from the literature. The left panel compares to values from the H I Parkes All Sky Survey (HIPASS), which used the 64-m Parkes telescope (Meyer et al. 2004). The right panel compares to values from the Third Reference Catalogue of Bright Galaxies (RC3; de Vaucouleurs et al. 1991). The HIPASS values are generally larger than ours, whereas the RC3 values agree better, with a scatter of about 8%. It is unlikely that we have resolved out flux at large scales, which might be associated with larger velocities, because we see no systematic offset between our total H I fluxes and single-dish values (see Figure 23). Furthermore, the extent of each galaxy is less than the largest angular structure for which the C configuration is sensitive ($\sim 15'$; although note that this angular sensitivity is only strictly appropriate for full-synthesis data). Finally, the offset between the HIPASS W_{20} values and our values is not larger for objects with rotation curves that continue rising to the edge of the H I disk (see Section 4.3). We accept our W_{20} values as being in reasonable agreement with values quoted in the literature, with no systematic offset relative to values quoted in the RC3.

We measured the total H I flux by summing the line profiles over velocity. The main contributors to the integrated flux uncertainty are flux calibration (5% effect) and aliasing (up to an 11% effect). For a few objects, we tested whether excluding single-channel flux peaks affects the total flux. To do so, we convolved the mask used in blanking to a larger velocity resolution. The dominant effect was that the noise was lower, and thus the flux cut for blanking was decreased and the integrated flux was larger, 10% larger in the case of a bright galaxy and 50% larger in the case of a faint galaxy. The effect of different flux cuts is not typically included in error estimates, so we only assign the quadrature sum of the flux calibration and aliasing errors (12%) as the generic uncertainty associated with the integrated fluxes.

Figure 23 provides a comparison of our integrated fluxes to values from HIPASS (Meyer et al. 2004) or Springob et al. (2005), who compiled measurements from a variety of large single-dish telescopes. Our values are in agreement with the literature values, but with a scatter of about 30%. This is typical for comparisons between data from different instruments (e.g., Walter et al. 2008). We also compute the total H I masses, assuming the gas is optically thin, using:

$$M_{HI}[M_\odot] = 2.36 \times 10^5 D^2 \times \sum_i S_i\,\Delta v, \qquad (1)$$

where D is the distance in Mpc, S_i is total flux density in a channel in Jy, Δv is the velocity width of a channel in $\mathrm{km\,s^{-1}}$, and the sum is over all channels that show line emission. We made no correction for H I self absorption. Note that the H I mass in NGC 6509 is a lower limit because a region is in absorption rather than emission, due to the strong radio lobe of a background galaxy; see Section 5 for more details.

Table 4 contains our integrated H I flux, H I mass, and W_{20} values, as well as comparison integrated flux and W_{20} values from single-dish measurements in the literature. Figure 24 shows our derived H I masses versus circular velocity, which we calculate in Section 4.3. As expected, the H I mass generally increases with increasing circular velocity. The outlier is NGC 2805, which has a high but reasonable integrated flux value. For NGC 2805 to agree with the main distribution in Figure 24, the distance would have to be about 10 Mpc rather than the Table 1 value of 28.0 Mpc, which is derived from the Tully-Fisher relation. However, the recession velocity is consistent with a distance of 28.0 Mpc and the smaller distance would have other implications. For example, the nuclear star cluster in this galaxy would be somewhat small and faint compared to the distribution of nuclear star cluster sizes and magnitudes in Böker et al. (2004).

Figure 25 shows the integrated H I intensity map for each galaxy, derived from the naturally-weighted, blanked, and primary beam corrected data cube, with units of $\mathrm{Jy\,beam^{-1}\,km\,s^{-1}}$.

4.3. *Rotation Curves*

In our rotation curve analysis, we aim to derive global kinematic properties rather than characterize the detailed rotation curve shape. We therefore simply used the first moment of the data cube as our velocity field, which provides the intensity-weighted mean velocity at each spatial pixel. de Blok et al. (2008) found that the use of the first moment can bias the rotation curve fit if the velocity profile is asymmetric. They instead favor the use of a third-order Gauss-Hermite polynomial to fit the line profile and derive the velocity field. Nonetheless, using the first moment should be sufficient for our goals. We primarily used the first-moment map created with the MOMENTS task within the Groningen Image Processing SYstem (GIPSY; van der Hulst et al. 1992). We blanked pixels with values less than three times the image noise and excluded single-channel wide peaks. This blanking procedure is different from our primary method, described in Section 3.1. The method described in Section 3.1 retains low-level emission, but may also allow residual beam pattern from side lobes to contribute to the moments. Excluding low-level emission should have little effect on the rotation curve analysis since it has little weight in the first moment. However, UGC 1862 is so faint that we used the first-moment map created from the data cube that was blanked with our primary method.

We used first-moment maps created from the robustly-weighted data cubes, which provide higher spatial resolution, for 12 objects. The remaining eight objects (ESO 544-G030, UGC 1862, ESO 418-G008, ESO 555-G027, ESO 501-G023, UGC 6446, NGC 3906, and IC 1291) are fainter, so we created moment maps from the naturally-weighted data cubes, which have better sensitivity. The first-moment maps were not corrected for primary beam attenuation.

We carried out velocity field modeling for our galaxies on the first-moment maps with the ROTCUR task within GIPSY. ROTCUR performs a least-squares fit, comparing the data to a model composed of a series of tilted rings described by

$$V_{\rm los}(x,y) = V_{\rm sys} + V_{\rm rot}\sin(i)\cos(\theta), \quad (2)$$

where $V_{\rm los}(x,y)$ is the line of sight velocity at position (x,y) in the plane of the sky, $V_{\rm sys}$ is the systemic velocity, $V_{\rm rot}$ is the rotation velocity, i is the inclination, and θ is the angle between the major axis and the position of interest in the plane of the galaxy.

As initial estimates for the center, position angle of the major axis (PA), and inclination, we used values derived from ellipse fits of *Spitzer Space Telescope* IRAC Channel 1 (3.6 μm) data, described in L. Watson et al. (2011, in preparation). In four cases (NGC 2805, ESO 501-G023, UGC 6446, and IC 1291), the IRAC fits did not converge so we used RC3 parameters as initial estimates. Our initial estimate for the systemic velocity was obtained from NED[8].

We followed a typical velocity field modeling procedure, outlined below (see also Begeman 1989; Haan et al. 2008). We solved for the systemic velocity, center, PA, inclination, and rotation velocity by successively fitting for a single parameter as a function of radius while most of the other parameters were held fixed. Except for the rotation velocity, we calculated the weighted mean of the values at all radii, excluding the first and last annuli. The errors used in the weighted mean are the formal least squares errors provided by ROTCUR. In subsequent runs, we held the parameter fixed as a function of radius at the value of the weighted mean. In doing so, we ignored real variations caused by warps and bars, but we accepted this since we are only interested in global kinematics. In all fits, we forced the radial velocity to zero. We excluded points within 20° of the minor axis and used a $|\cos(\theta)|$ weighting so points near the major axis were weighted more than points near the minor axis, where beam smearing becomes severe. We fit both the approaching and receding sides of the galaxy simultaneously and sampled the rotation curve every $(B_{\rm maj}\,B_{\rm min})^{1/2}$, beginning at $(B_{\rm maj}\,B_{\rm min})^{1/2}/2$, where $B_{\rm maj}$ and $B_{\rm min}$ are the beam major axis and minor axis FWHM in arcseconds.

We verified the agreement between each data cube and the derived velocity field model using the INSPECTOR task within GIPSY. We also created two-dimensional model velocity fields described completely by the derived parameters, using VELFI in GIPSY, and subtracted the model from the data to form a residual velocity map. We examined the residual map for signs of parameter mis-estimation (for examples, see van der Kruit & Allen 1978) and also noted the rms of the residual distribution.

In the above procedure, we have allowed the parameters to veer away from the initial estimates derived from the IRAC ellipse fits. Therefore, we did one final check: we calculated the rotation velocities again, but used the IRAC center rather than the fitted value. We again created a model two-dimensional velocity field and residual velocity map. We declared that the IRAC center fit the data as well as the fitted value if the rms of the residual map was the same (within one tenth the channel width) or smaller than the original rms, and if the residual velocity map had not developed any symptoms of data-model mismatch. We carried out this same procedure for the PA and inclination. If an IRAC parameter fit the data as well as the value determined in ROTCUR, we chose the IRAC parameter, as it was derived from independent data and also fit the kinematics. We only chose an RC3 parameter over a ROTCUR parameter if it fit the data significantly better. We chose the IRAC center for eleven objects, the IRAC PA for eight objects (primarily when the fitted value was very similar to the IRAC value), the IRAC inclination in all sixteen galaxies where it was available, and the RC3 inclination for one object. See Table 5 for a comparison of the parameters derived in the rotation curve analysis, the IRAC values, and the RC3 values. The final parameter values are given in Table 6, where Column 10 lists which parameters are derived from the IRAC analysis; all others are from the rotation curve analysis.

Inclinations are difficult to derive from tilted ring models for galaxies with $i < 40°$ (Begeman 1989). Furthermore, the rotation velocities derived at these inclinations are less accurate and precise because the velocity dispersion of the gas becomes a larger fraction of the line-of-sight velocity and small inclination errors lead to large rotation velocity errors. Ten of our objects have final inclinations below 40°. Fortunately, we have additional inclination information from the IRAC ellipse fits and our procedure led us to use the IRAC value whenever it was available. This additional constraint allows us to derive accurate kinematics for the low-inclination sources. In addition, the uncertainty in the inclination is reflected in the circular velocity uncertainty, described further below.

Figures 26-45 show the velocity fields and position-velocity diagrams for the sample. In each figure, the top row, left panel shows the first-moment map, created using the method described above in this section and covering the same area as the channel maps for the object. The middle panel shows the tilted ring model velocity field and the right panel shows the residual velocity map – the first-moment map minus the model velocity field. The dynamical center (from Columns 5 and 6 in Table 6) is shown as a cross in all three panels and the systemic velocity (from Column 2 of Table 6) is shown as a thick black contour in the left and middle panels. The bottom row of each figure shows the position-velocity diagram along the major axis in the left panel and along the minor axis in the right panel. These figures display data extracted from a slice that is a single spatial pixel in width (see Column 8 of Table 3 for pixel size in arcseconds). The contours start at twice the image noise, increase in intervals of twice the image noise, and end at the maximum surface brightness along the major axis slice plus that interval. We give the specific range in each figure. For comparison, the projected tilted ring model values along the major axis are overplotted as solid triangles in the left panel.

We are particularly interested in deriving accurate circular velocities from our rotation curve analysis because in future work we will study star formation and secular

[8] The NASA/IPAC Extragalactic Database (NED) is operated by the Jet Propulsion Laboratory, California Institute of Technology, under contract with the National Aeronautics and Space Administration.

evolution above and below the dust scale height transition velocity of $v_{circ} = 120\,km\,s^{-1}$, which was observed in Dalcanton et al. (2004). We take the maximum velocity from the deprojected rotation curve as a measure of the circular velocity. These values are listed in Column 8 of Table 6. Dalcanton & Bernstein (2002) primarily measured the circular velocity as half W_{50} (the line width at 50% of the peak flux density) from single-dish H I data. For about one quarter of their sample, they used the maximum velocity in long-slit Hα rotation curves. No inclination correction was necessary because they studied edge-on disks. The maximum velocity from the rotation curve is not an optimal measure of the circular velocity because it is sensitive to details of the rotation curve shape (Persic et al. 1996; Kannappan et al. 2002). Alternative methods are used in Tully-Fisher relation studies, which often evaluate a parametrization of the rotation curve at a relatively large radius (see, e.g., Courteau 1997; Kannappan et al. 2002; Pizagno et al. 2007). The form of the parametrization and the radius at which the fit is evaluated vary. For simplicity and for consistency with Dalcanton & Bernstein (2002), we used the maximum velocity from the rotation curve as a measure of the circular velocity. As a check, we compared our circular velocities to values estimated as $W_{50}/2/\sin(i)$, where we measured W_{50} from our integrated H I line profiles and i is from Column 4 of Table 6, and found good agreement.

We calculated the errors listed in Table 6 in the following ways. The error on an IRAC parameter is the standard deviation of the parameter values for the outer few isophotes of the ellipse fits. The error on the systemic velocity, center, PA, or inclination determined from the velocity field modeling is the standard deviation of the individual ring values about the weighted mean, divided by the square-root of the number of rings. We excluded the first and last ring in this calculation. We chose this error estimate because it is most well-matched with the IRAC errors. Note that the ESO 501-G023 inclination is from RC3, but RC3 does not give an error, so the inclination error is the value from the velocity field modeling. The final inclination for NGC 4561 and PA for PGC 6667 are from the IRAC analysis, but we quote errors from the velocity field modeling because the outer few isophotes in the IRAC data have the same values, which gives a standard deviation of zero. The systemic velocity for UGC 1862 is from a single ring and the error is just the ROTCUR formal least squares error for that ring.

The circular velocity errors in Column 8 of Table 6 are propagated inclination errors. Specifically, we ran ROTCUR using our final inclination plus and minus the inclination error (from Column 4 of Table 6), and the circular velocity errors are the deviation of the maximum rotation velocity in these runs from the nominal value. These errors are a measure of the uncertainty associated with converting the measured velocity into a deprojected value. We do not include the formal least squares error returned by ROTCUR, which is a measure of the error in the observed rotation velocity. The formal least squares error returned by ROTCUR accounts for correlations between parameters that are allowed to vary as a function of radius. Because we hold the systemic velocity, PA, center, and particularly the inclination fixed for all annuli when calculating the final rotation curve, the output formal least squares error on the rotation velocities are underestimates. These values, albeit underestimated, are typically significantly smaller than the propagated inclination errors. There is also an uncertainty associated with whether the maximum velocity is a good measure of the circular velocity, which is typically the case when a galaxy rotation curve shows a clear turnover. Six of our galaxies do not fall in this category. To address this concern, we assigned each galaxy a rotation curve quality assessment, listed in Column 9 of Table 6. Rankings A, B, and C refer to galaxies with clear, moderate, and no rotation curve turnovers, respectively.

5. MORPHOLOGY AND EVIDENCE FOR INTERACTIONS

Three of our objects have two kinematic components: NGC 4561, NGC 4713, and NGC 6509. The main component covers most of or more than the optical disk and the outer component is characterized by low surface brightness emission in the outer disk. We carried out the velocity field modeling separately for the two components. Table 6 quotes only the kinematic parameters determined for the main component, as it corresponds to the optical disk. For the outer component fit, we used the naturally-weighted data cubes, blanked using the method described in Section 3.1, which better probes the low surface brightness emission. The left panel of the top, middle, and bottom rows in Figure 46 shows the main and outer components in the first-moment map of NGC 4561, NGC 4713, and NGC 6509, respectively. The position angle of the major axis of the outer component differs by between about 30° and 90° from that of the main component.

The middle panel of each row shows the position-velocity diagram along the major axis of the outer component while the right panel of each row shows the position-velocity diagram along the major axis of the main component. The filled triangles and circles show the projected tilted ring model values for the outer and main components, respectively. Although much of the emission in the first-moment maps is of low significance, the position-velocity diagrams show that there is significant emission in the outer-disk components. These outer components are likely due to a warp, which may indicate that these galaxies have undergone a recent interaction.

We detected a companion(s) to NGC 0337, NGC 2805, ESO 501-G023, NGC 3906, and IC 1291 within the $\sim 30'$ field of view and $\sim 500\,km\,s^{-1}$ bandwidth of our final H I data cubes. These objects may deserve further investigation into whether the galaxies are interacting with the companions. However, we see no obvious evidence of bridges or tidal tails in any of the data to suggest an ongoing interaction.

NGC 6509 shows H I in absorption on the east side of the galaxy because it is in the foreground of the radio source 4C +06.63, which is the northwest component of a pair of radio lobes, the southeast component being VLSS J1759.5+0615. 4C +06.63 is centered at approximately RA 17:59:29.6 and DEC 06:17:13 (J2000), about $65''$ east of the galaxy center. It is slightly resolved, with a FWHM of $20''$ in a continuum image with a beam size of $15.97'' \times 14.76''$. The full extent of the source is approximately $1'$. Because of this absorption, the H I mass in NGC 6509 is a lower limit. We made no adjustments to the rotation curve analysis for this object. Especially

note that we still used both the approaching and receding side of the galaxy, including about 25° where absorption is evident in position velocity diagrams. Even so, the rotation curve model is acceptable.

6. SUMMARY

We have presented H I channel maps, line profiles, and integrated intensity maps for a sample of 20 nearby, moderately inclined, bulgeless disk galaxies, which were selected to bracket the circular velocity transition for dust scale heights found in Dalcanton et al. (2004). We have also calculated H I fluxes and H I masses and have carried out rotation curve fitting to derive kinematic properties, in particular the circular velocity, for each galaxy. We found that three objects in our sample have two kinematic components, which may indicate a recent interaction. The remaining objects appear undisturbed, which makes them well suited for studying the internal evolution of galaxies with quiescent merger histories. We will use the data presented here, as well as data from the IRAM 30 m, MDM, the *Spitzer Space Telescope*, and *HST* in studies of star formation, dust properties, and secular evolution in bulgeless disk galaxies as a function of circular velocity.

We thank the LITTLE THINGS group, especially Dana Ficut-Vicas and Elias Brinks for generously providing us with their data reduction recipe for VLA-EVLA transition data. We are also grateful to Sebastian Haan and Fabian Walter for advice on the data reductions, to Eric Greisen for help with AIPS, and to the VLA for rescheduling observations of UGC 6930 and NGC 4519. We thank the referee for helpful comments and the MPIA for hospitality and support during several productive visits. L.C.W. gratefully acknowledges support from an NSF Graduate Research Fellowship. P.M. is grateful for support from the NSF via award AST-0705170. U.L. acknowledges financial support from the research project AYA2007-67625-C02-02 from the Spanish Ministerio de Ciencia y Educación and from the Junta de Andalucía.

REFERENCES

Abadi, M. G., Navarro, J. F., Steinmetz, M., & Eke, V. R. 2003, ApJ, 591, 499
Begeman, K. G. 1989, A&A, 223, 47
Böker, T., Lisenfeld, U., & Schinnerer, E. 2003, A&A, 406, 87
Böker, T., Sarzi, M., McLaughlin, D. E., van der Marel, R. P., Rix, H.-W., Ho, L. C., & Shields, J. C. 2004, AJ, 127, 105
Brook, C. B., et al. 2011, MNRAS, 595
Cameron, E., Driver, S. P., Graham, A. W., & Liske, J. 2009, ApJ, 699, 105
Courteau, S. 1997, AJ, 114, 2402
Dalcanton, J. J., & Bernstein, R. A. 2000, AJ, 120, 203
Dalcanton, J. J., & Bernstein, R. A. 2002, AJ, 124, 1328
Dalcanton, J. J., Yoachim, P., & Bernstein, R. A. 2004, ApJ, 608, 189
de Blok, W. J. G., Walter, F., Brinks, E., Trashcans, C., Oh, S.-H., & Kennicutt, R. C. 2008, AJ, 136, 2648
de Vaucouleurs, G., de Vaucouleurs, A., Corwin, H. G., Jr., Buta, R. J., Paturel, G., & Fouque, P. 1991, Third Reference Catalogue of Bright Galaxies (New York: Springer)
Doyle, M. T., et al. 2005, MNRAS, 361, 34
Haan, S., Schinnerer, E., Mundell, C. G., García-Burillo, S., & Combes, F. 2008, AJ, 135, 232
Hopkins, P. F., Hernquist, L., Cox, T. J., Younger, J. D., & Besla, G. 2008, ApJ, 688, 757
Hopkins, P. F., et al. 2009, MNRAS, 397, 802
Jorsater, S., & van Moorsel, G. A. 1995, AJ, 110, 2037
Kannappan, S. J., Fabricant, D. G., & Franx, M. 2002, AJ, 123, 2358
Karachentsev, I. D., Karachentseva, V. E., & Parnovskij, S. L. 1993, Astronomische Nachrichten, 314, 97
Katz, N., & Gunn, J. E. 1991, ApJ, 377, 365
Kautsch, S. J., Grebel, E. K., Barazza, F. D., & Gallagher, J. S., III 2006, A&A, 445, 765
Kormendy, J., Drory, N., Bender, R., & Cornell, M. E. 2010, ApJ, 723, 54
Kormendy, J., & Kennicutt, R. C., Jr. 2004, ARA&A, 42, 603
Martini, P., Regan, M. W., Mulchaey, J. S., & Pogge, R. W. 2003, ApJS, 146, 353
Matthews, L. D., & Gallagher, J. S., III 1997, AJ, 114, 1899
Matthews, L. D., Gao, Y., Uson, J. M., & Combes, F. 2005, AJ, 129, 1849
Meyer, M. J., et al. 2004, MNRAS, 350, 1195
Mould, J. R., et al. 2000, ApJ, 529, 786
Navarro, J. F., & Steinmetz, M. 2000, ApJ, 538, 477
Navarro, J. F., & White, S. D. M. 1994, MNRAS, 267, 401
Persic, M., Salucci, P., & Stel, F. 1996, MNRAS, 281, 27
Pizagno, J., et al. 2007, AJ, 134, 945
Rafikov, R. R. 2001, MNRAS, 323, 445
Robertson, B., Bullock, J. S., Cox, T. J., Di Matteo, T., Hernquist, L., Springel, V., & Yoshida, N. 2006, ApJ, 645, 986
Springob, C. M., Haynes, M. P., Giovanelli, R., & Kent, B. R. 2005, ApJS, 160, 149
Stark, A. A., & Lee, Y. 2005, ApJ, 619, L159
Stewart, K. R., Bullock, J. S., Wechsler, R. H., Maller, A. H., & Zentner, A. R. 2008, ApJ, 683, 597
Toth, G., & Ostriker, J. P. 1992, ApJ, 389, 5
Tully, R. B. 1988, Nearby Galaxies Catalog (Cambridge: Cambridge Univ. Press)
Tully, R. B., Shaya, E. J., Karachentsev, I. D., Courtois, H. M., Kocevski, D. D., Rizzi, L., & Peel, A. 2008, ApJ, 676, 184
van der Hulst, J. M., Terlouw, J. P., Begeman, K. G., Zwitser, W., & Roelfsema, P. R. 1992, in ASP Conf. Ser. 25, Astronomical Data Analysis Software and Systems I, ed. D. M. Worrall, C. Biemesderfer, & J. Barnes (San Francisco, CA: ASP), 131
van der Kruit, P. C., & Allen, R. J. 1978, ARA&A, 16, 103
Walter, F., Brinks, E., de Blok, W. J. G., Bigiel, F., Kennicutt, R. C., Thornley, M. D., & Leroy, A. 2008, AJ, 136, 2563
White, S. D. M., & Rees, M. J. 1978, MNRAS, 183, 341

TABLE 1
General Galaxy Properties

Source	RA (J2000.0) (hh:mm:ss.s)	DEC (J2000.0) (dd:mm:ss)	D (Mpc)	D_{25} (arcsec)	m_B (mag)	M_B (mag)	Type
(1)	(2)	(3)	(4)	(5)	(6)	(7)	(8)
NGC 0337	00:59:50.0	-07:34:41	20.7 [T88]	173	11.44	-20.14	7.0
PGC 3853	01:05:04.8	-06:12:46	11.4 [T08]	250	11.98	-18.30	7.0
PGC 6667	01:49:10.3	-10:03:45	24.6 [T88]	173	12.92	-19.03	6.7
ESO 544-G030	02:14:57.2	-20:12:40	13.9 [T08]	123	13.25	-17.47	7.7
UGC 1862	02:24:24.8	-02:09:41	22.3 [T08]	99.6	13.47	-18.27	7.0
ESO 418-G008	03:31:30.8	-30:12:46	23.6 [T08]	70.5	13.65	-18.21	8.0
ESO 555-G027	06:03:36.6	-20:39:17	24.3 [T88]	138	13.18	-18.75	7.0
NGC 2805	09:20:20.4	+64:06:12	28.0 [T88]	379	11.17	-21.07	7.0
ESO 501-G023	10:35:23.6	-24:45:21	7.01 [T08]	208	12.86	-16.37	8.0
UGC 6446	11:26:40.6	+53:44:58	18.0 [T08]	213	13.30	-17.98	7.0
NGC 3794	11:40:54.8	+56:12:10	19.2 [T08]	134	13.23	-18.19	6.5
NGC 3906	11:49:40.2	+48:25:30	18.3 [...]	112	13.50	-17.81	7.0
UGC 6930	11:57:17.2	+49:17:08	17.0 [T88]	262	12.38	-18.77	7.0
NGC 4519	12:33:30.5	+08:39:16	19.6 [T08]	190	12.15	-19.31	7.0
NGC 4561	12:36:08.6	+19:19:26	12.3 [T88]	90.8	12.82	-17.63	8.0
NGC 4713	12:49:58.1	+05:18:39	14.9 [T08]	162	11.85	-19.02	7.0
NGC 4942	13:04:19.2	-07:39:00	28.5 [T88]	112	13.27	-19.00	7.0
NGC 5964	15:37:36.3	+05:58:28	24.7 [T88]	250	12.28	-19.68	7.0
NGC 6509	17:59:24.9	+06:17:12	28.2 [T88]	95.1	12.12	-20.13	7.0
IC 1291	18:33:51.5	+49:16:45	31.5 [T88]	109	13.28	-19.21	8.0

Note. — Column 1: Object name; Column 2 and 3: Right ascension (RA) and declination (DEC) from de Vaucouleurs et al. (1991); Column 4: Distance and distance reference. Distances are derived using the Tully-Fisher relation, except for NGC 3906. T08: Tully et al. (2008), T88: Tully (1988), and the NGC 3906 distance is from the de Vaucouleurs et al. (1991) heliocentric velocity, corrected for Virgo infall using Mould et al. (2000) and using $H_0 = 71\,\mathrm{km\,s^{-1}\,Mpc^{-1}}$. Note that the NGC 2805 distance may be overestimated. See Section 4.2 for details. Column 5: Major isophotal diameter at $25\,\mathrm{mag\,arcsec^{-2}}$ in the B band, from de Vaucouleurs et al. (1991). Column 6: Apparent blue magnitude, corrected for Galactic and internal extinction and redshift. Values are from de Vaucouleurs et al. (1991), except for NGC 4942 and PGC 6667, which are from Doyle et al. (2005) and are only corrected for Galactic extinction. Column 7: Absolute blue magnitude, calculated from the apparent magnitude in column 6 and the distance in column 4. Column 8: Morphological type from de Vaucouleurs et al. (1991).

TABLE 2
SUMMARY OF OBSERVATIONS

Source	Conf.	Date (yyyy-mm-dd)	Start (hh:mm)	End (hh:mm)	On-source (hh:mm)	Mode	Chan. (No.)	$\Delta\nu$ (kHz)	Δv ($\mathrm{km\,s^{-1}}$)	$\mathrm{v_{hel,1}}$ ($\mathrm{km\,s^{-1}}$)	$\mathrm{v_{hel,2}}$ ($\mathrm{km\,s^{-1}}$)	Flux Calibrator	Phase Calibrator	Flux Density (Jy)
(1)	(2)	(3)	(4)	(5)	(6)	(7)	(8)	(9)	(10)	(11)	(12)	(13)	(14)	(15)
NGC 0337	C	2006-11-04	00:23	05:26	01:54	4	64	24.41	5.21	1520.4	1770.7	3C48	0059+001	2.318 ± 0.007
PGC 3853	C	2006-11-04	00:39	05:29	02:00	4	64	24.41	5.20	968.4	1217.8	3C48	0059+001	2.316 ± 0.007
PGC 6667	C	2006-11-04	05:30	07:44	01:57	4	64	24.41	5.23	1857.4	2108.2	3C48	0157-107	2.000 ± 0.010
ESO 544-G030	CnB	2006-10-08	07:08	10:33	02:59	4	64	24.41	5.21	1487.4	1737.6	3C48	0240-231	6.13 ± 0.02
	CnB	2006-10-12	06:57	10:26	02:59	4	64	24.41	5.21	1487.4	1737.6	3C48	0240-231	6.025 ± 0.011
UGC 1862	C	2006-11-04	07:46	10:03	01:58	4	64	24.41	5.20	1257.4	1507.2	3C48	0231+133	1.511 ± 0.002
ESO 418-G008	CnB	2006-10-10	07:31	10:56	02:57	4	64	24.41	5.20	1067.4	1316.9	3C48	0416-209	2.576 ± 0.010
	CnB	2006-10-15	08:17	11:06	02:35	4	64	24.41	5.20	1067.4	1316.9	...	0416-209	2.58
ESO 555-G027	CnB	2006-10-12	10:26	14:00	03:04	4	64	24.41	5.23	1855.4	2106.2	3C48	0609-157	2.848 ± 0.010
NGC 2805	C	2008-05-14	01:51	04:12	01:59	4	64	24.41	5.21	1617.7	1867.7	3C286	0841+708	3.278 ± 0.012
ESO 501-G023	CnB	2006-10-12	14:02	17:17	03:00	4	64	24.41	5.19	914.4	1163.7	3C48	1057-245	1.050 ± 0.003
UGC 6446	B	2002-06-22	19:10	07:06	09:40	2AD	128	12.21	2.59	643.7	...	3C286	1035+564	1.816 ± 0.004
	C	2002-11-18	11:39	17:51	05:05	2AD	128	12.21	2.59	643.7	...	3C286	1035+564	1.788 ± 0.003
NGC 3794	C	2008-05-17	01:40	04:00	01:58	4	64	24.41	5.20	1254.7	1504.1	3C286	1035+564	1.838 ± 0.010
NGC 3906	C	2008-05-16	01:44	04:04	01:59	4	64	24.41	5.18	832.7	1081.4	3C286	1219+484	0.602 ± 0.003
UGC 6930	C	2009-07-30	23:37	02:05	01:57	4	64	24.41	5.18	647.5	896.2	3C286	1219+484	0.656 ± 0.004
NGC 4519	C	2009-08-05	00:15	02:46	02:00	4	64	24.41	5.19	1097.1	1346.2	3C286	1254+116	0.765 ± 0.004
NGC 4561	C	2008-05-14	04:13	06:37	01:59	4	64	24.41	5.20	1279.6	1529.1	3C286	1254+116	0.771 ± 0.007
NGC 4713	C	2008-05-16	04:04	06:28	01:59	4	64	24.41	5.17	524.6	772.8	3C286	1254+116	0.761 ± 0.006
NGC 4942	C	2008-05-17	04:00	06:24	01:58	4	64	24.41	5.21	1623.6	1873.7	3C286	1246-075	0.495 ± 0.003
NGC 5964	C	2001-08-20	20:45	04:31	06:21	4	64	24.41	5.21	1312.1	1582.9	3C286	1557-000	0.6275 ± 0.0013
NGC 6509	C	2008-05-13	08:54	11:14	01:58	4	64	24.41	5.21	1686.5	1936.6	3C286,3C48	1751+096	1.373 ± 0.007
IC 1291	C	2008-05-13	11:14	13:38	01:58	4	64	24.41	5.22	1858.2	2108.6	3C286,3C48	1845+401	0.941 ± 0.003

NOTE. — Column 1: Object name; Column 2: VLA Configuration; Column 3: Date observed in International Atomic Time (IAT); Column 4: Start time of observation (IAT); Column 5: End time of observation (IAT); Column 6: Time spent on source; Column 7: Correlator mode; Column 8: Number of channels per IF; Column 9: Channel width in kHz; Column 10: Channel width in $\mathrm{km\,s^{-1}}$; Column 11: Central heliocentric velocity of IF1; Column 12: Central heliocentric velocity of IF2; Column 13: Flux calibrator: 3C48 and 3C286 are also known as 0137+331 1331+305 in J2000, respectively; Column 14: Phase calibrator (J2000); Column 15: Flux density of phase calibrator, from GETJY on IF1. Note that the observations of ESO 418-G008 on 2006 October 15 were made without a primary calibrator. We set the flux density of the phase calibrator to the value from 2006 October 10.

TABLE 3
Summary of Data Cube Properties

Source	Weighting	$B_{\rm maj}$ (arcsec)	$B_{\rm min}$ (arcsec)	PA (°)	Noise (mJy beam^{-1})	Image Size (pix)	Pixel Size (arcsec)	Channel Width (km s^{-1})
(1)	(2)	(3)	(4)	(5)	(6)	(7)	(8)	(9)
NGC 0337	NA	25.77	15.06	-18.30	1.7	512	4.0	5.2
	RO	21.23	13.58	-15.37	1.1	512	3.0	10.4
PGC 3853	NA	25.33	15.47	-16.86	1.4	512	4.0	5.2
	RO	20.68	13.89	-16.00	0.99	512	3.0	10.4
PGC 6667	NA	25.73	14.78	3.81	1.2	512	4.0	5.2
	RO	20.57	12.75	3.19	0.82	512	3.0	10.5
ESO 544-G030	NA	27.78	12.01	10.49	1.0	512	4.0	5.2
	RO	13.25	7.64	66.48	0.75	512	2.0	10.4
UGC 1862	NA	23.97	15.32	22.14	1.4	512	4.0	5.2
	RO	19.30	13.88	15.43	0.88	512	3.0	10.4
ESO 418-G008	NA	31.17	13.00	-8.18	1.3	512	4.0	5.2
	RO	13.12	9.99	51.01	0.90	512	2.0	10.4
ESO 555-G027	NA	28.07	12.72	11.28	1.3	512	4.0	5.2
	RO	13.21	7.86	68.75	0.88	512	2.0	10.5
NGC 2805	NA	19.84	16.79	-57.86	1.1	512	4.0	5.2
	RO	17.02	13.76	-54.49	0.85	512	3.0	10.4
ESO 501-G023	NA	30.30	12.51	-14.66	1.4	512	4.0	5.2
	RO	12.32	8.65	-76.74	1.0	512	2.0	10.4
UGC 6446	NA	11.68	11.56	-75.23	0.5	512	3.0	2.6
NGC 3794	NA	19.28	16.86	-57.66	1.0	512	4.0	5.2
	RO	15.72	14.23	-46.75	1.1	512	3.0	5.2
NGC 3906	NA	20.69	16.16	-64.87	0.80	1024	4.0	10.4
	RO	16.24	13.80	-54.94	0.85	1024	3.0	10.4
UGC 6930	NA	19.36	14.81	-62.87	1.1	512	4.0	5.2
	RO	16.18	12.50	-59.72	1.2	512	3.0	5.2
NGC 4519	NA	51.91	18.77	-34.50	1.3	512	4.0	5.2
	RO	17.69	14.43	53.53	1.4	512	3.0	5.2
NGC 4561	NA	19.97	16.23	79.10	1.5	512	4.0	5.2
	RO	16.23	13.83	-86.37	1.3	512	3.0	10.4
NGC 4713	NA	18.99	18.40	64.18	1.1	512	4.0	5.2
	RO	16.63	15.06	-73.24	1.2	512	3.0	5.2
NGC 4942	NA	21.52	18.91	9.28	1.1	512	4.0	5.2
	RO	17.42	16.29	3.45	1.2	512	3.0	5.2
NGC 5964	NA	20.15	17.29	-7.11	0.64	512	4.0	5.2
	RO	16.09	14.94	-5.03	0.52	512	3.0	10.4
NGC 6509	NA	18.61	17.91	4.03	1.0	512	4.0	5.2
	RO	15.93	14.95	-67.69	1.2	512	3.0	5.2
IC 1291	NA	19.62	16.02	-78.49	1.2	2048	4.0	5.2
	RO	16.76	13.46	-69.28	1.2	2048	3.0	5.2

Note. — Column 1: Object name; Column 2: Image weighting: NA uses *robust* = 5 in IMAGR; RO uses *robust* = 0.5 in IMAGR; Column 3: Beam major axis FWHM; Column 4: Beam minor axis FWHM; Column 5: Position angle of beam major axis; Column 6: Image noise; Column 7: Spatial dimensions of data cube; Column 8: Pixel size; Column 9: Channel width. See Section 3.1 for more details.

TABLE 4
H I Flux, Mass, and Line Width Measurements

Source	$S_{\rm HI}$ ($\rm Jy\,km\,s^{-1}$)	$M_{\rm HI}$ ($10^8\,M_\odot$)	$S_{\rm HI}^{\rm HIPASS}$ ($\rm Jy\,km\,s^{-1}$)	$S_{\rm HI}^{\rm Springob}$ ($\rm Jy\,km\,s^{-1}$)	W_{20} ($\rm km\,s^{-1}$)	$W_{20}^{\rm HIPASS}$ ($\rm km\,s^{-1}$)	$W_{20}^{\rm RC3}$ ($\rm km\,s^{-1}$)
(1)	(2)	(3)	(4)	(5)	(6)	(7)	(8)
NGC 0337	75.6	76.4	50.6	50.84	261	277.3	261 ± 6
PGC 3853	125.3	38.4	61.9	...	192	194.5	182 ± 7
PGC 6667	33.3	47.6	21.4	...	198	219.8	213 ± 16
ESO 544-G030	11.2	5.09	8.4	...	146	148.4	104 ± 16
UGC 1862	4.7	5.47	3.4	3.51	125	121.6	...
ESO 418-G008	8.2	10.7	9.6	...	140	185.4	...
ESO 555-G027	34.0	47.3	24.0	...	162	180.8	168 ± 16
NGC 2805	120.3	223	...	...	120	...	118 ± 4
ESO 501-G023	24.9	2.89	29.3	...	83	88.3	79 ± 16
UGC 6446	43.8	33.5	...	34.55	150	...	143 ± 6
NGC 3794	19.4	16.8	...	20.32	182	...	187 ± 6
NGC 3906	4.8	3.76	...	11.38	49	...	48 ± 6
UGC 6930	43.5	29.7	...	...	140	...	133 ± 8
NGC 4519	50.9	46.2	...	...	218	...	209 ± 6
NGC 4561	27.5	9.83	...	26.16	171	...	140 ± 4
NGC 4713	36.0	18.8	...	55.70	176	...	192 ± 5
NGC 4942	10.1	19.4	11.4	...	177	203.4	159 ± 16
NGC 5964	54.5	78.4	...	40.84	208	...	192 ± 4
NGC 6509	30.4	> 57.0	...	31.02	266	...	283 ± 9
IC 1291	14.5	34.0	...	23.16	209	...	226 ± 7

Note. — Column 1: Object name; Column 2: Integrated HI line flux. We assign an error of 12% to our fluxes to account for flux calibration and aliasing. Column 3: Total HI mass. Note that the NGC 6509 mass is a lower limit due to absorption. See Section 5 for details; Column 4: Integrated flux from HIPASS, which uses the single-dish 64-m Parkes telescope (Meyer et al. 2004); Column 5: Integrated flux from a variety of large single-dish telescopes, compiled in Springob et al. (2005); Column 6: Width of the HI line at 20% of the peak flux density, corrected for the spectral resolution assuming $W_{20} = \sqrt{W_{20,\rm obs}^2 - W_{20,\rm res}^2}$, $W_{20,\rm res} = W_{50,\rm res}\sqrt{\ln 5/\ln 2}$, and $W_{50,\rm res} = \Delta$v, where $W_{50,\rm res}$ is the spectral resolution FWHM, Δv is the channel width of the naturally-weighted data cube from column 9 of Table 3, $W_{20,\rm res}$ is the spectral resolution at 20% of the peak flux density, and $W_{20,\rm obs}$ is the observed width at 20% of the peak flux density. These assumptions are appropriate for data that has been Hanning smoothed and for which the spectral response function is Gaussian. W_{20} is not corrected for turbulent broadening or inclination. The uncertainty in W_{20} is the channel width, which is $5\,\rm km\,s^{-1}$ for all objects except UGC 6446 and NGC 3906, where the uncertainty is $3\,\rm km\,s^{-1}$ and $10\,\rm km\,s^{-1}$, respectively. Column 7: W_{20} from Meyer et al. (2004); Column 8: W_{20} values compiled in de Vaucouleurs et al. (1991).

TABLE 5
Comparison of Kinematic and Photometric Parameters

	Center			Position Angle			Inclination		
Source	RA (J2000.0) (hh:mm:ss.s)	DEC (J2000.0) (dd:mm:ss)	Offset (arcsec)	ROTCUR (°)	IRAC (°)	RC3 (°)	ROTCUR (°)	IRAC (°)	RC3 (°)
(1)	(2)	(3)	(4)	(5)	(6)	(7)	(8)	(9)	(10)
NGC 0337	00:59:50.0	-07:34:42	3.2	119.0	118.4	130	49.9	43.7	51
PGC 3853	01:05:05.1	-06:12:58	12.4	106.2	105.3	...	40.7	41.4	32
PGC 6667	01:49:10.6	-10:03:48	3.7	125.2	122.9	...	48.0	34.0	37
ESO 544-G030	02:14:57.6	-20:12:44	11.2	106.1	107.6	103	12.0	48.5	51
UGC 1862	02:24:24.8	-02:09:47	3.8	21.4	21.7	10	39.0	43.4	39
ESO 418-G008	03:31:30.8	-30:12:46	0.8	317.9	321.6	329	49.9	55.6	49
ESO 555-G027	06:03:35.9	-20:39:10	27.6	221.5	245.3	230	31.0	20.9	36
NGC 2805	...	...	...	300.0	...	305	37.5	...	41
ESO 501-G023	...	...	...	223.6	...	194	49.0	...	37
UGC 6446	...	...	...	189.4	...	190	52.5	...	50
NGC 3794	11:40:54.4	+56:12:07	0.8	123.1	116.2	120	54.2	54.8	50
NGC 3906	11:49:39.8	+48:25:27	11.1	183.1	185.0	...	40.0	16.5	27
UGC 6930	11:57:16.8	+49:16:58	3.5	39.5	24.2	...	31.3	25.4	51
NGC 4519	12:33:30.4	+08:39:18	9.6	354.9	326.3	325	42.5	42.4	39
NGC 4561	12:36:08.3	+19:19:24	7.1	221.3	227.3	210	33.0	34.3	32
NGC 4713	12:49:57.5	+05:18:39	4.7	274.1	274.0	280	41.4	45.2	51
NGC 4942	13:04:19.1	-07:38:56	1.1	137.3	146.9	145	45.1	37.3	45
NGC 5964	15:37:36.2	+05:58:24	3.4	136.7	160.5	145	37.7	31.9	39
NGC 6509	17:59:25.3	+06:17:13	0.5	280.8	286.2	285	47.1	41.0	42
IC 1291	...	...	...	131.4	...	210	28.0	...	34

Note. — Column 1: Object name. Columns 2 and 3: RA and DEC of the photometric center, derived from ellipse fits on the Channel 1 IRAC data. Empty columns here and in subsequent IRAC columns correspond to objects where the ellipse fits did not converge. Column 4: Offset of the kinematic center determined in the rotation curve analysis relative to the photometric center. Column 5: PA derived from the rotation curve analysis (degrees N to E to receding side). Column 6: PA derived from ellipse fits on the Channel 1 IRAC data. Column 7: RC3 PA, converted to the definition used in column 5 when necessary. Column 8: Inclination derived from the rotation curve analysis. Column 9: Inclination derived from ellipse fits on the Channel 1 IRAC data. Column 10: RC3 inclination.

TABLE 6
Final Kinematic Parameters

Source	V_{sys} ($km\,s^{-1}$)	PA (°)	i (°)	Center RA (hh:mm:ss.s)	Center DEC (dd:mm:ss)	Center error (arcsec)	v_{circ} ($km\,s^{-1}$)	RC Quality Assessment	Note
(1)	(2)	(3)	(4)	(5)	(6)	(7)	(8)	(9)	(10)
NGC 0337	1646 ± 2	118 ± 5	44 ± 2	00:59:50.0	-07:34:42	3	145^{+5}_{-4}	A	i,c,p
PGC 3853	1094.7 ± 0.4	105.3 ± 0.2	41.4 ± 1.1	01:05:04.8	-06:12:47	1.3	$128.1^{+1.6}_{-2}$	A	i,p
PGC 6667	1989.2 ± 0.6	122.9 ± 1.8	34.0 ± 1.1	01:49:10.5	-10:03:45	1.1	155^{+4}_{-4}	A	i,p
ESO 544-G030	1608.4 ± 1.0	107.6 ± 1.1	48.5 ± 1.2	02:14:56.9	-20:12:40	3	$100.9^{+1.4}_{-2}$	C	i,p
UGC 1862	1382.9 ± 0.4	21.7 ± 1.7	43 ± 4	2:24:24.8	-2:09:47	1.8	55^{+6}_{-5}	C	i,c,p
ESO 418-G008	1195.4 ± 0.3	317.9 ± 1.1	55.6 ± 1.4	03:31:30.8	-30:12:46	1.2	$74.1^{+0.6}_{-0.6}$	B	i,c
ESO 555-G027	1978.7 ± 0.4	221.5 ± 0.3	21 ± 4	06:03:35.9	-20:39:10	1.9	190^{+40}_{-30}	A	i,c
NGC 2805	1732.6 ± 0.6	300 ± 3	38 ± 4	09:20:19.6	+64:06:02	7	81^{+7}_{-8}	A	...
ESO 501-G023	1046.8 ± 0.7	224 ± 2	37 ± 12	10:35:23.0	-24:45:19	9	46^{+18}_{-8}	A	i*
UGC 6446	645.5 ± 0.6	189.4 ± 0.5	52.5 ± 1.9	11:26:40.6	+53:44:52	1.0	$79.7^{+1.3}_{-0.8}$	A	...
NGC 3794	1384.9 ± 0.7	123.1 ± 1.1	54.8 ± 1.3	11:40:54.4	+56:12:07	0.11	$103.3^{+1.1}_{-1.0}$	A	i,c
NGC 3906	959.44 ± 0.7	180 ± 20	16 ± 5	11:49:40.4	+48:25:36	7	65^{+30}_{-16}	C	i,p
UGC 6930	776.7 ± 0.7	39.5 ± 0.5	25 ± 4	11:57:16.8	+49:16:58	4	121^{+20}_{-15}	A	i,c
NGC 4519	1218.1 ± 1.0	355 ± 2	42 ± 3	12:33:30.4	+08:39:18	1.3	112^{+8}_{-7}	A	i,c
NGC 4561	1402.2 ± 0.9	227 ± 8	34 ± 4	12:36:08.3	+19:19:24	3	57^{+6}_{-5}	B	i,c,p
NGC 4713	654.5 ± 0.5	274.0 ± 0.6	45.2 ± 1.2	12:49:57.7	+05:18:43	1.0	$110.9^{+2}_{-1.8}$	A	i,p
NGC 4942	1741 ± 2	137.3 ± 0.8	37 ± 2	13:04:19.1	-07:38:56	3	124^{+6}_{-5}	A	i,c
NGC 5964	1447.1 ± 1.2	136.7 ± 1.2	32 ± 3	15:37:36.2	+05:58:24	5	168^{+18}_{-14}	A	i,c
NGC 6509	1811.0 ± 0.4	280.8 ± 1.1	41 ± 4	17:59:25.3	+06:17:13	4	153^{+12}_{-9}	A	i,c
IC 1291	1951.0 ± 1.1	131 ± 2	28 ± 3	18:33:52.5	+49:16:49	2	189^{+17}_{-14}	B	...

Note. — Column 1: Object name. Column 2: Systemic velocity derived from the rotation curve analysis, corrected to the heliocentric reference frame. Column 3: Position angle of the major axis (degrees N to E to receding side). For columns 3-6, the values are either from the rotation curve analysis or from ellipse fits on the Channel 1 IRAC data. See column 10 and Section 4.3 for more information. Column 4: Inclination. Column 5 and 6: RA and DEC (J2000.0) of the galaxy center. Column 7: Error on the galaxy center. Column 8: Circular velocity, defined as the maximum velocity in the rotation curve fits. Column 9: Rotation curve quality assessment. A refers to galaxies with clear turnovers in the rotation curve, B refers to galaxies with a hint of a turnover, and C refers galaxies with no turnover. Column 10: The note lists which final parameters are derived from the IRAC analysis (i=inclination, p=PA, c=center). The remaining parameters are from the rotation curve analysis.
* The inclination for ESO 501-G023 is from RC3.

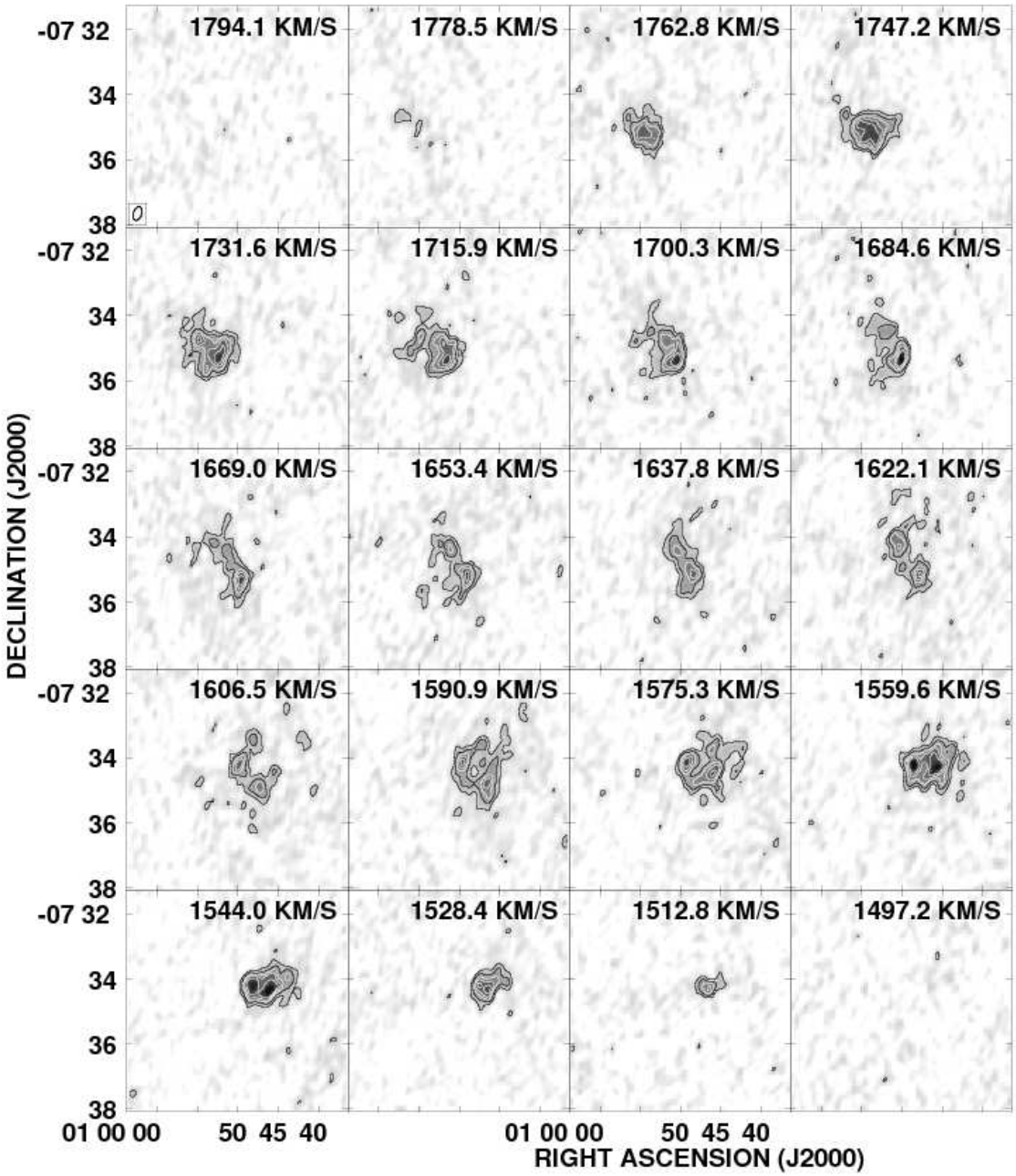

FIG. 1.— NGC 0337 channel maps based on the naturally-weighted cube that has not been blanked. The contours begin at 3σ and end at 11σ, in steps of 2σ, where σ is the image noise from Column 6 of Table 3. The grayscale spans -0.02 to 28.33 mJy beam^{-1}. Every third channel is shown and the channel width is 5.2 km s^{-1}. The beam size is shown in the lower left corner of the top left panel and the velocity of the channel is shown in the upper right of each panel.

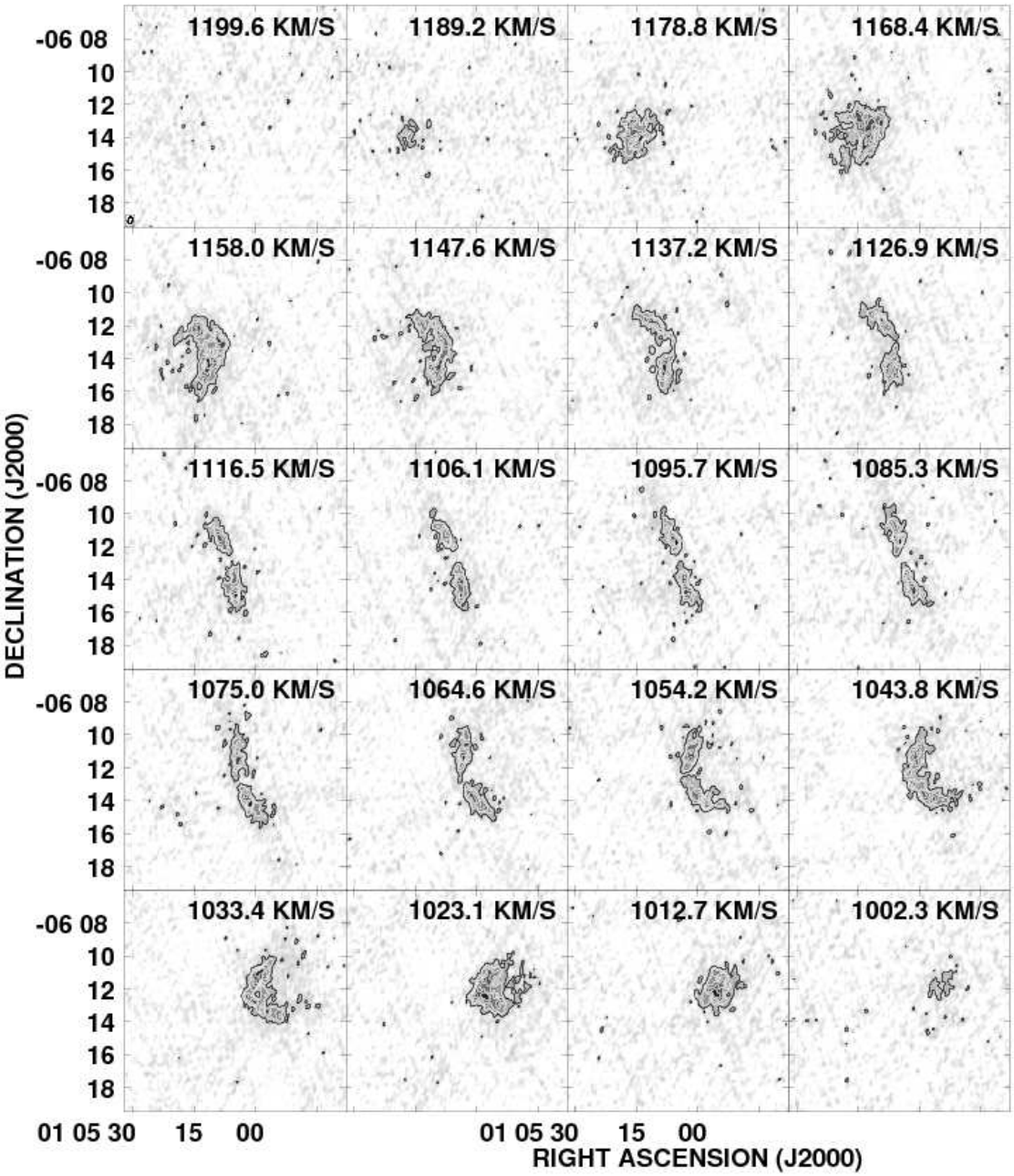

FIG. 2.— As in Figure 1, but for PGC 3853. The grayscale spans -0.02 to 20.30 mJy beam^{-1}. Every second channel is shown and the channel width is 5.2 km s^{-1}.

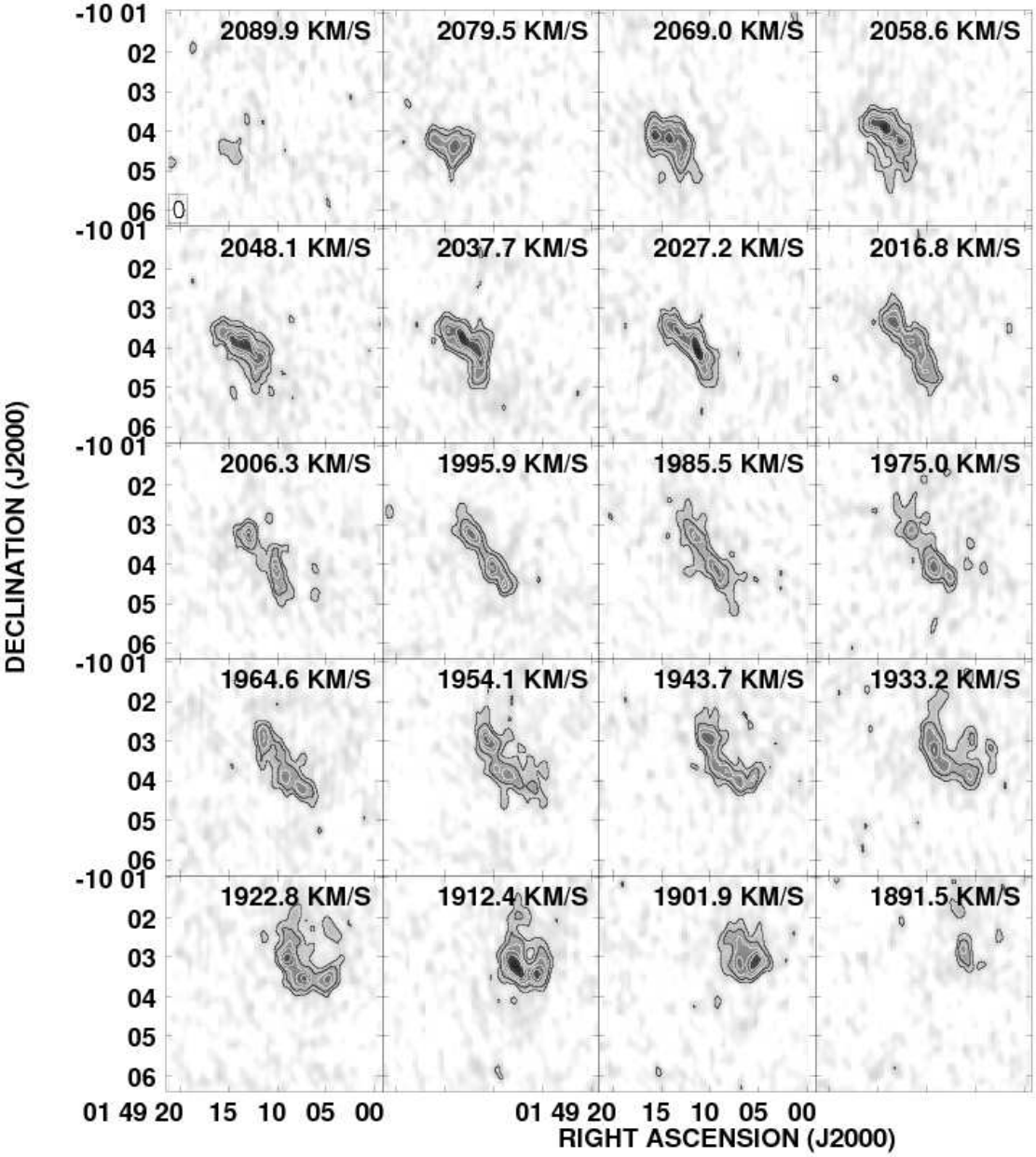

FIG. 3.— As in Figure 1, but for PGC 6667. The grayscale spans -0.02 to 21.13 mJy beam^{-1}. Every second channel is shown and the channel width is 5.2 km s^{-1}.

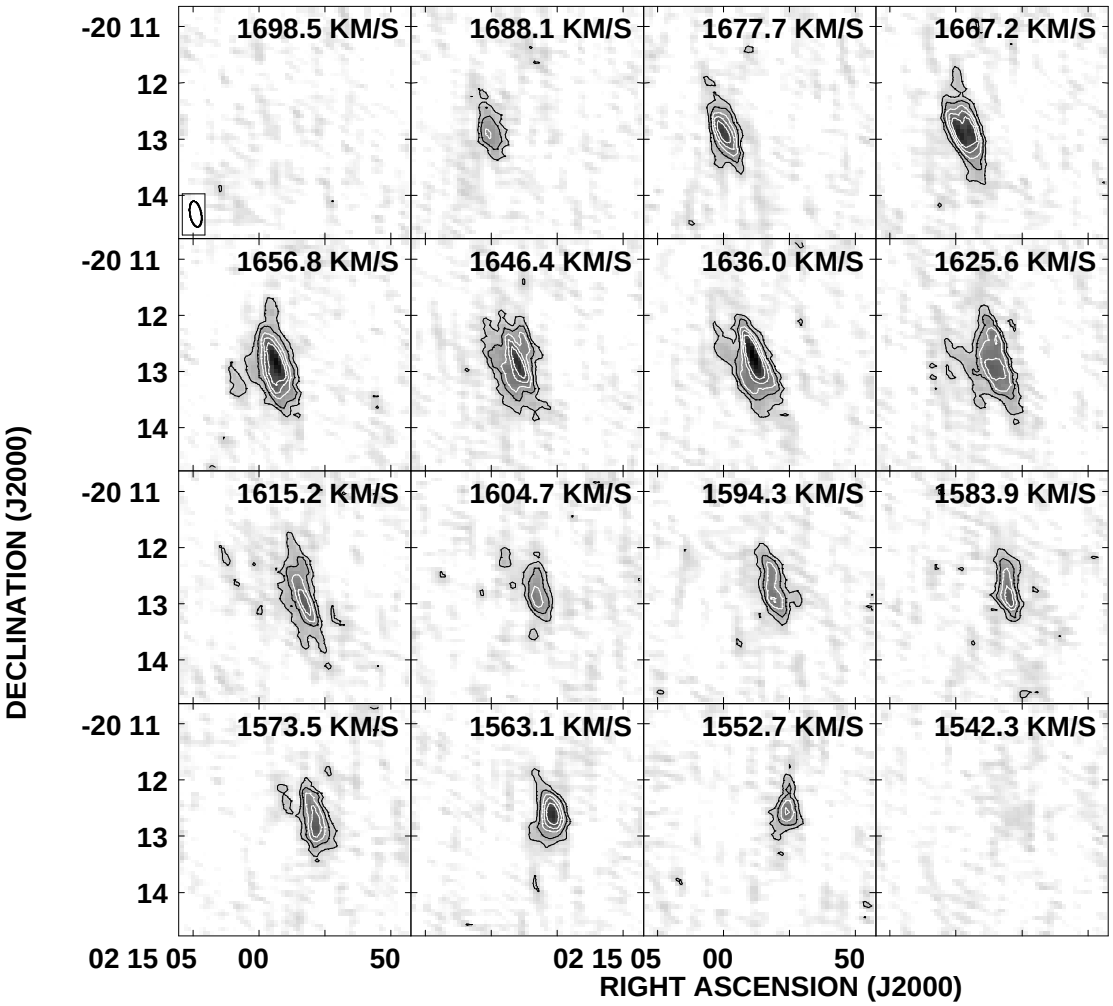

FIG. 4.— As in Figure 1, but for ESO 544-G030. The grayscale spans -0.02 to 16.35 mJy beam^{-1}. Every second channel is shown and the channel width is 5.2 km s^{-1}.

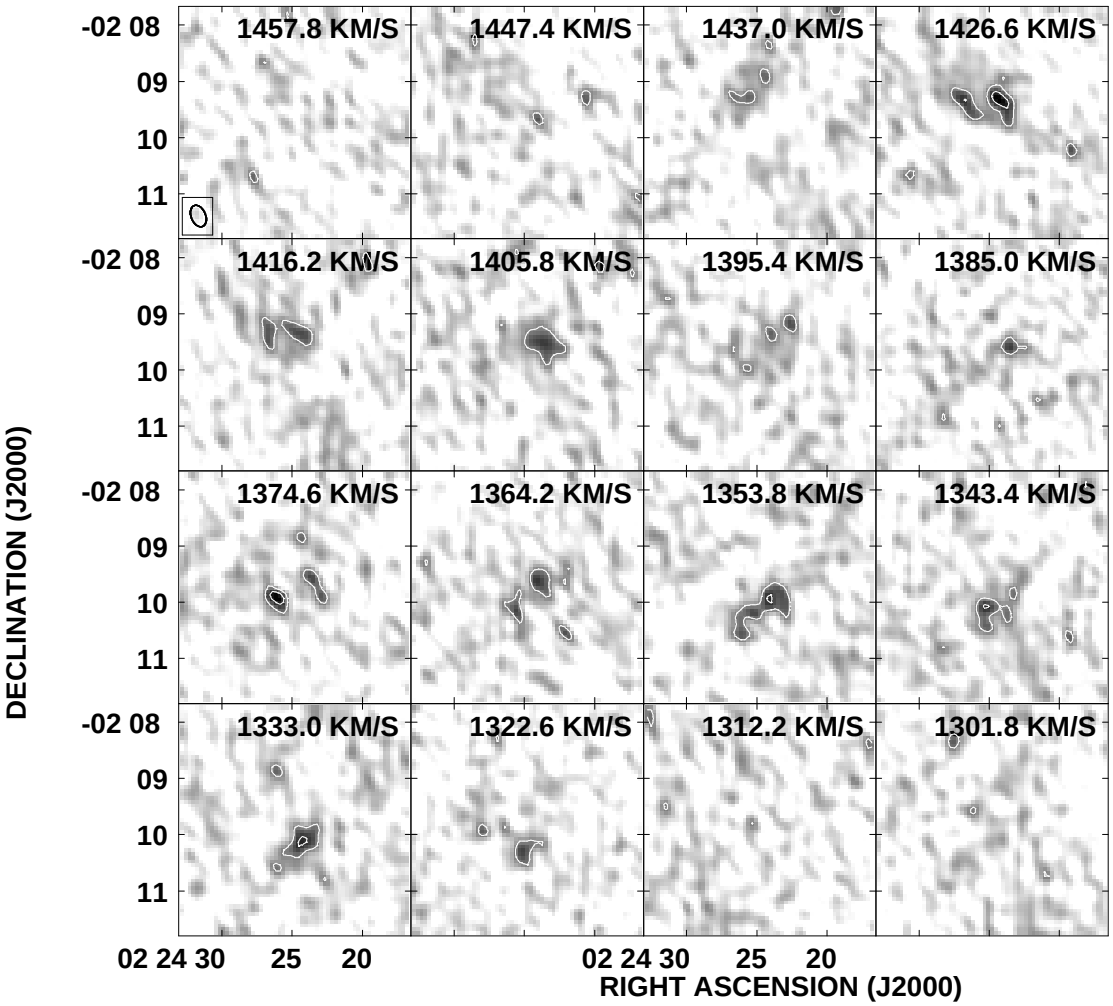

FIG. 5.— As in Figure 1, but for UGC 1862. The grayscale spans -0.02 to 8.43 mJy beam^{-1}. Every second channel is shown and the channel width is 5.2 km s^{-1}.

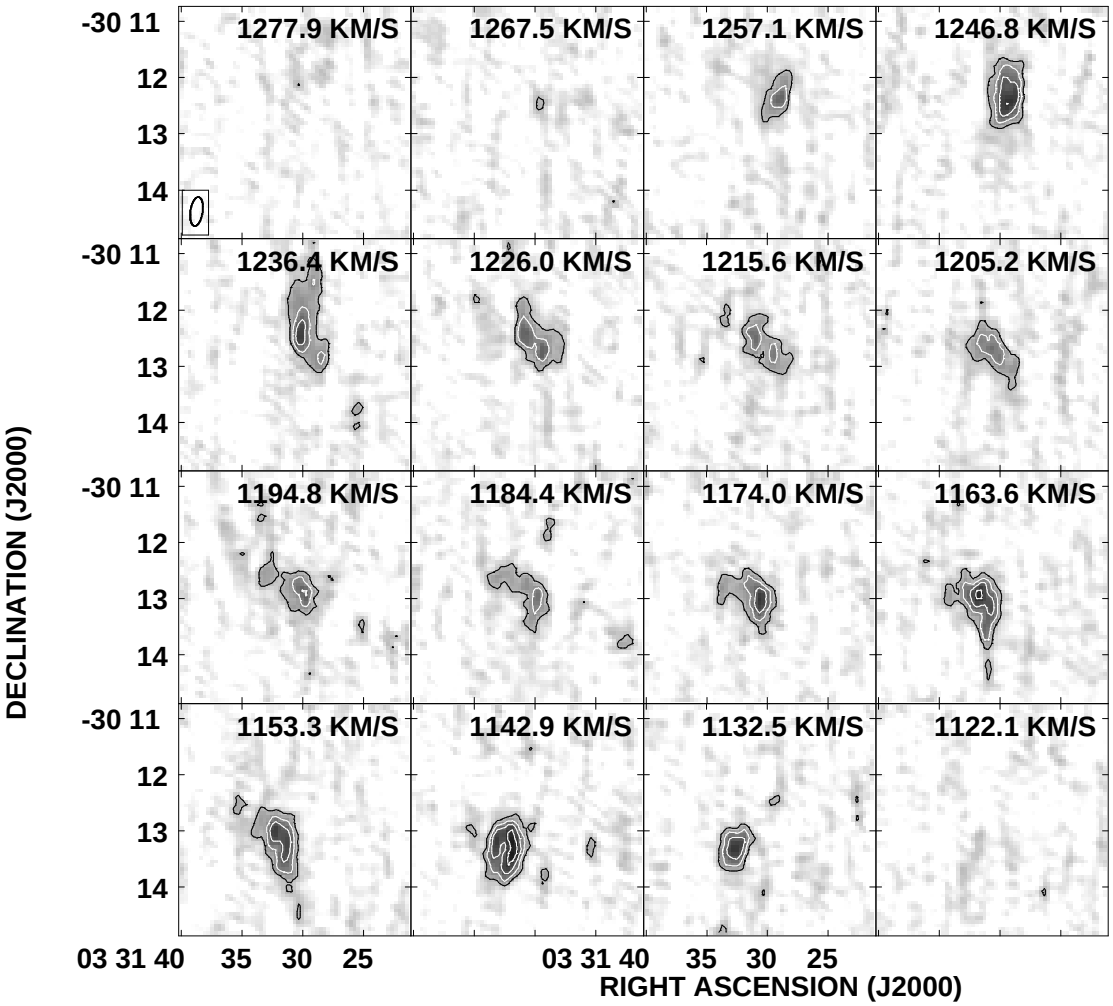

FIG. 6.— As in Figure 1, but for ESO 418-G008. The grayscale spans -0.02 to 14.61 mJy beam^{-1}. Every second channel is shown and the channel width is 5.2 km s^{-1}.

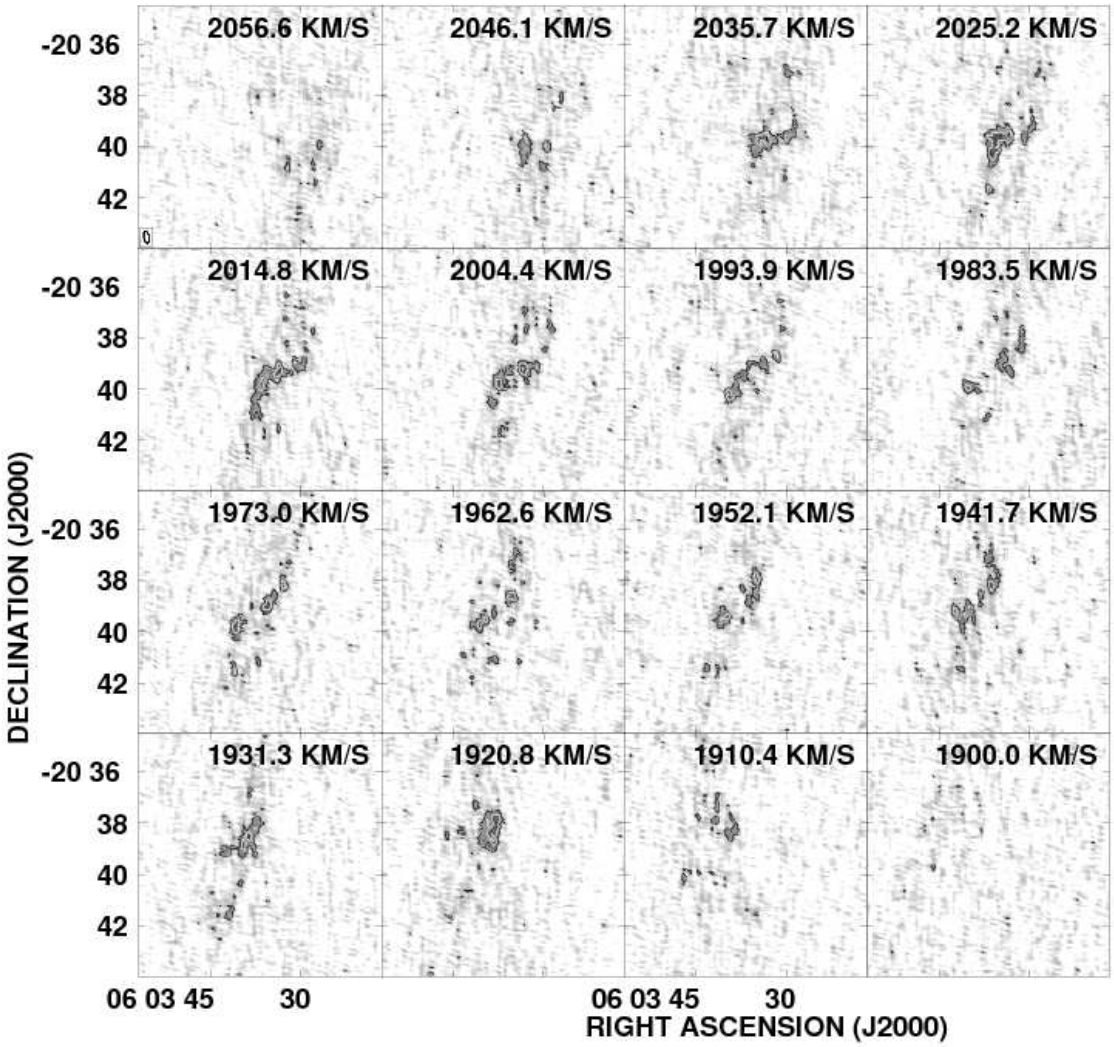

FIG. 7.— As in Figure 1, but for ESO 555-G027. The grayscale spans -0.02 to 12.09 mJy beam^{-1}. Every second channel is shown and the channel width is 5.2 km s^{-1}.

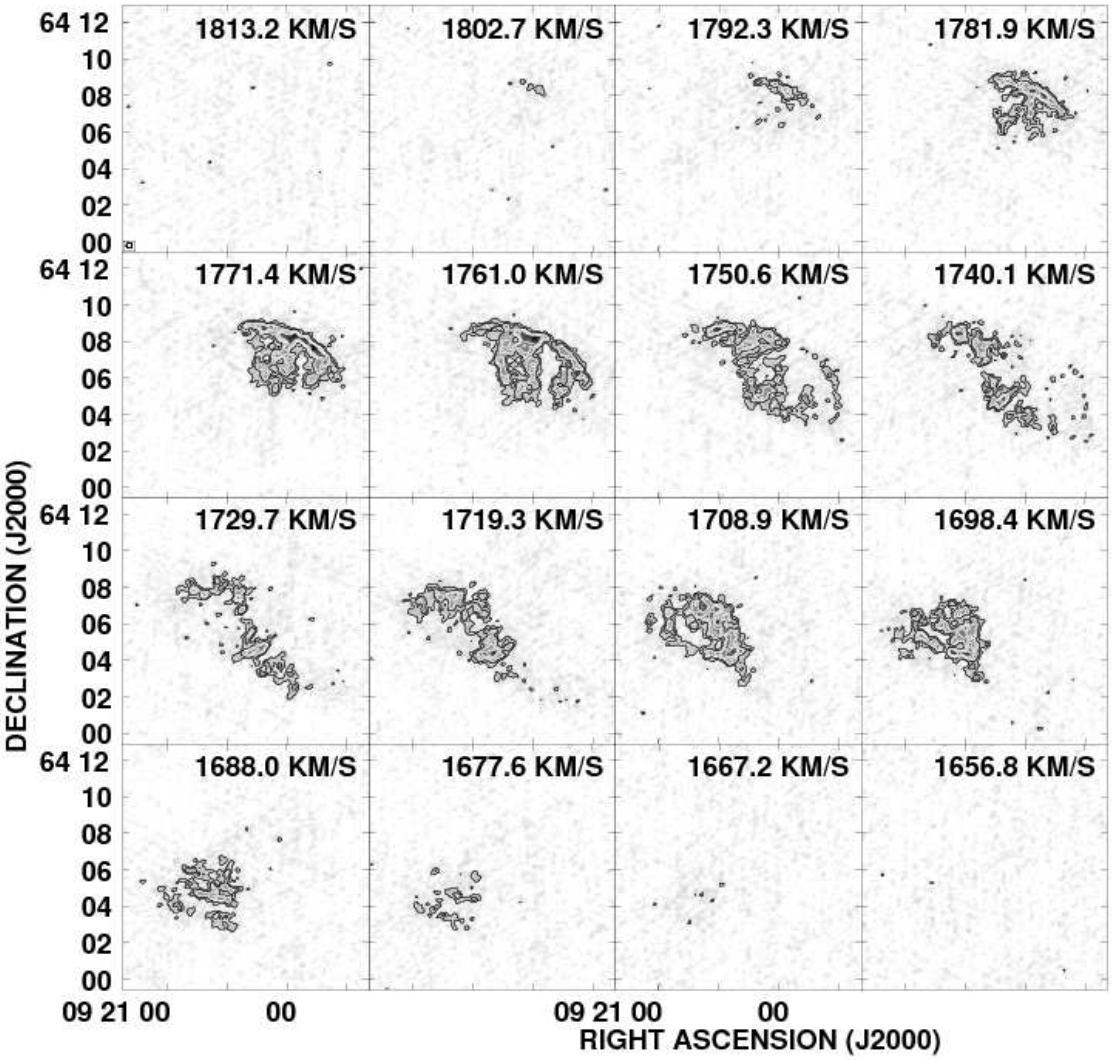

FIG. 8.— As in Figure 1, but for NGC 2805. The grayscale spans -0.02 to 21.31 mJy beam^{-1}. Every second channel is shown and the channel width is 5.2 km s^{-1}.

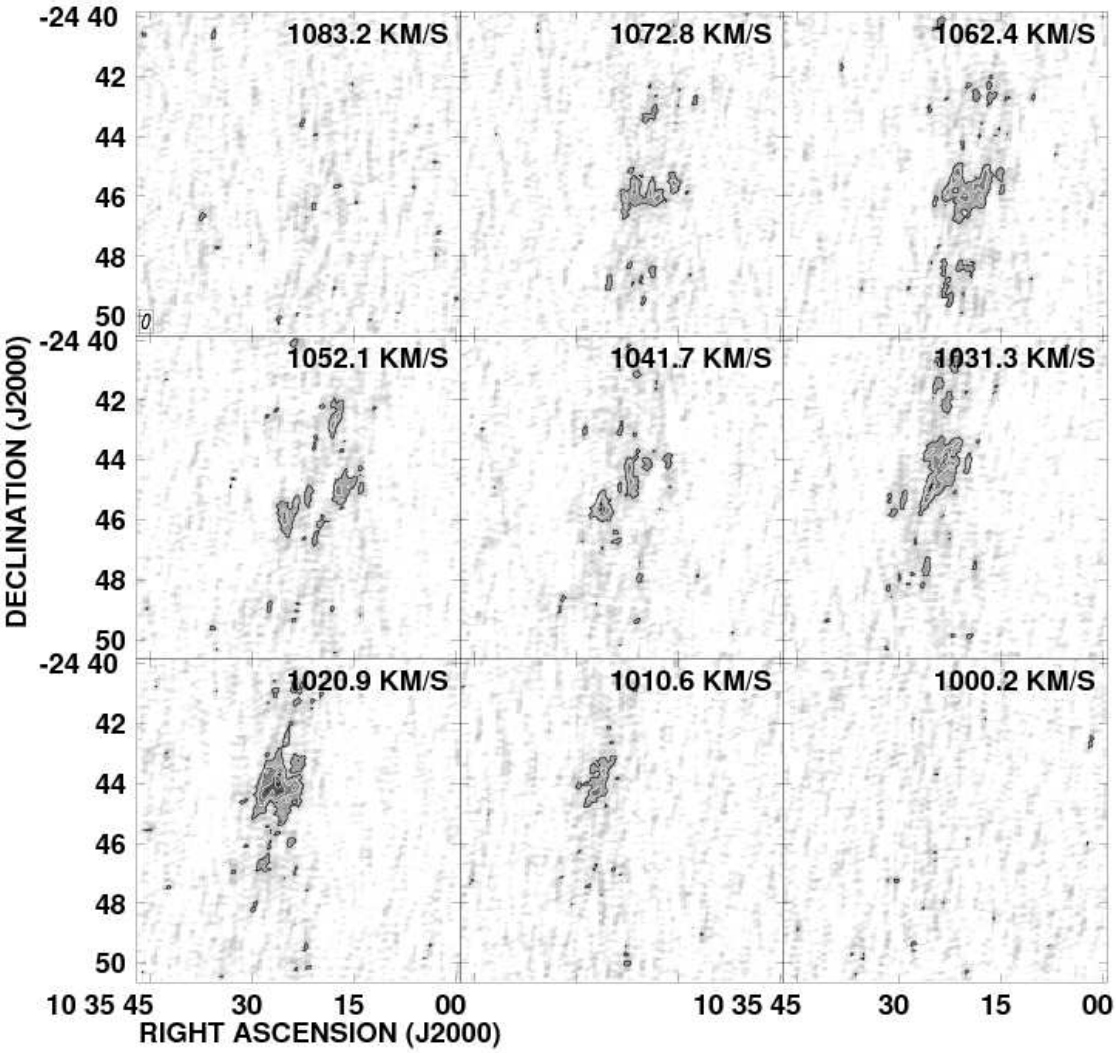

FIG. 9.— As in Figure 1, but for ESO 501-G023. The grayscale spans -0.02 to 16.40 mJy beam^{-1}. Every second channel is shown and the channel width is 5.2 km s^{-1}.

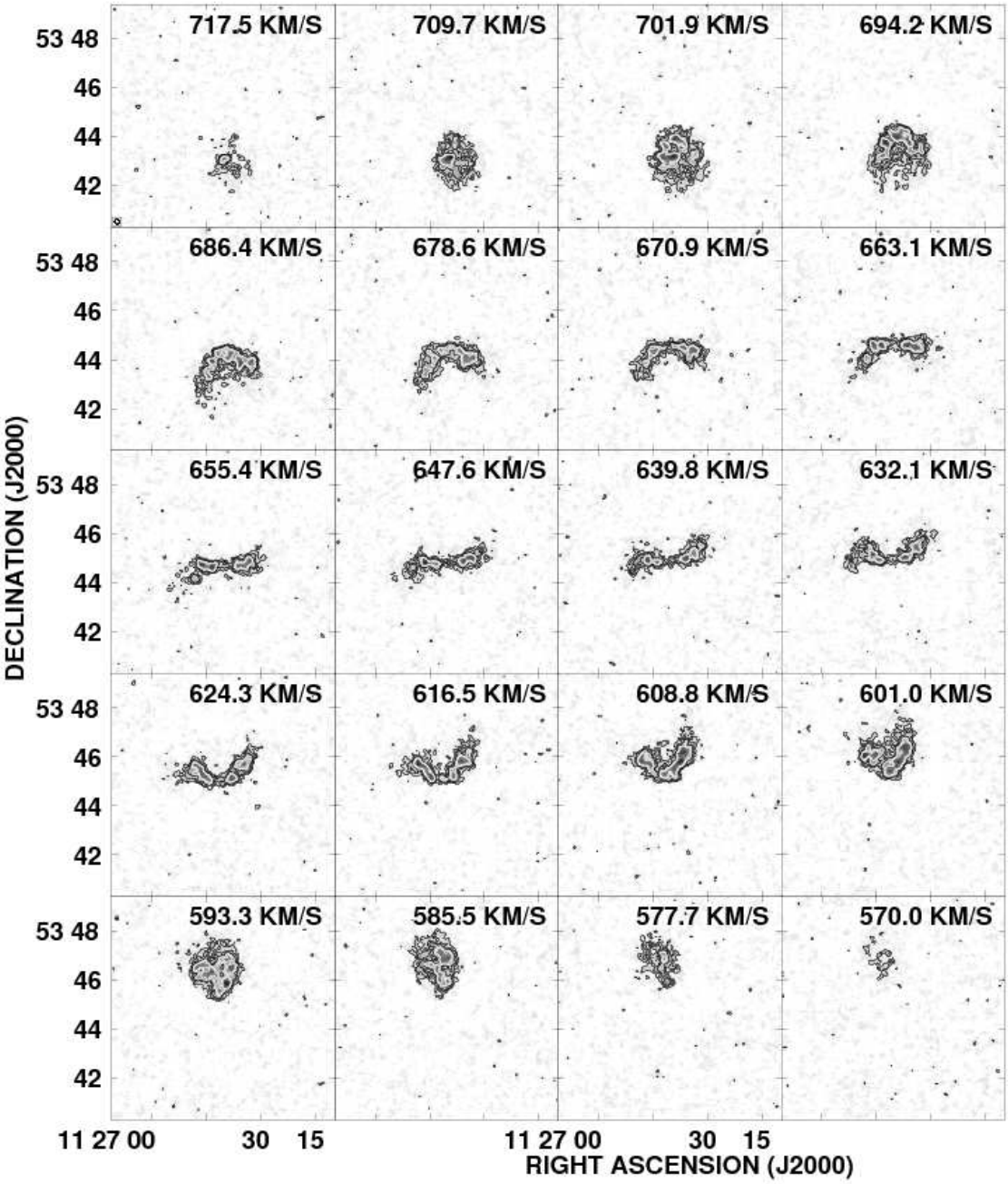

FIG. 10.— As in Figure 1, but for UGC 6446. The grayscale spans -0.02 to 12.52 mJy beam^{-1}. Every third channel is shown and the channel width is 2.6 km s^{-1}.

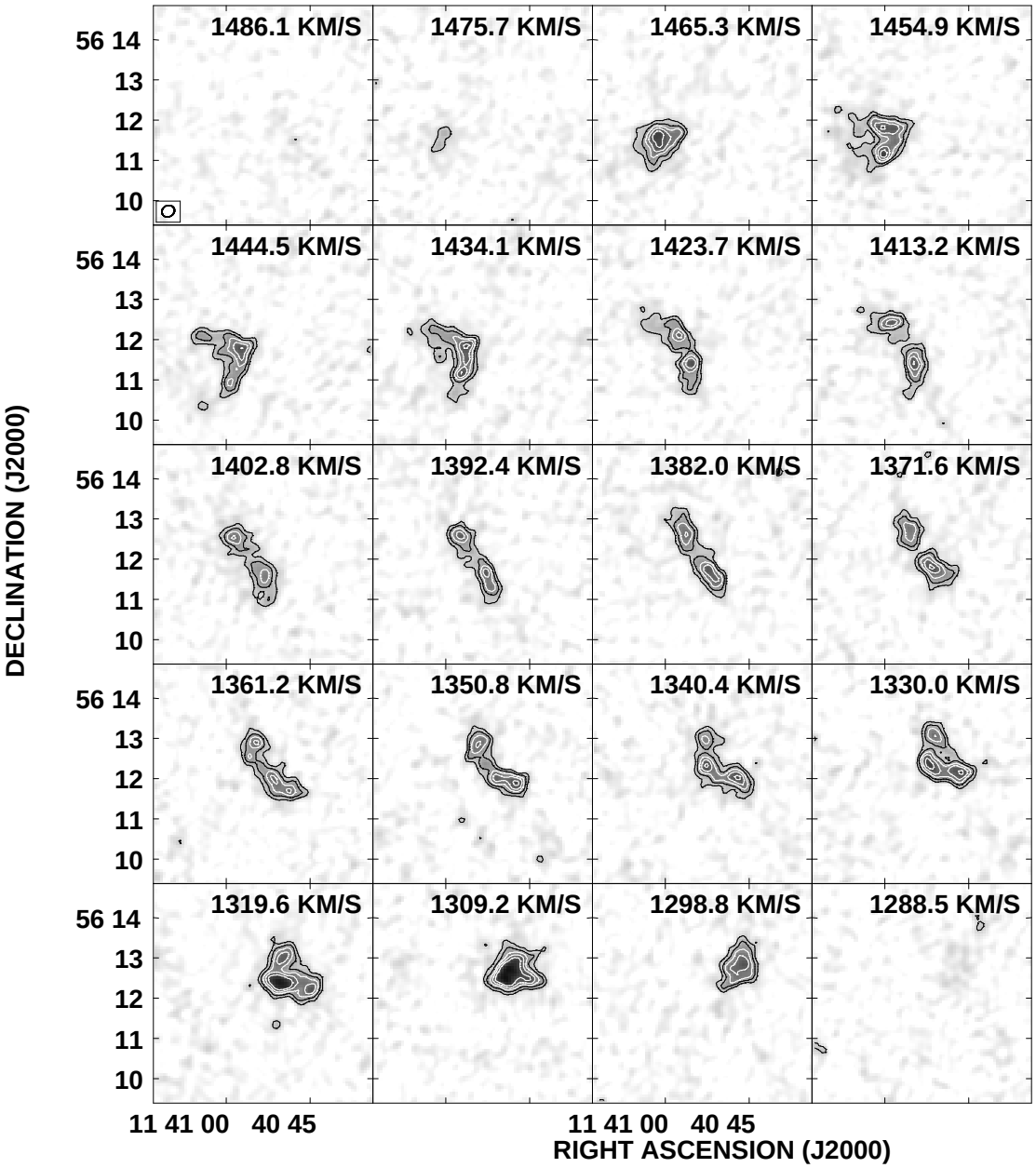

FIG. 11.— As in Figure 1, but for NGC 3794. The grayscale spans -0.02 to 15.67 mJy beam^{-1}. Every second channel is shown and the channel width is 5.2 km s^{-1}.

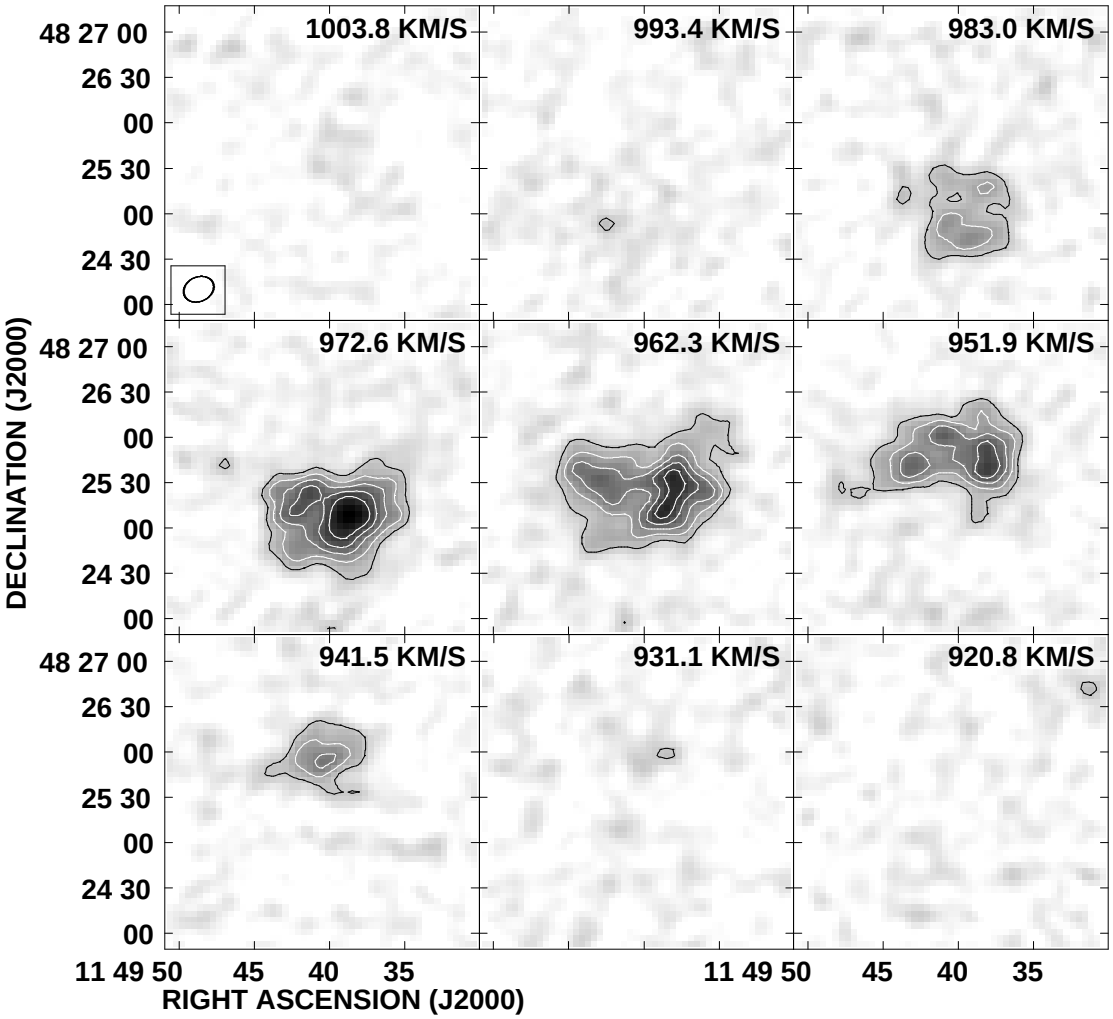

FIG. 12.— As in Figure 1, but for NGC 3906. The grayscale spans -0.02 to 11.48 mJy beam^{-1}. Every channel is shown and the channel width is 10.4 km s^{-1}.

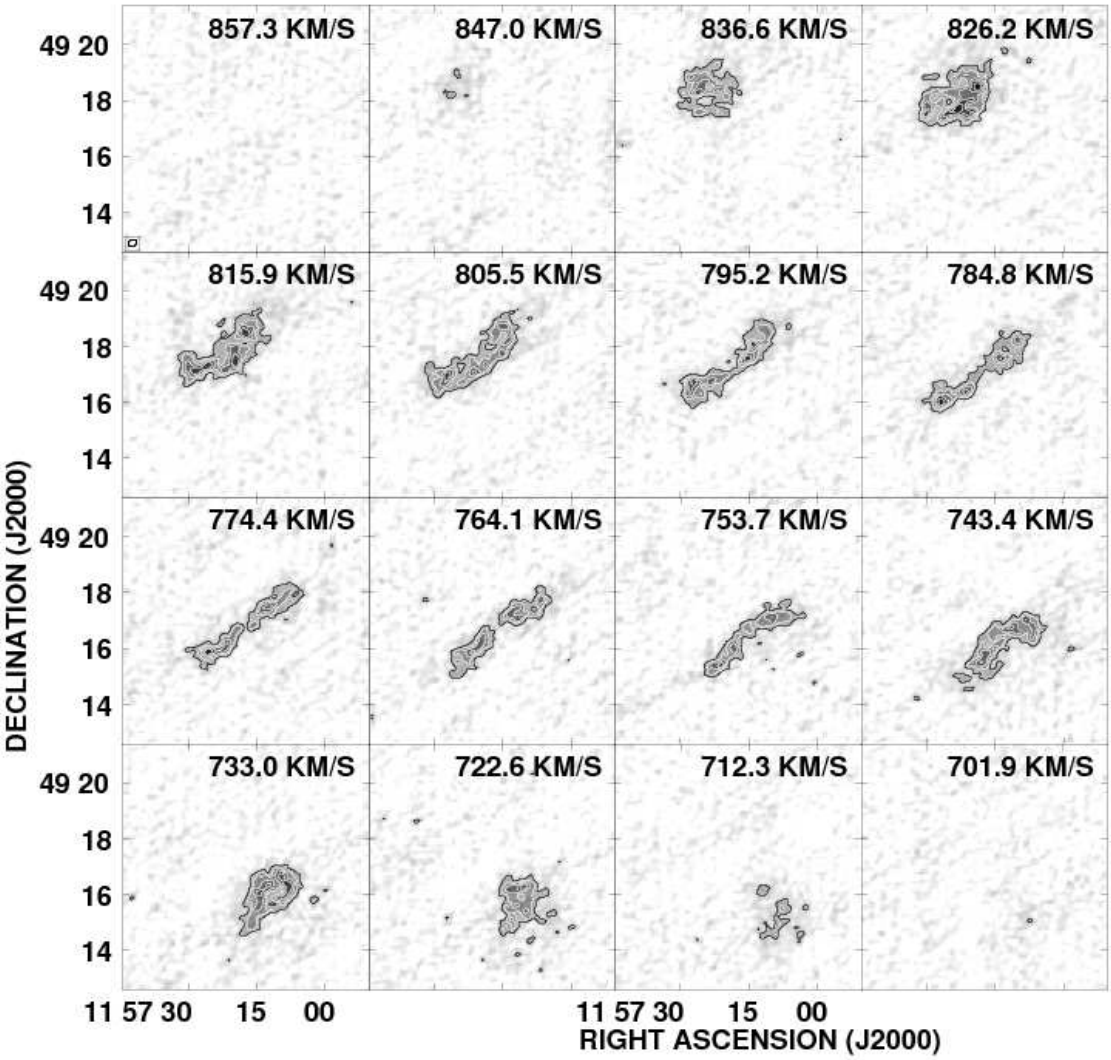

FIG. 13.— As in Figure 1, but for UGC 6930. The grayscale spans -0.02 to 15.06 mJy beam^{-1}. Every second channel is shown and the channel width is 5.2 km s^{-1}.

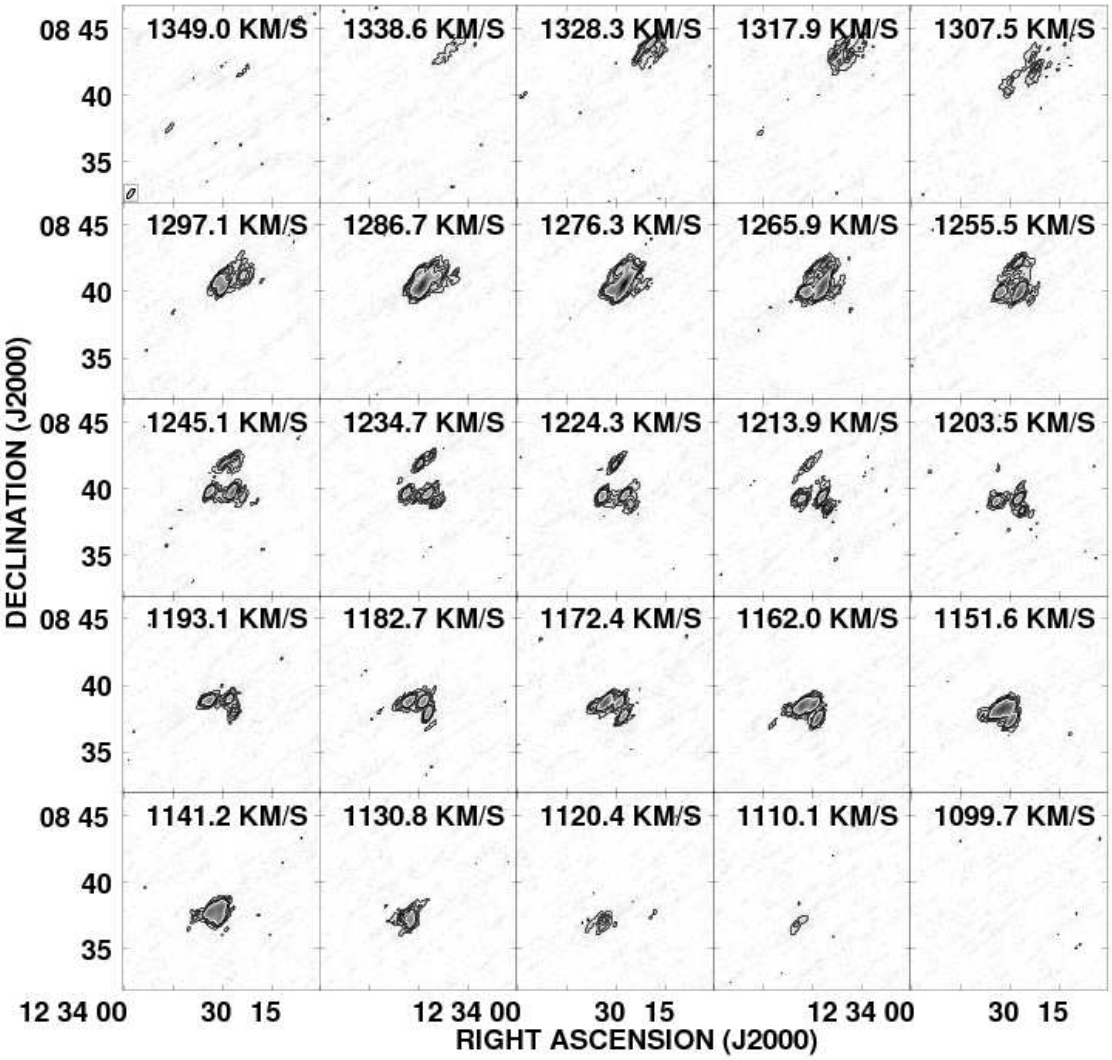

FIG. 14.— As in Figure 1, but for NGC 4519. The grayscale spans -0.02 to 41.37 mJy beam^{-1}. Every second channel is shown and the channel width is 5.2 km s^{-1}.

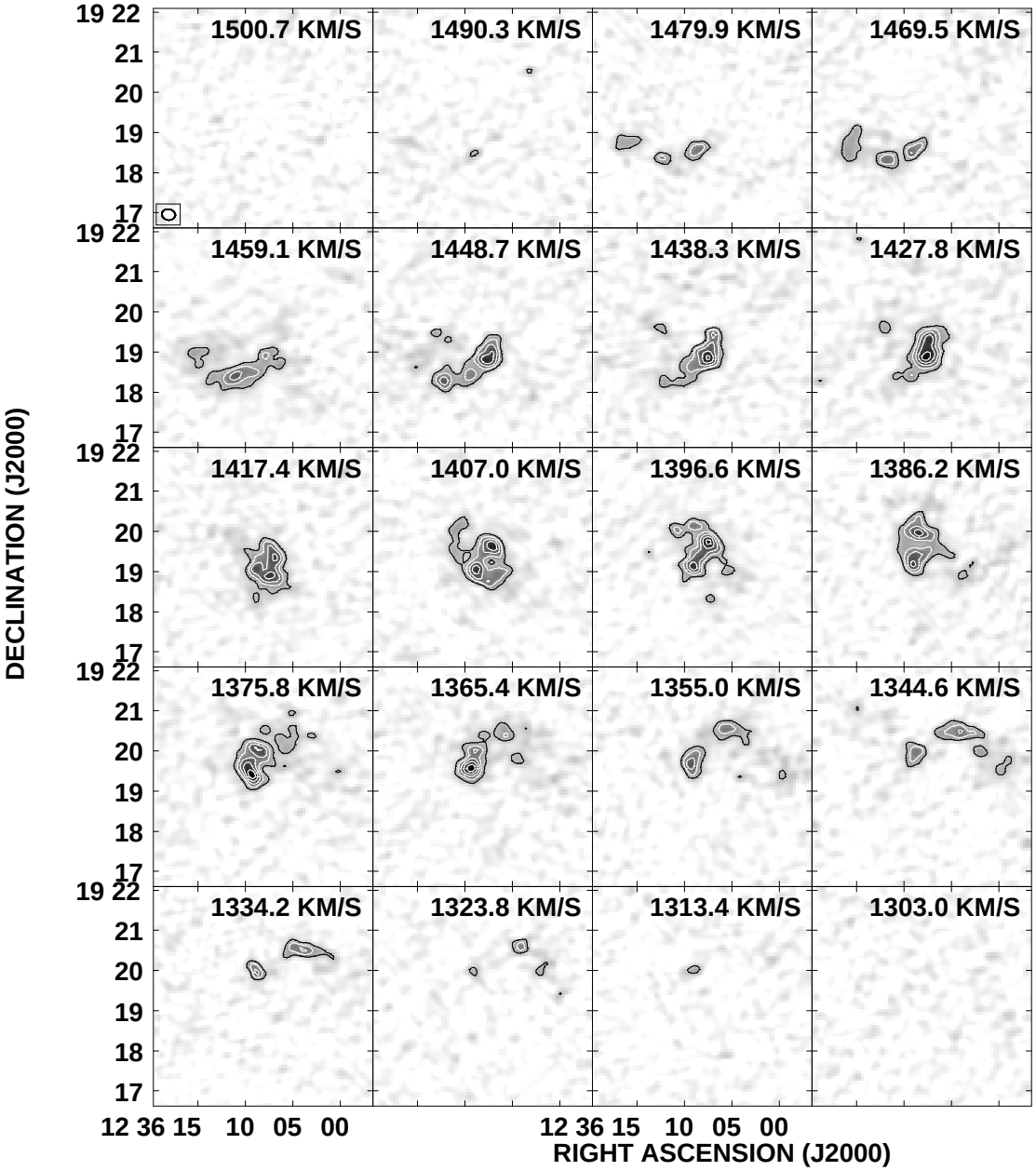

FIG. 15.— As in Figure 1, but for NGC 4561. The grayscale spans -0.02 to 18.81 mJy beam^{-1}. Every second channel is shown and the channel width is 5.2 km s^{-1}.

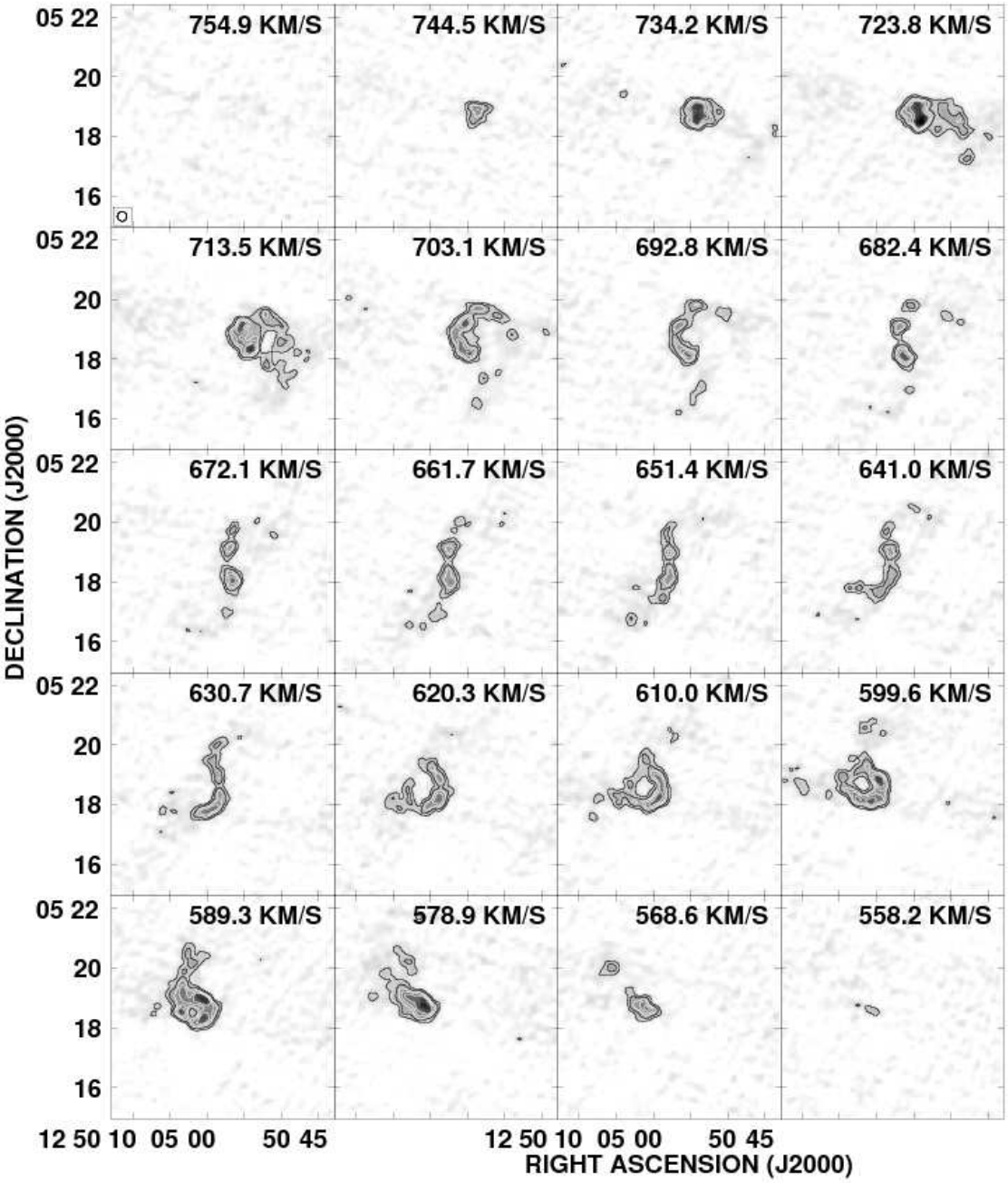

FIG. 16.— As in Figure 1, but for NGC 4713. The grayscale spans -0.02 to 21.68 mJy beam^{-1}. Every second channel is shown and the channel width is 5.2 km s^{-1}.

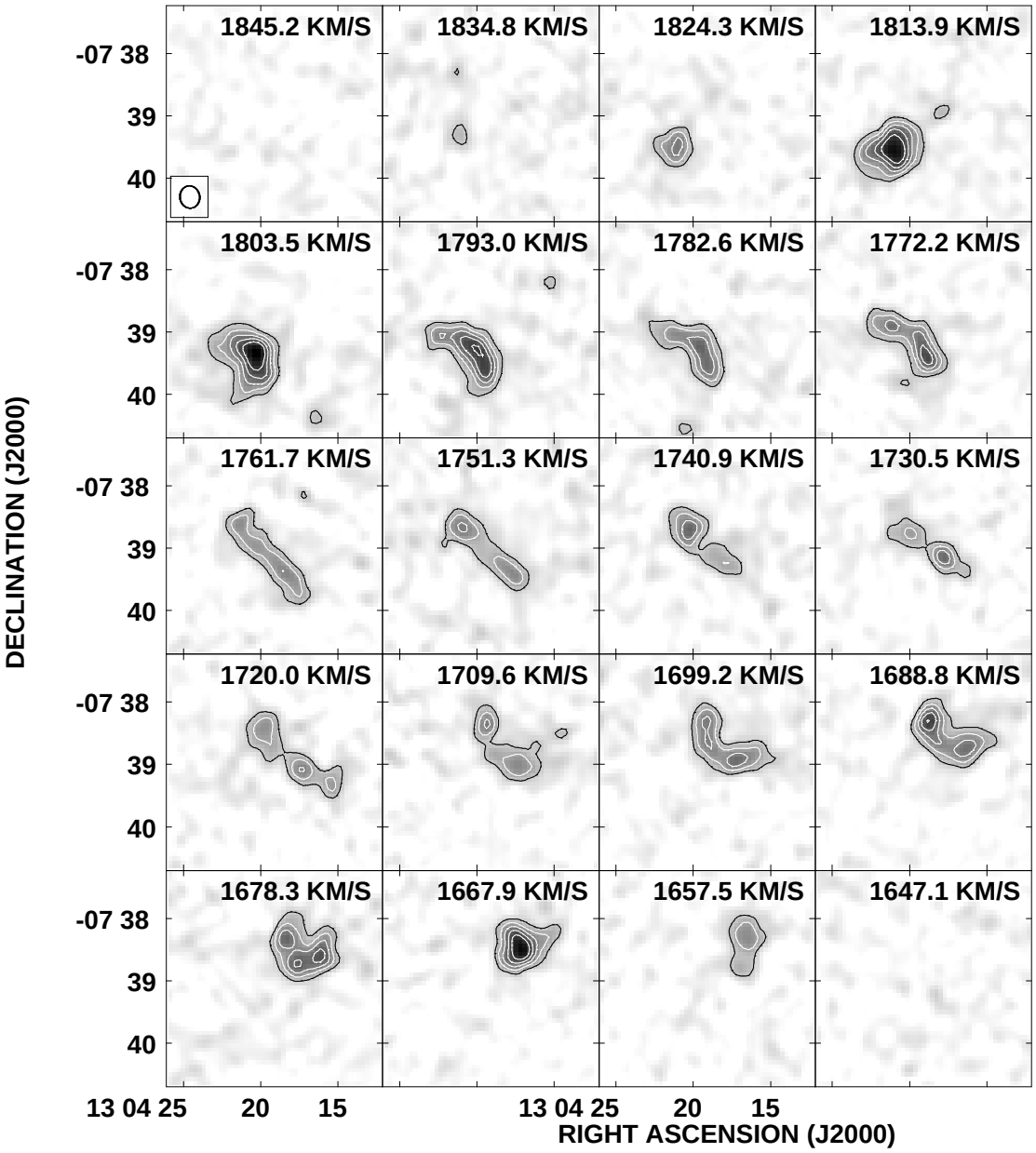

FIG. 17.— As in Figure 1, but for NGC 4942. The grayscale spans -0.02 to 16.02 mJy beam^{-1}. Every second channel is shown and the channel width is 5.2 km s^{-1}.

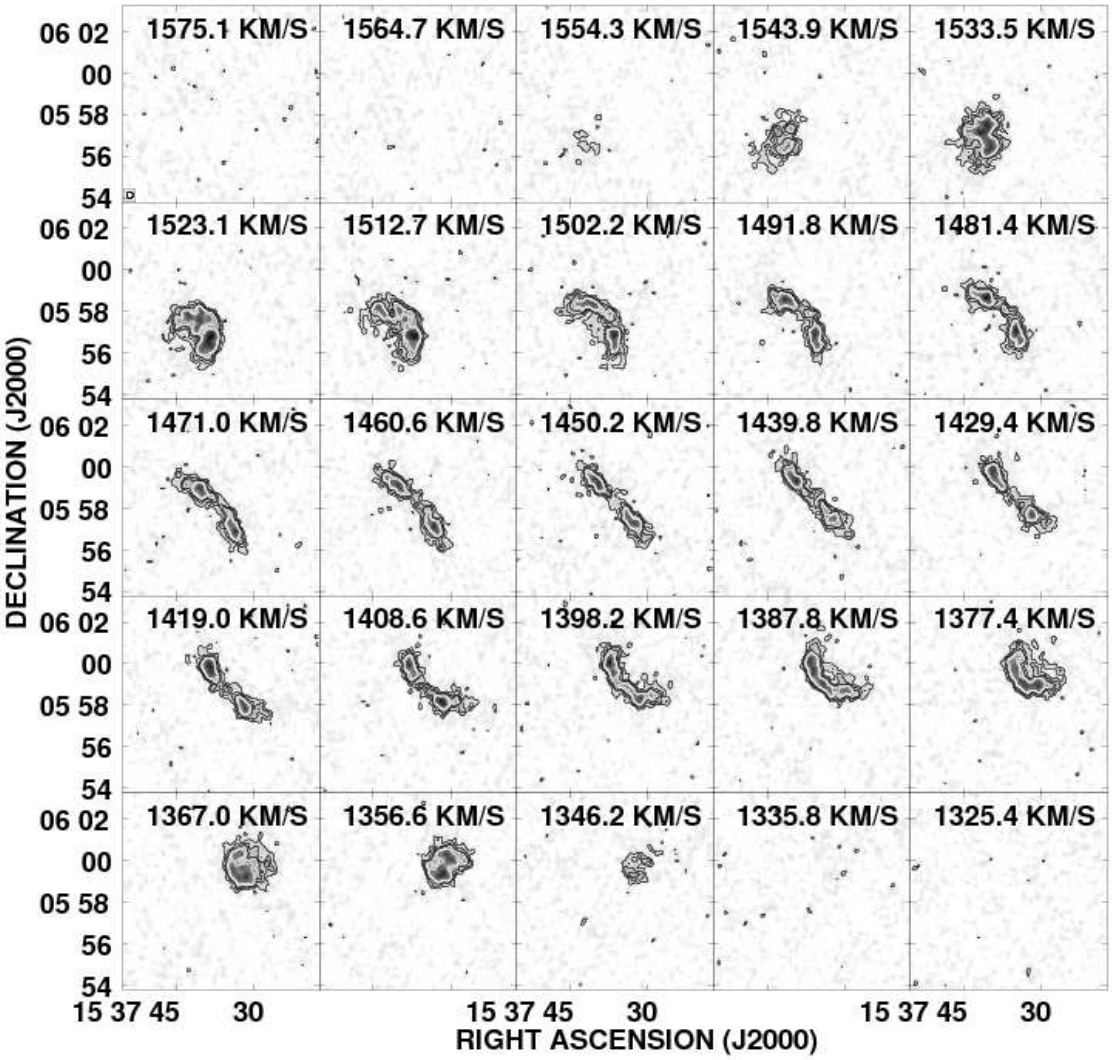

FIG. 18.— As in Figure 1, but for NGC 5964. The grayscale spans -0.02 to 16.25 mJy beam^{-1}. Every second channel is shown and the channel width is 5.2 km s^{-1}.

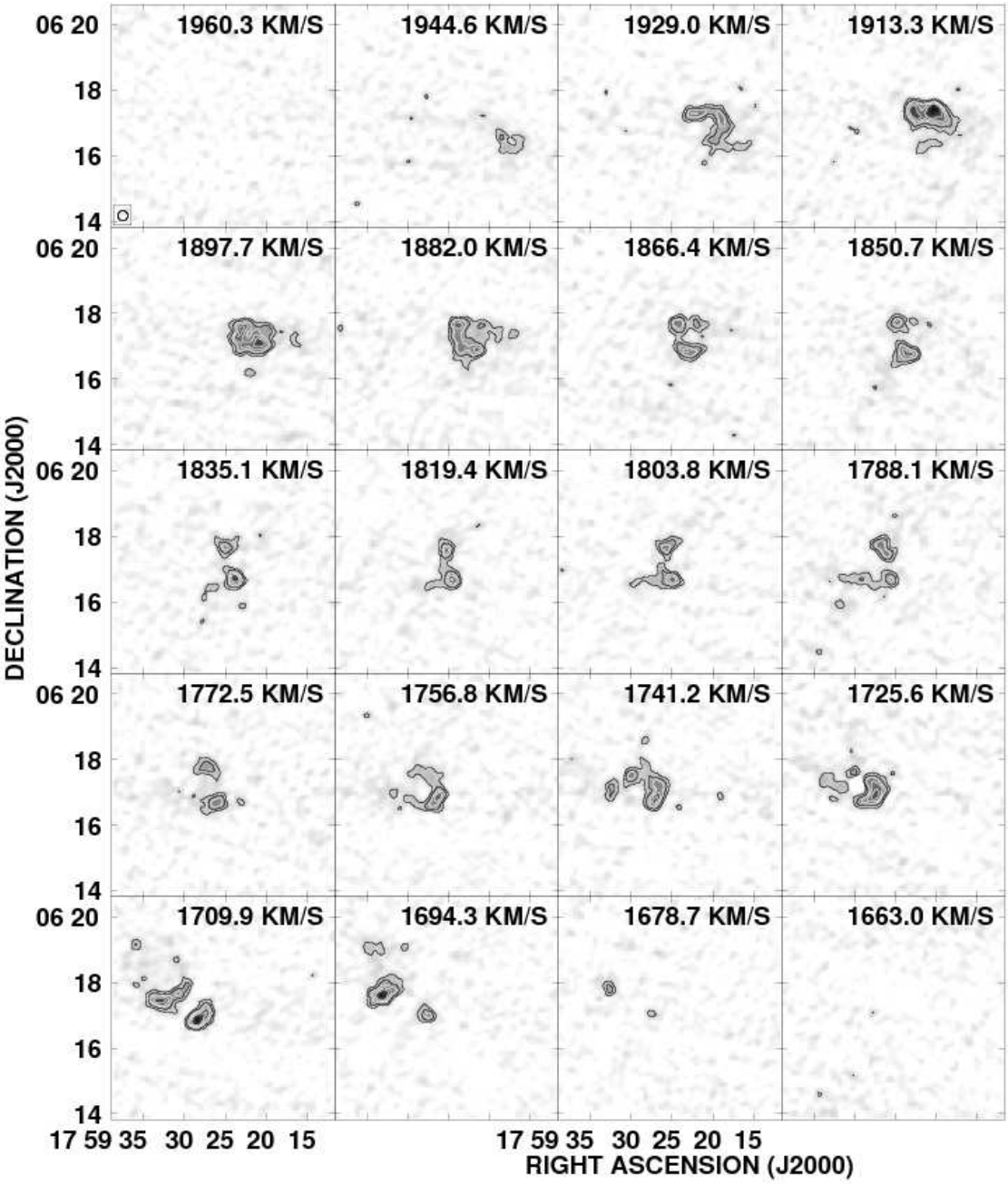

FIG. 19.— As in Figure 1, but for NGC 6509. The grayscale spans -0.02 to 17.43 mJy beam^{-1}. Every third channel is shown and the channel width is 5.2 km s^{-1}. The "hole" visible especially in the 1725.6 km s^{-1} channel is due to H I absorption of background continuum emission from a radio lobe of 4C 06.63. See Section 5 for details.

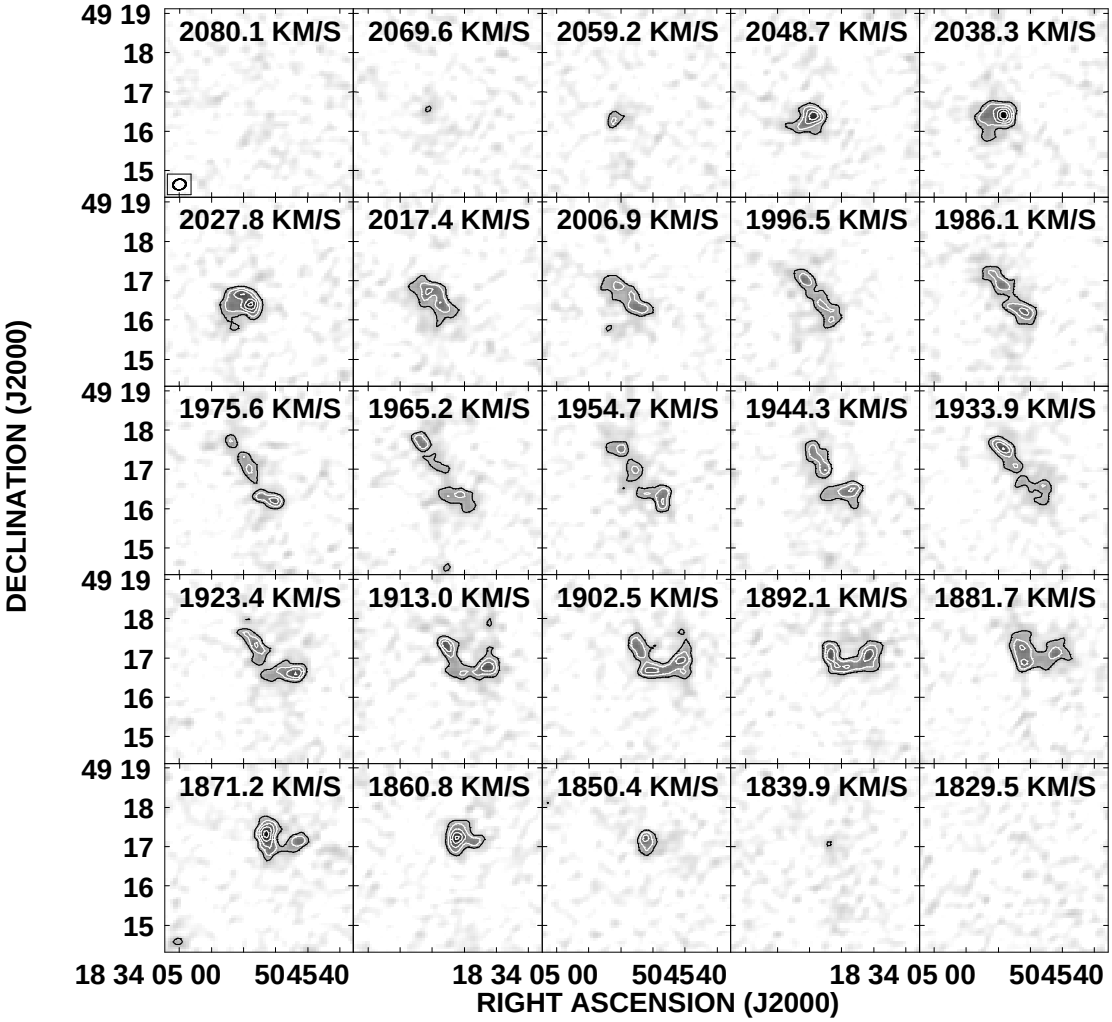

FIG. 20.— As in Figure 1, but for IC 1291. The grayscale spans -0.02 to 14.40 mJy beam^{-1}. Every second channel is shown and the channel width is 5.2 km s^{-1}.

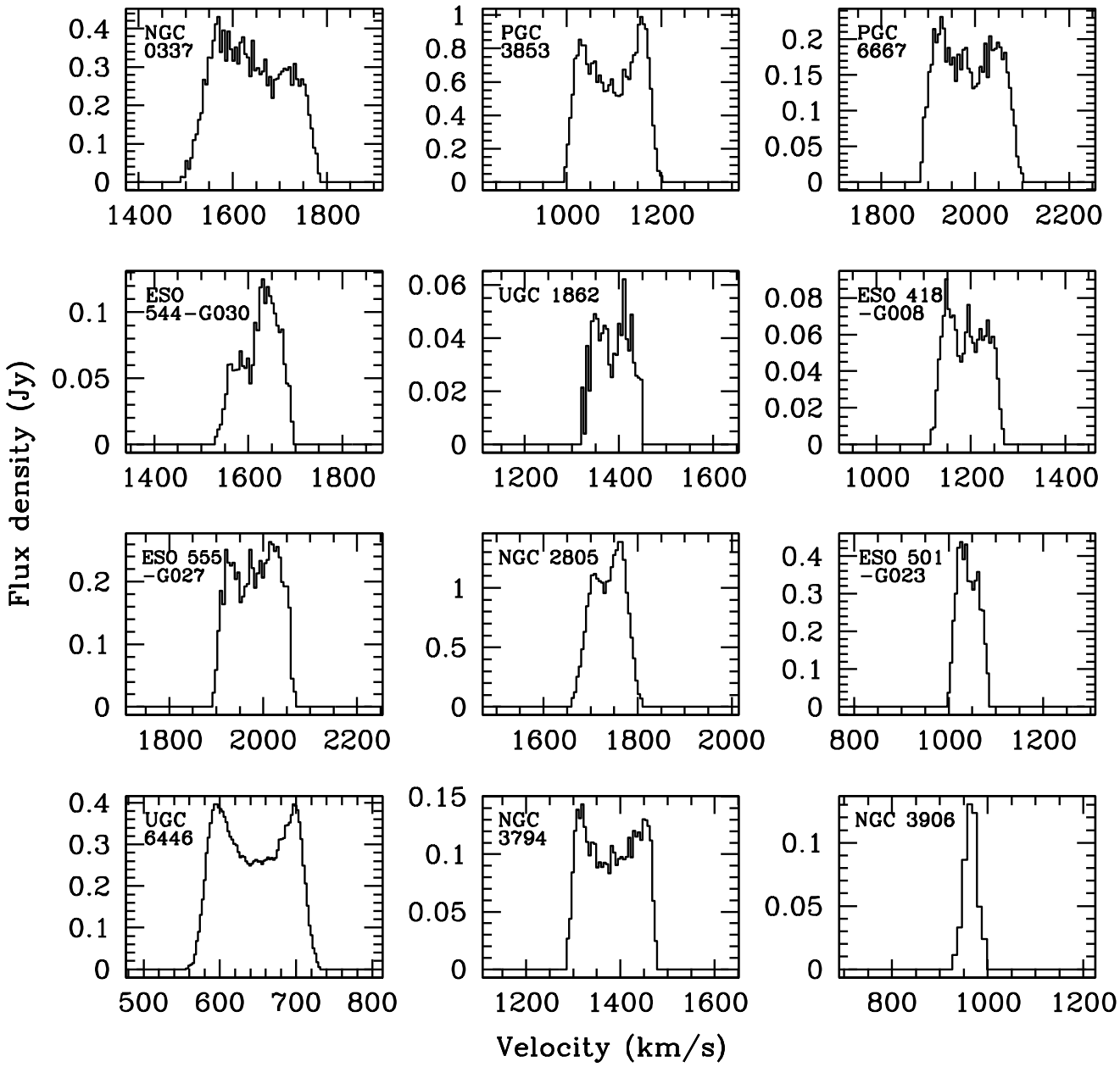

FIG. 21.— Integrated H I line profiles, created by summing the emission in each channel of the naturally-weighted data cubes. The channels outside the line emission show no noise pattern because of our blanking procedure.

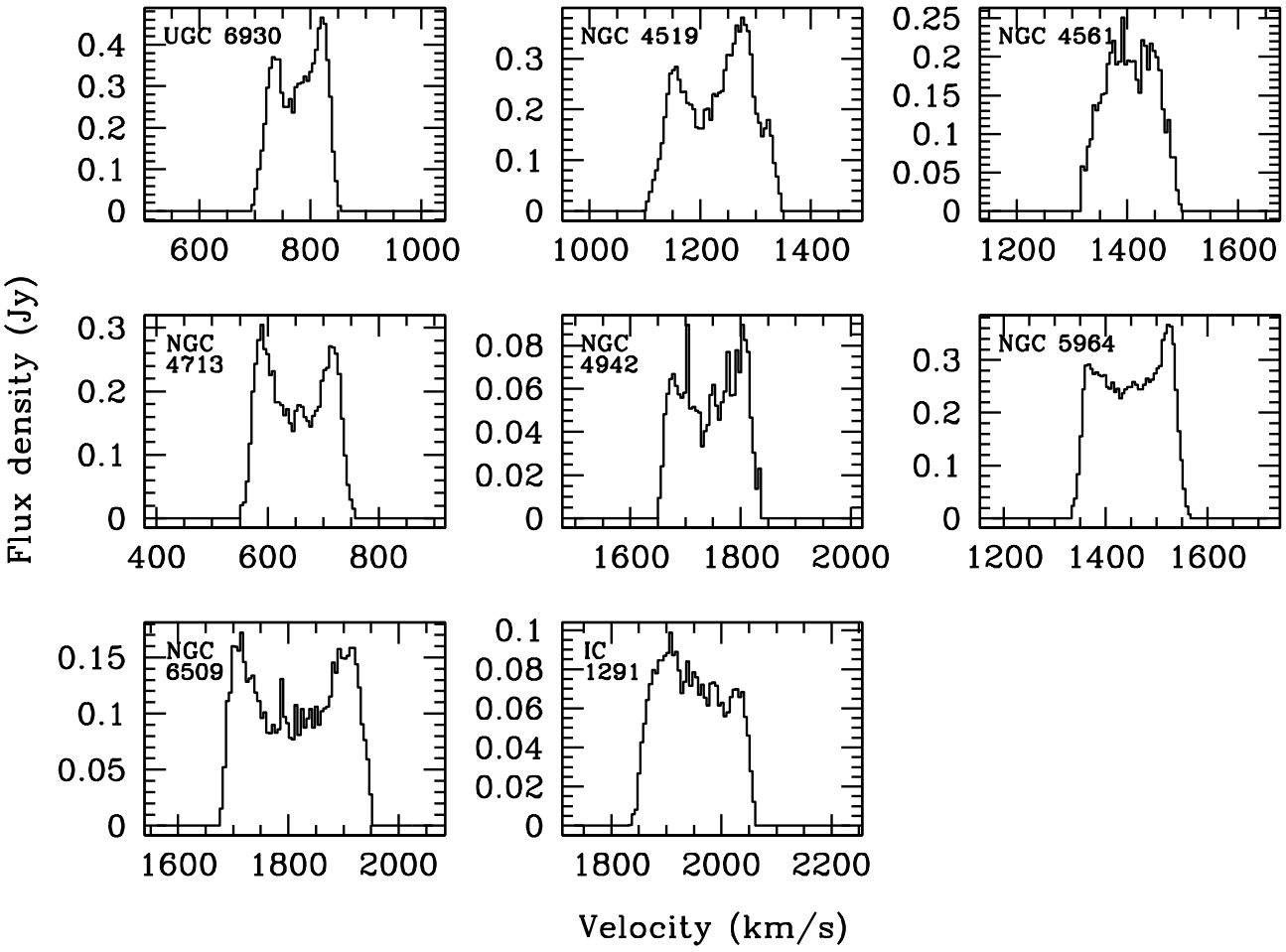

FIG. 21.— (Continued)

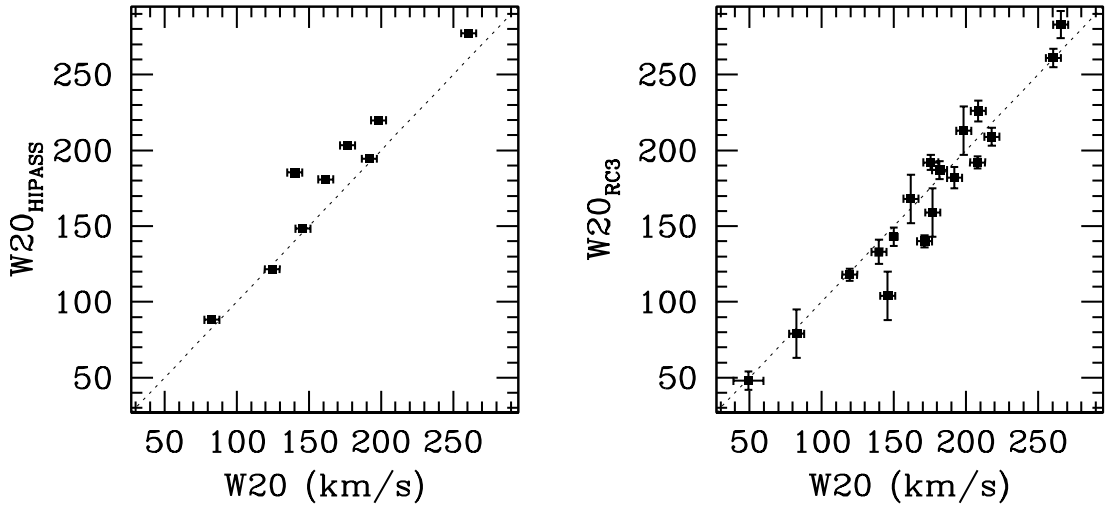

FIG. 22.— Comparison of our W_{20} values to single-dish values from HIPASS (*left*) and RC3 (*right*). The dashed line shows equality.

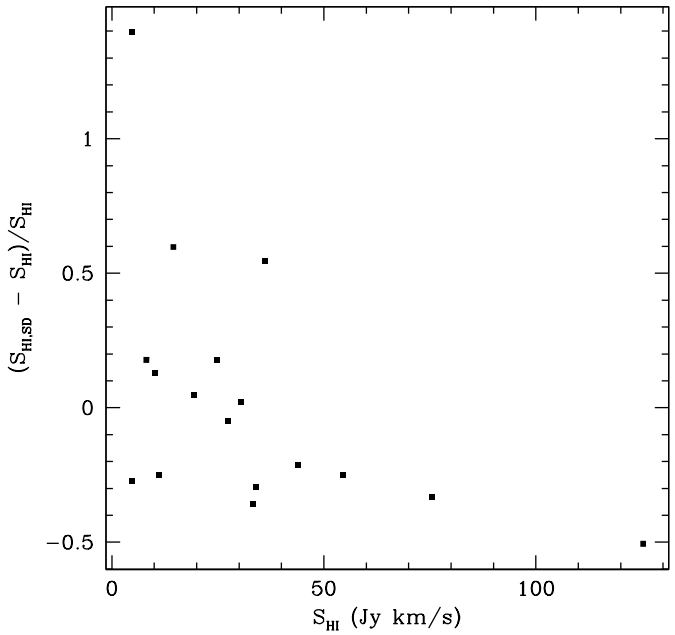

FIG. 23.— Comparison of our total H I fluxes ($S_{\rm HI}$) to single-dish measurements ($S_{\rm HI,\,SD}$) from Meyer et al. (2004) or Springob et al. (2005). We use the Meyer et al. (2004) value if both are available.

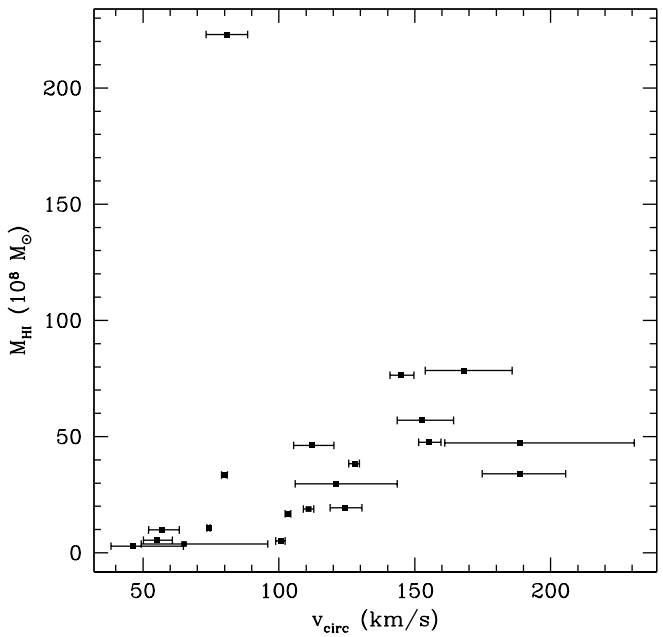

FIG. 24.— H I mass as a function of circular velocity, derived from rotation curve fitting in Section 4.3. The outlier is NGC 2805, for which the distance may be overestimated.

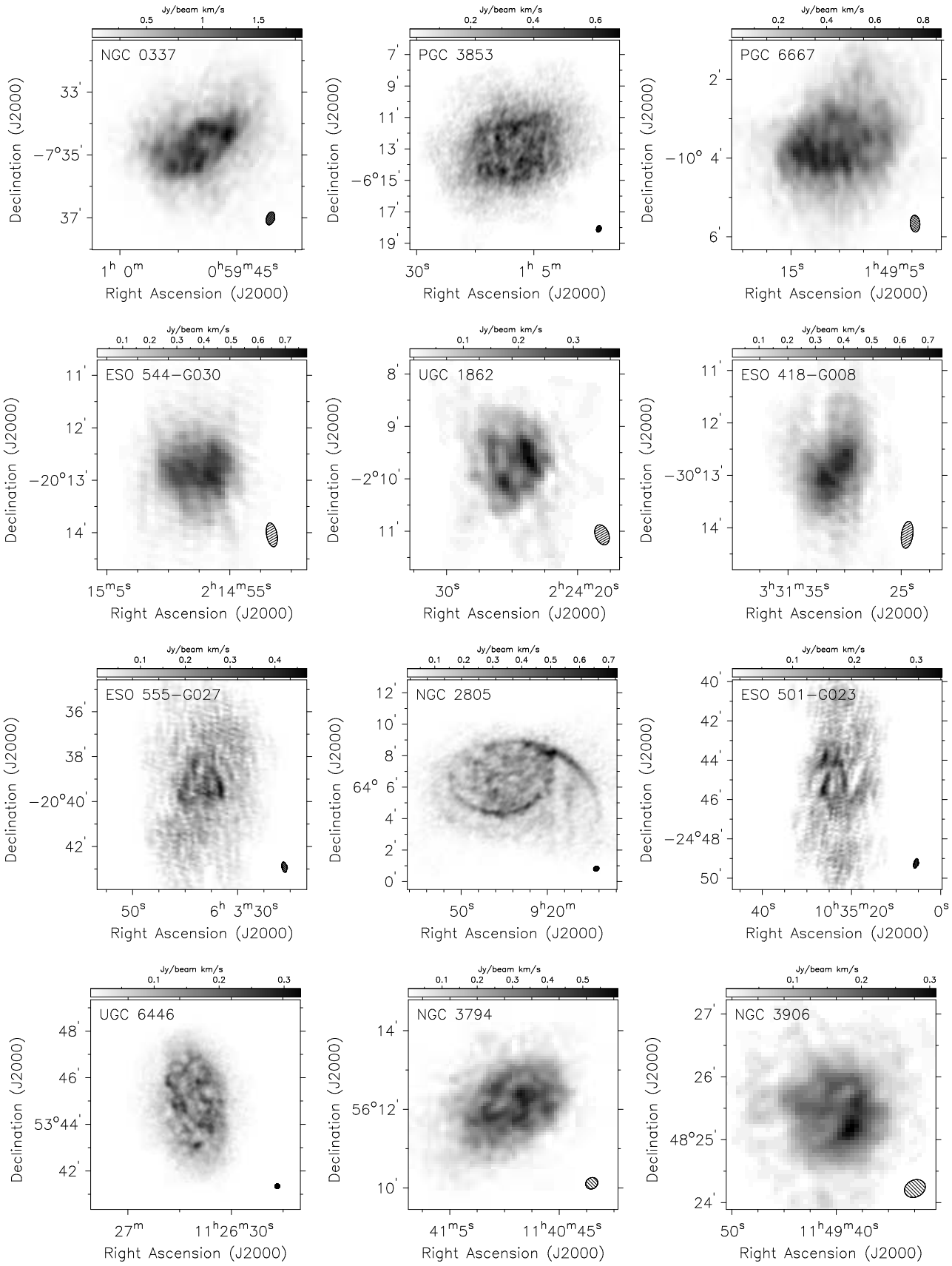

FIG. 25.— Integrated H I intensity map for each galaxy, derived from the naturally-weighted, blanked, and primary beam corrected data cube. The maps cover the same area shown in the channel maps. The beam size is shown in the lower right corner of each panel.

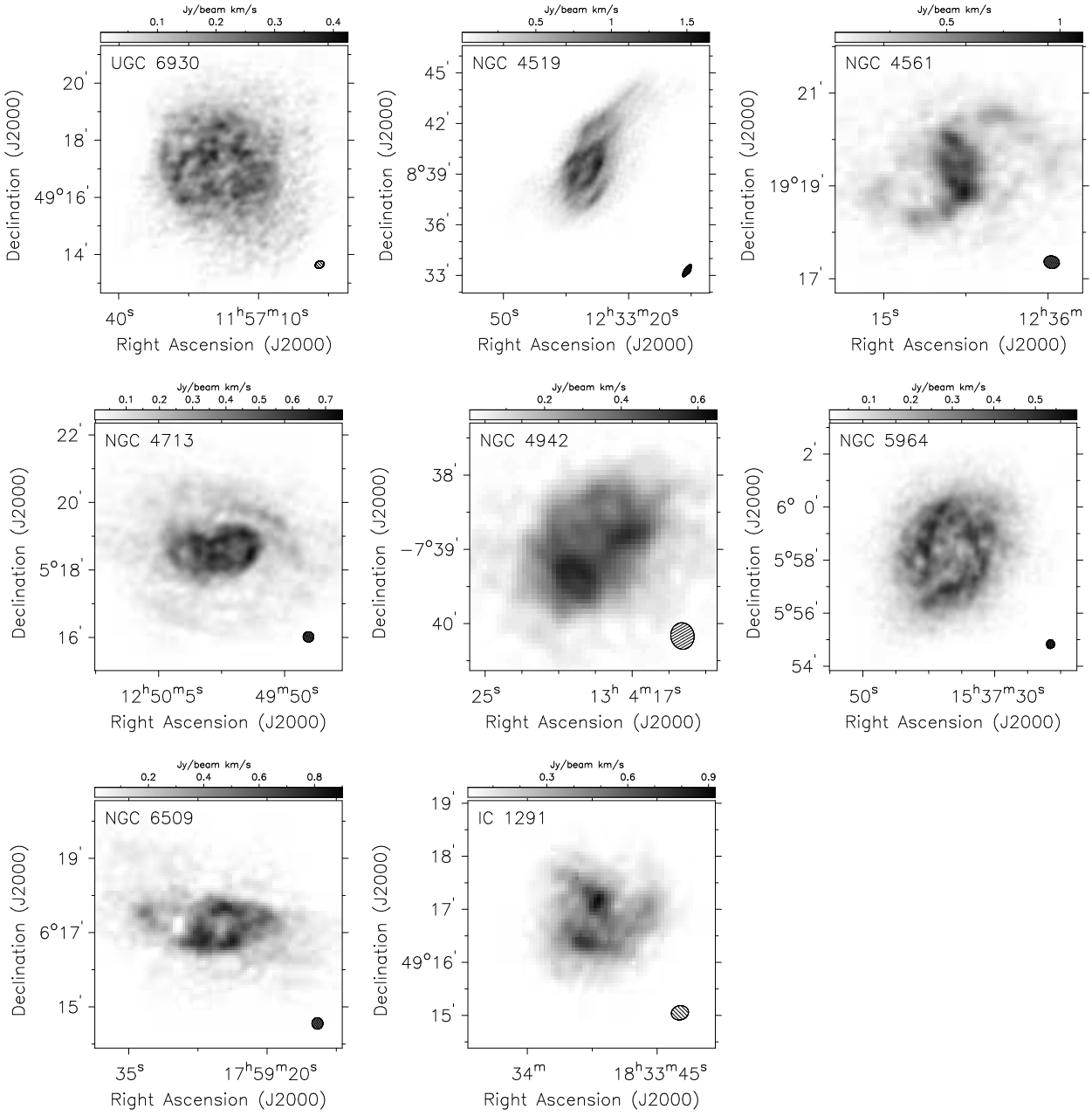

FIG. 25.— (Continued) Note the "hole" in NGC 6509. H I is in absorption here because it is in the foreground of a strong radio lobe. See Section 5 for more details.

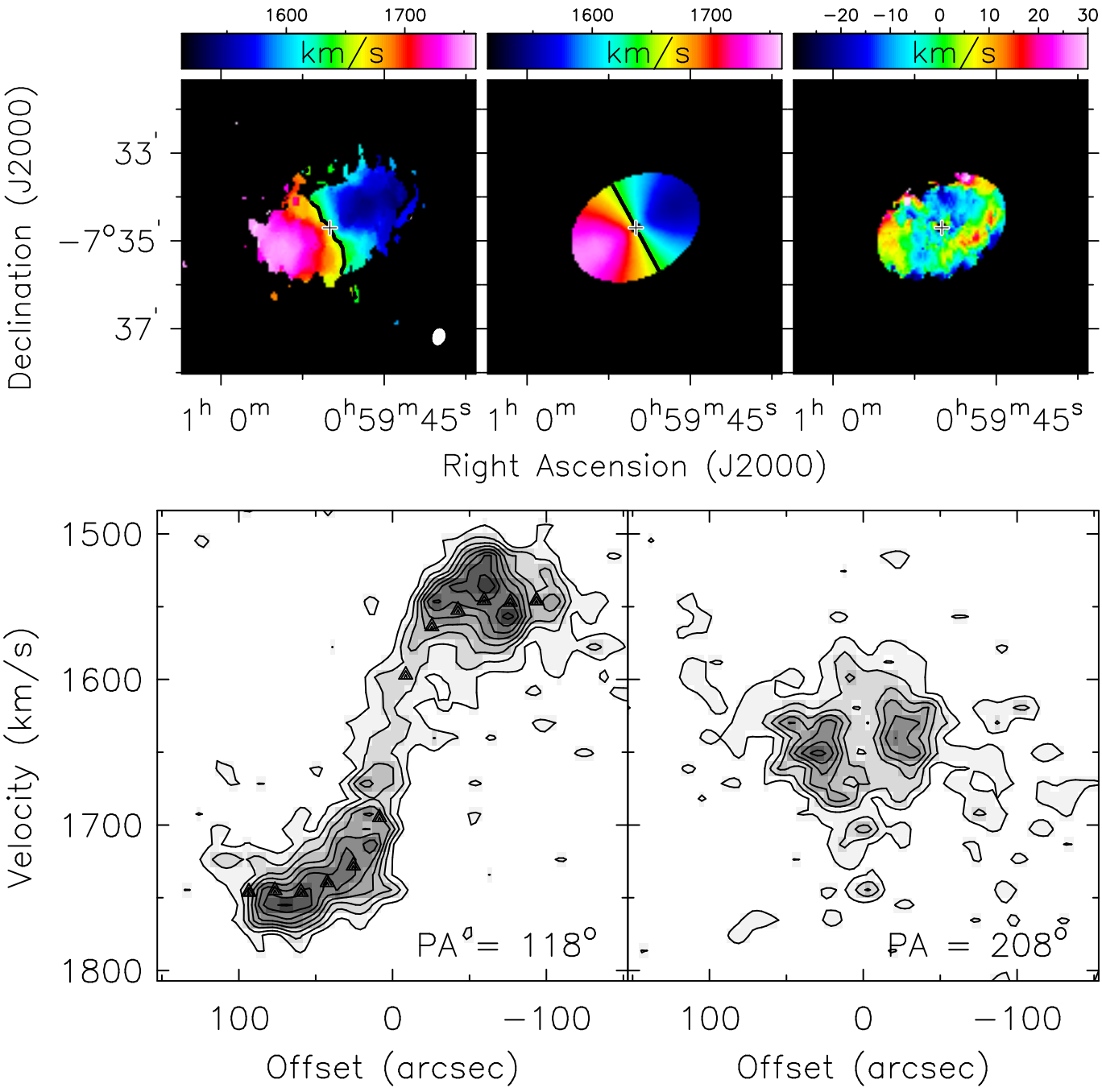

FIG. 26.— Velocity field and position-velocity diagrams for NGC 0337. *Top row*: the *left panel* shows the first-moment map, created using the method described in Section 4.3 and covering the same area as the channel maps. The beam size is shown in the lower right corner. The *middle panel* shows the tilted ring model velocity field. The *right panel* shows the residual velocity map (the first-moment map minus the velocity field model) in the region of overlap between the data and model. The final dynamical center is shown as a cross in all three panels and the *thick black contour* shows the final systemic velocity in the left and middle panels. *Bottom row*: position velocity diagrams along the major axis (*left panel*) and minor axis (*right panel*). Contours begin at 2σ and end at the maximum surface brightness along the major axis slice plus 2σ, in steps of 2σ, where σ is the image noise from Column 6 of Table 3 (2 mJy beam^{-1} to 20 mJy beam^{-1} in steps of 2 mJy beam^{-1} in this case). The projected tilted ring model fit is overplotted as *solid triangles* in the left panel.

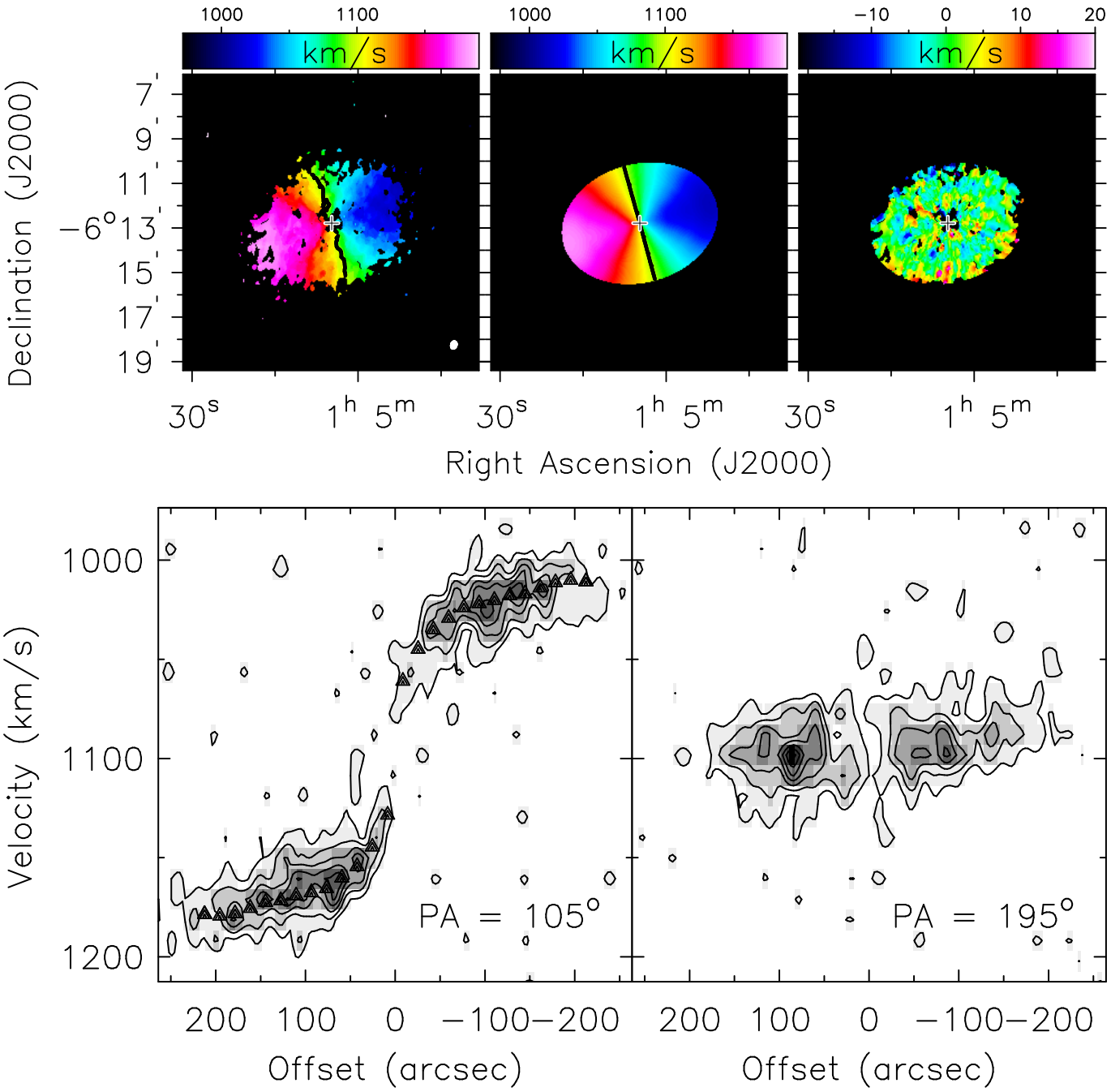

FIG. 27.— As in Figure 26, but for PGC 3853. The position-velocity diagram contours are from 2 mJy beam^{-1} to 14 mJy beam^{-1} in steps of 2 mJy beam^{-1}.

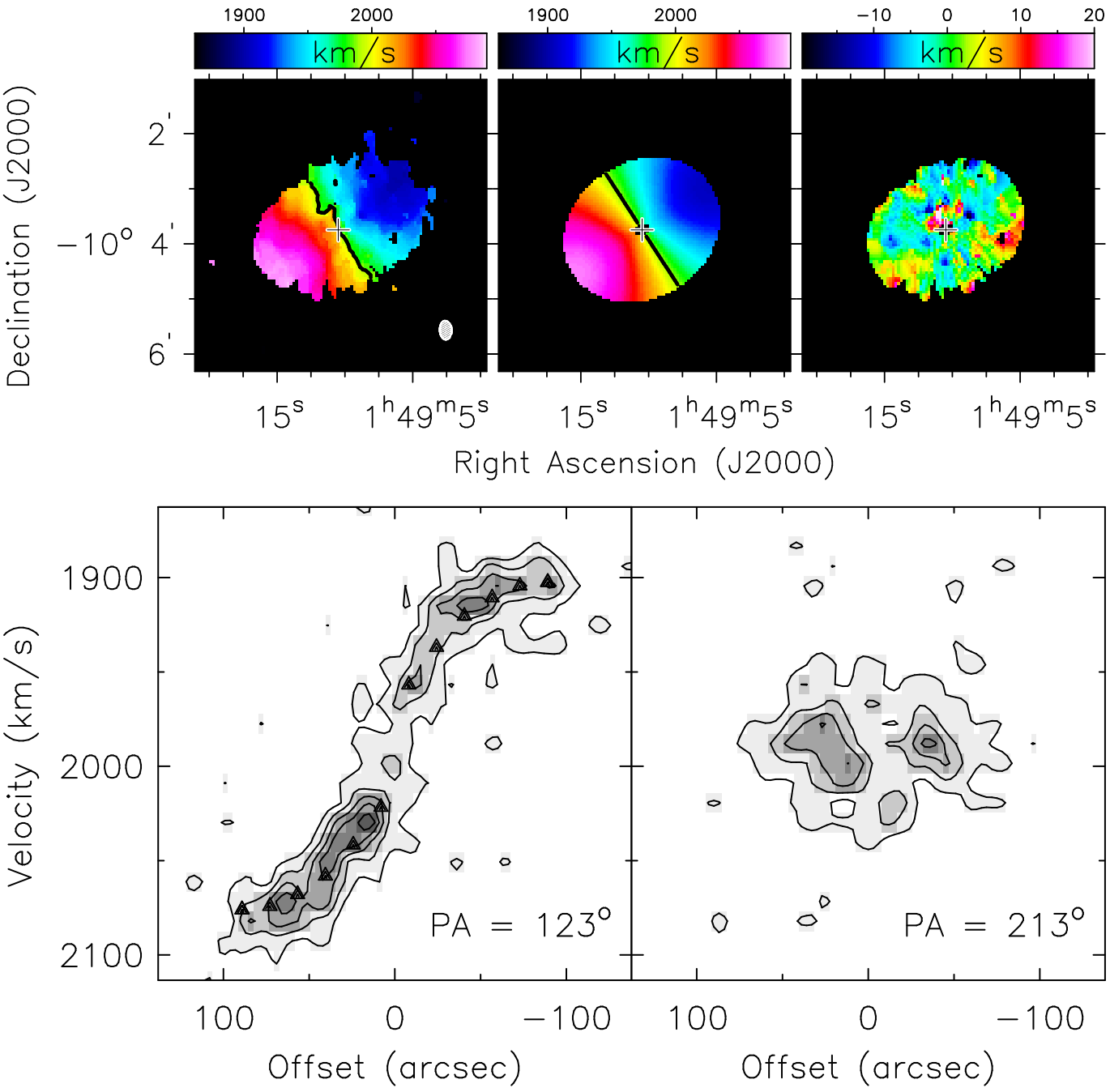

FIG. 28.— As in Figure 26, but for PGC 6667. The position-velocity diagram contours are from 2 mJy beam^{-1} to 14 mJy beam^{-1} in steps of 2 mJy beam^{-1}.

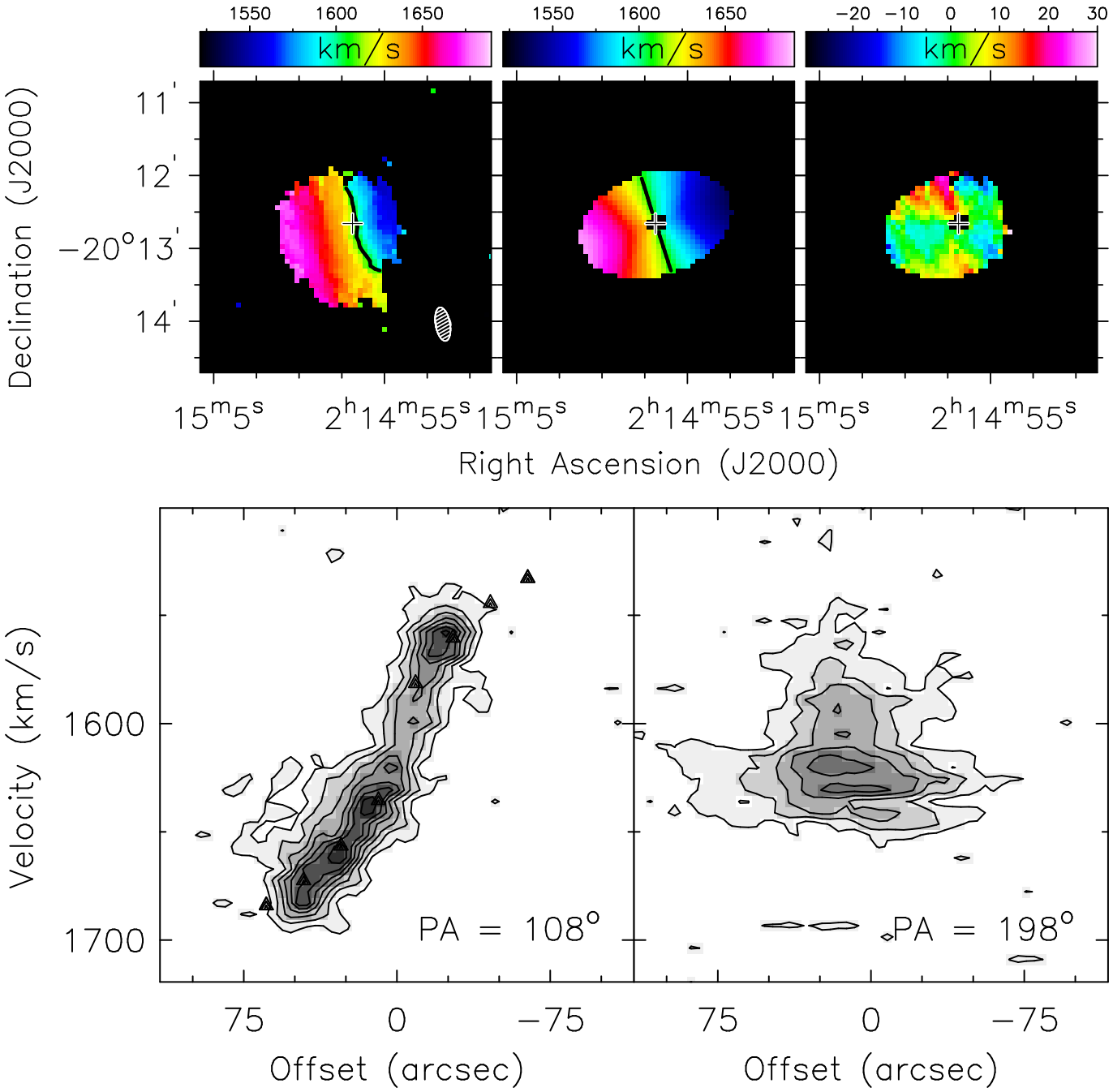

FIG. 29.— As in Figure 26, but for ESO 544-G030. The position-velocity diagram contours are from 2 mJy beam^{-1} to 18 mJy beam^{-1} in steps of 2 mJy beam^{-1}.

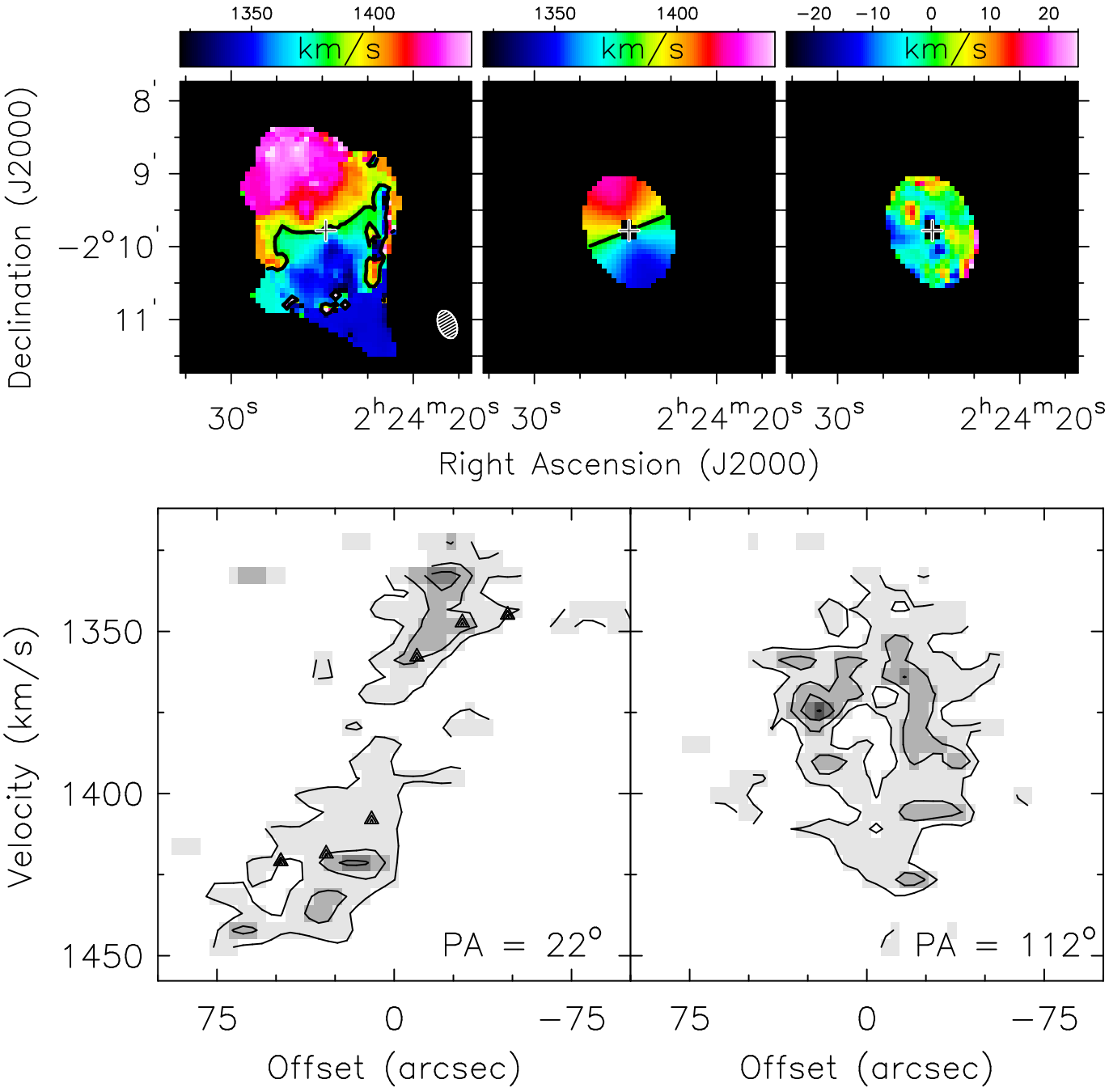

FIG. 30.— As in Figure 26, but for UGC 1862. The position-velocity diagram contours are from 2 mJy beam^{-1} to 10 mJy beam^{-1} in steps of 2 mJy beam^{-1}.

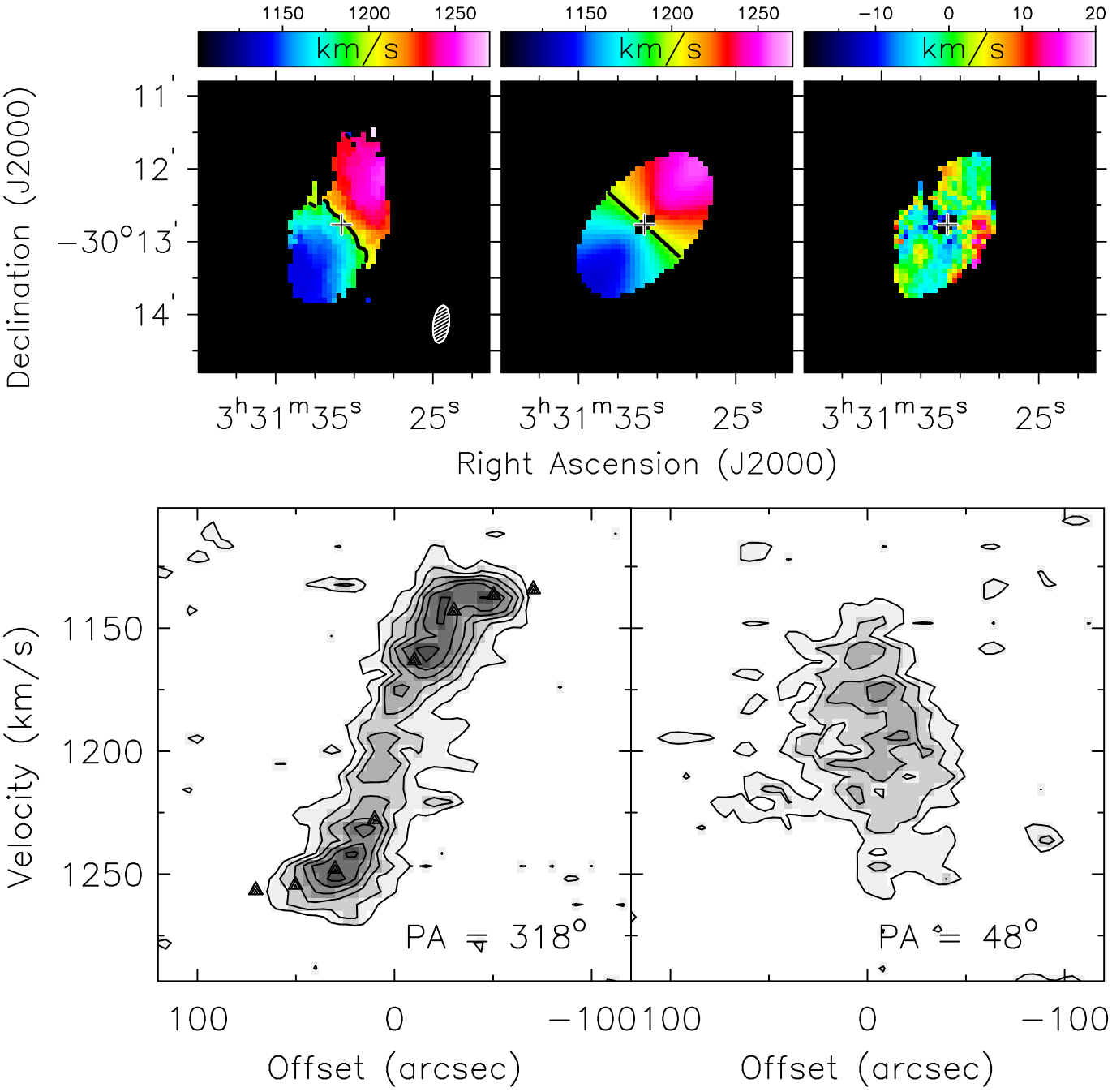

FIG. 31.— As in Figure 26, but for ESO 418-G008. The position-velocity diagram contours are from 2 mJy beam^{-1} to 16 mJy beam^{-1} in steps of 2 mJy beam^{-1}.

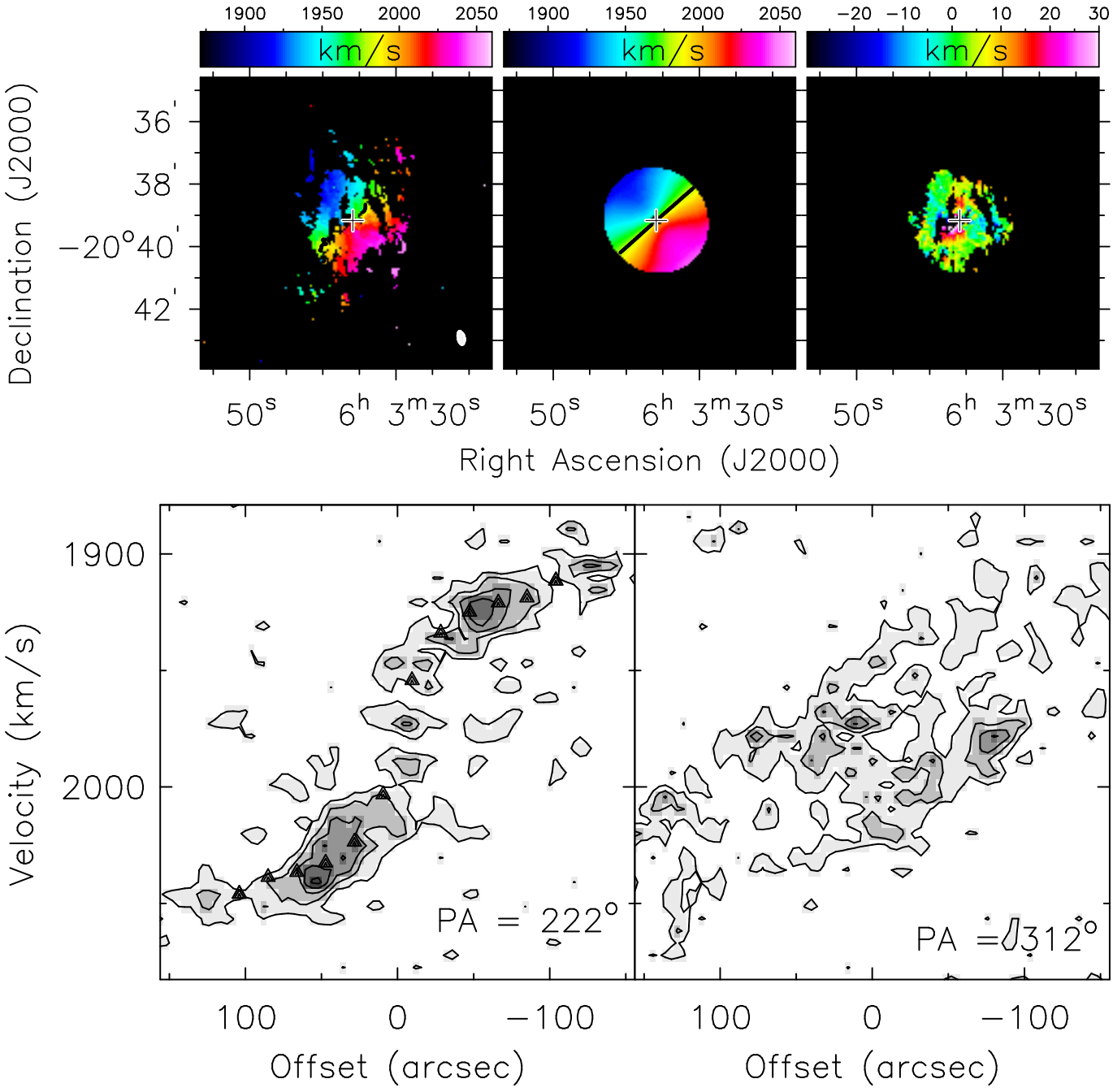

FIG. 32.— As in Figure 26, but for ESO 555-G027. The position-velocity diagram contours are from 2 mJy beam^{-1} to 13 mJy beam^{-1} in steps of 2 mJy beam^{-1}.

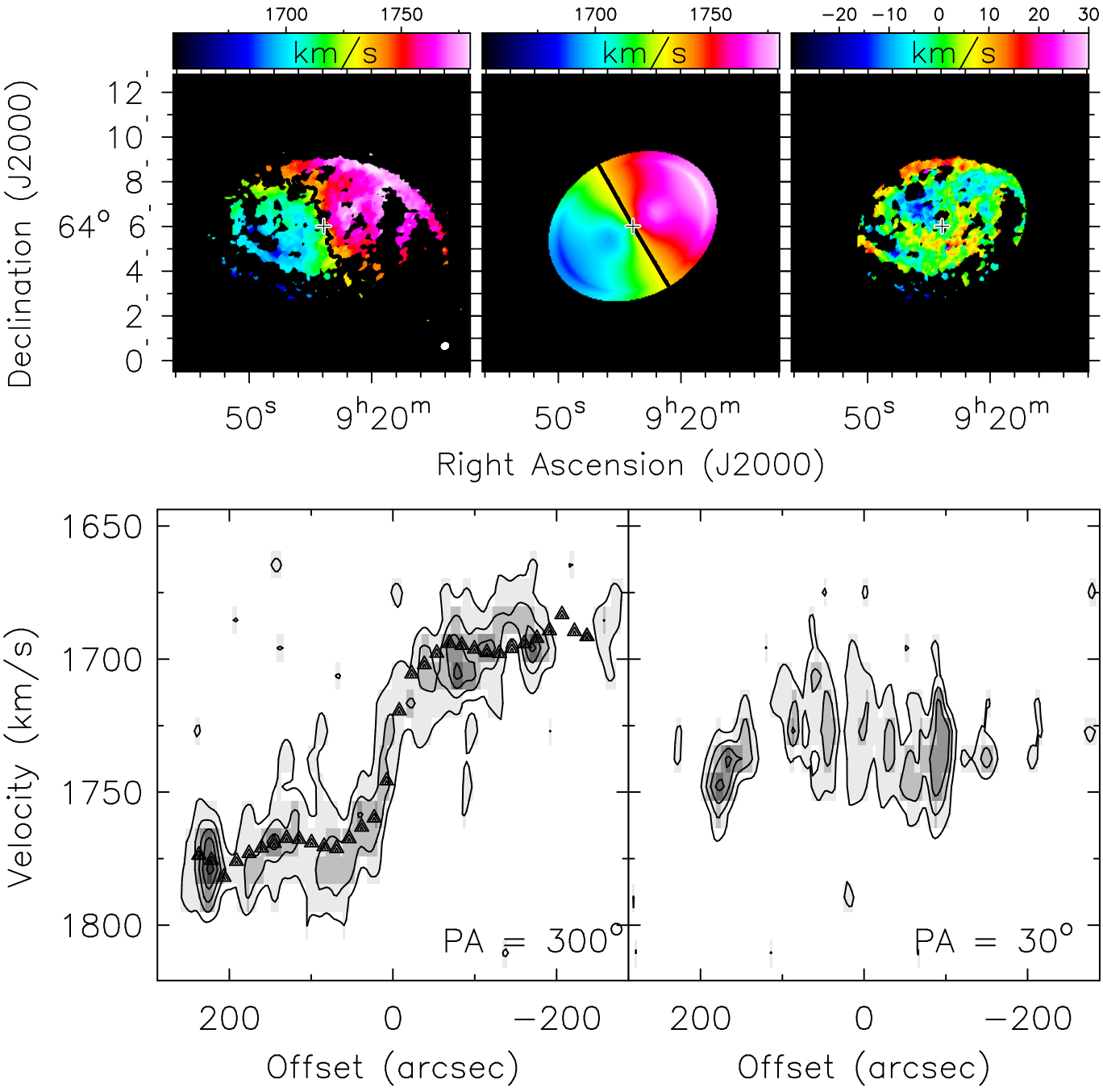

FIG. 33.— As in Figure 26, but for NGC 2805. The position-velocity diagram contours are from 2 mJy beam^{-1} to 13 mJy beam^{-1} in steps of 2 mJy beam^{-1}.

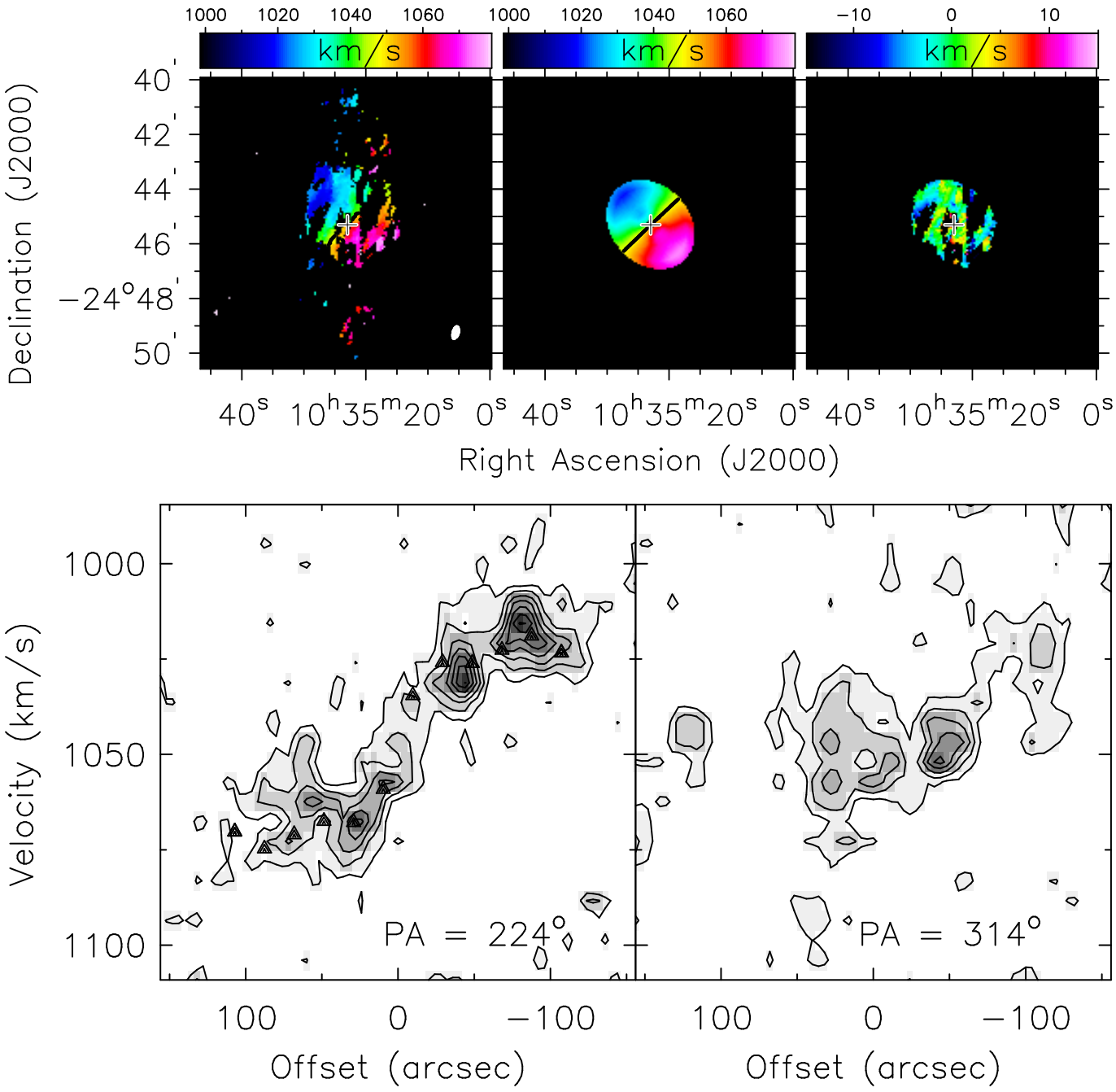

FIG. 34.— As in Figure 26, but for ESO 501-G023. The position-velocity diagram contours are from 2 mJy beam^{-1} to 16 mJy beam^{-1} in steps of 2 mJy beam^{-1}.

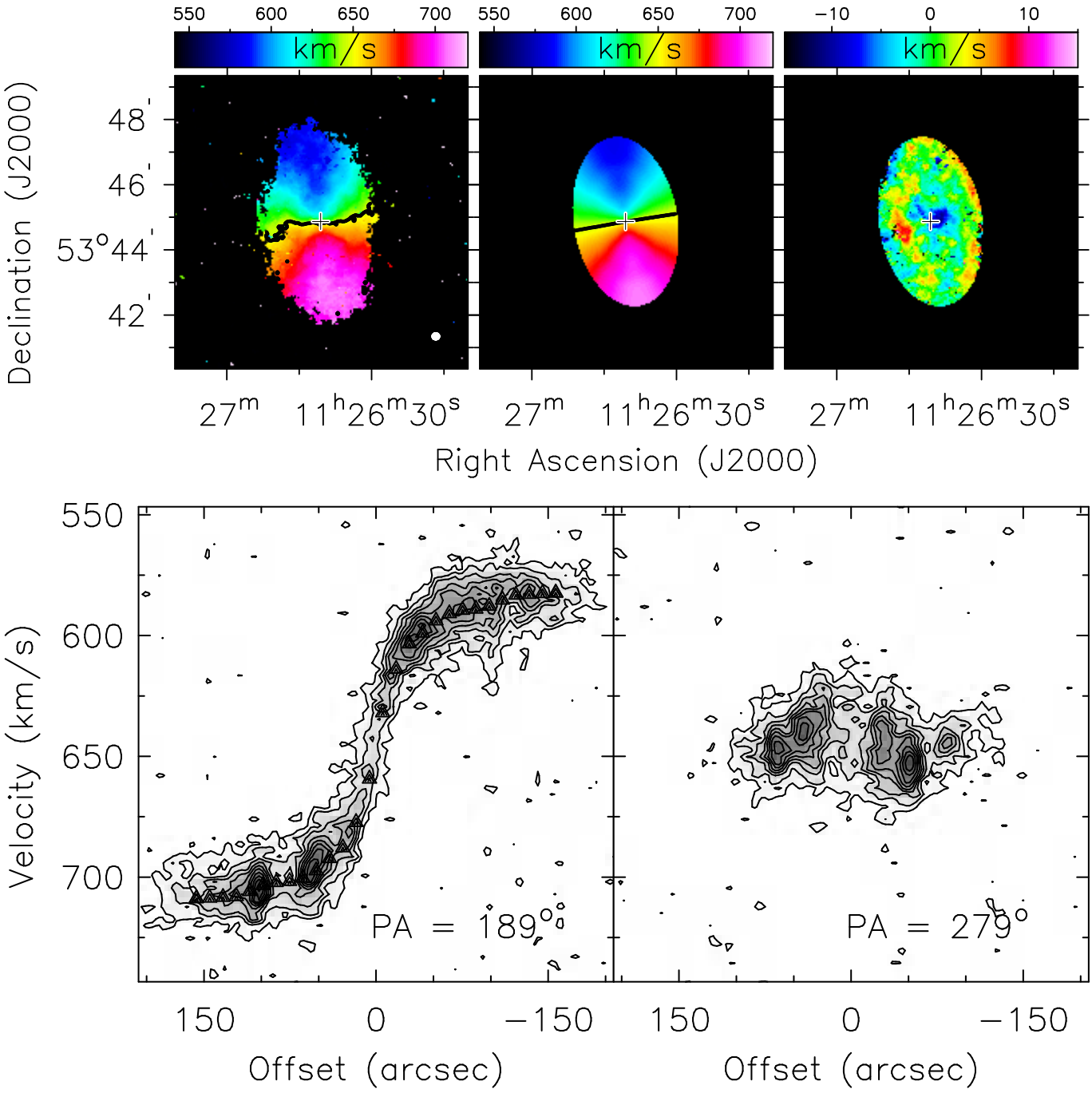

FIG. 35.— As in Figure 26, but for UGC 6446. The position-velocity diagram contours are from 1 mJy beam^{-1} to 12 mJy beam^{-1} in steps of 1 mJy beam^{-1}.

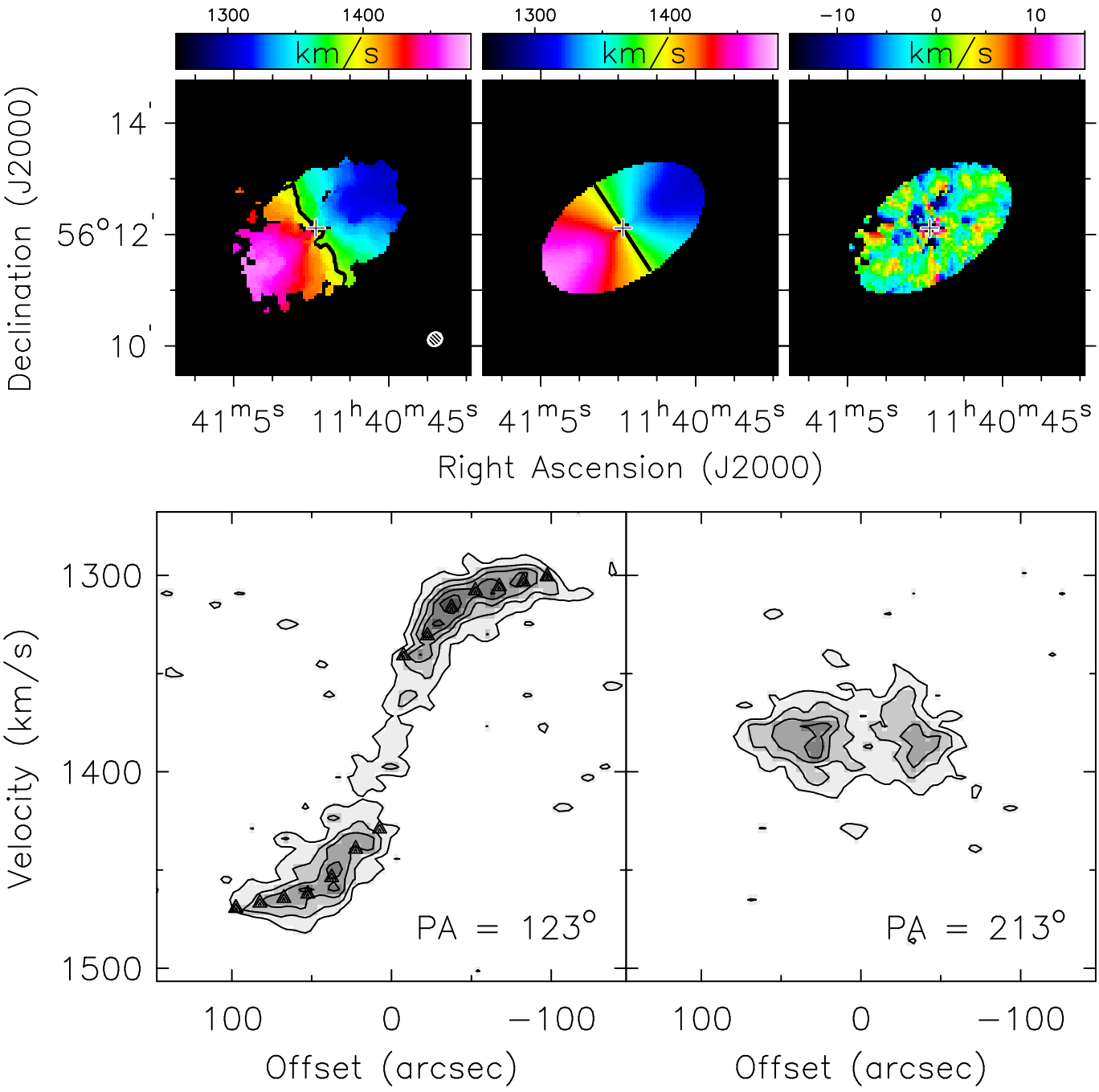

FIG. 36.— As in Figure 26, but for NGC 3794. The position-velocity diagram contours are from 2 mJy beam^{-1} to 14 mJy beam^{-1} in steps of 2 mJy beam^{-1}.

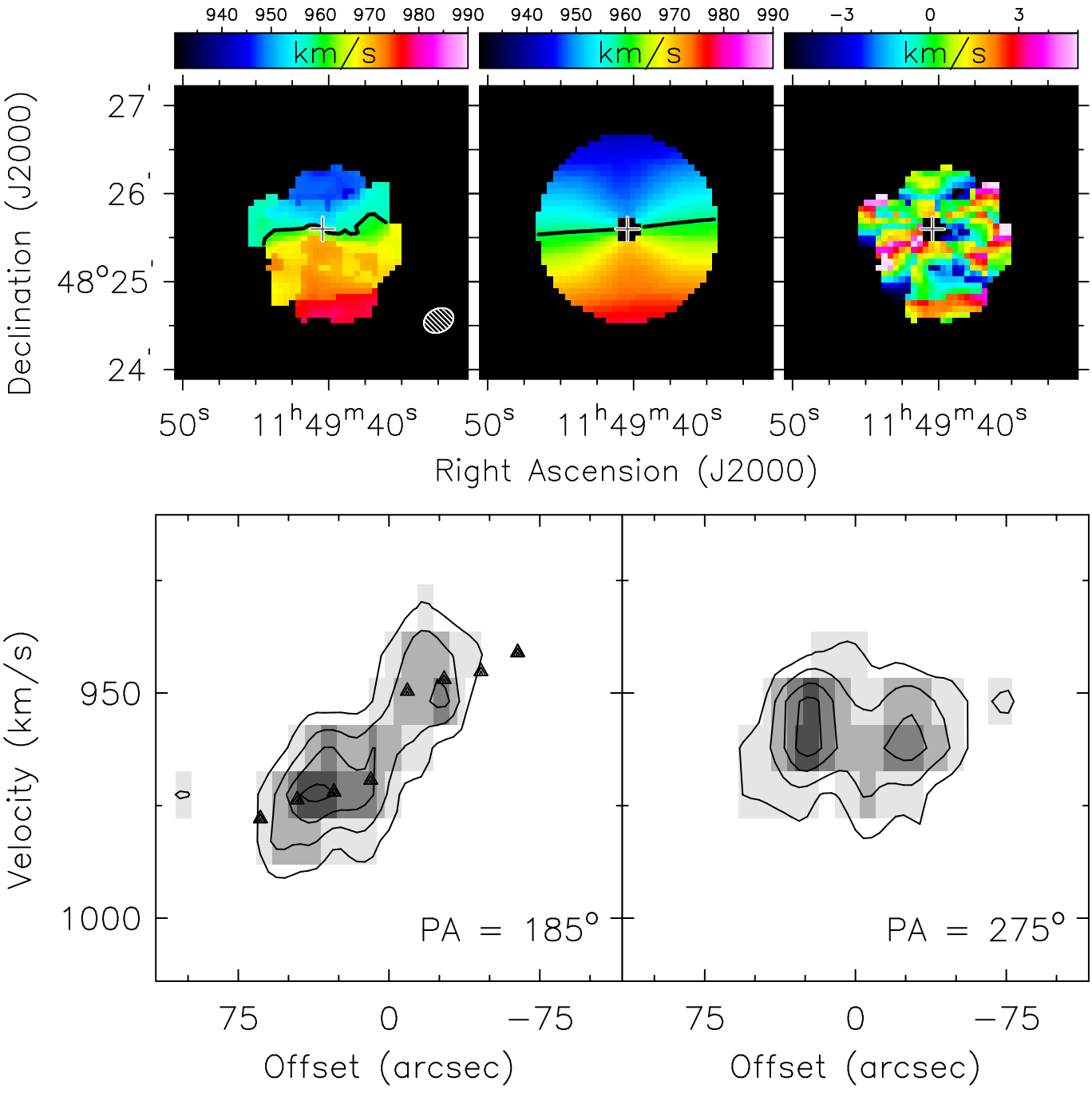

FIG. 37.— As in Figure 26, but for NGC 3906. The position-velocity diagram contours are from 2 mJy beam^{-1} to 11 mJy beam^{-1} in steps of 2 mJy beam^{-1}.

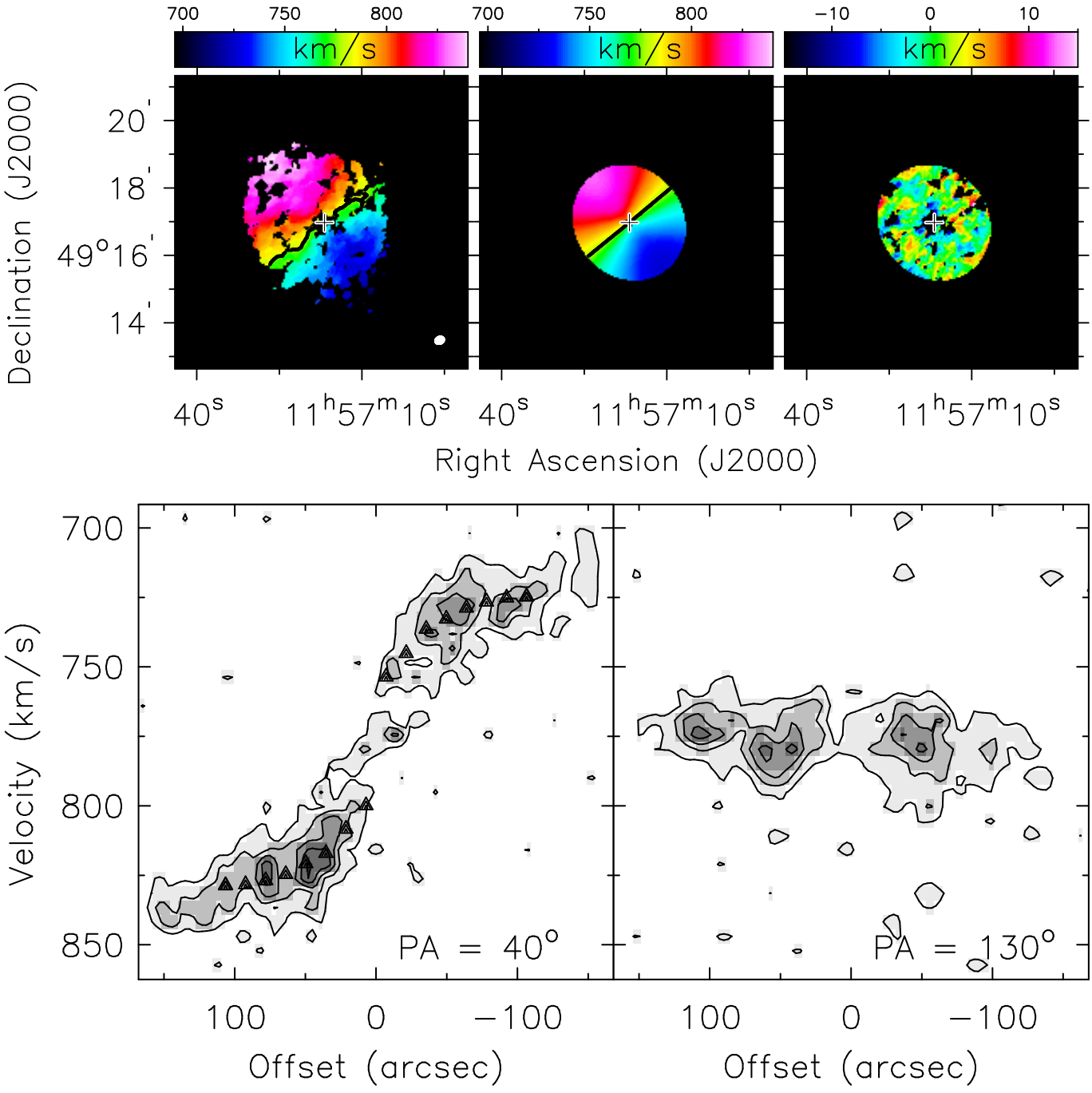

FIG. 38.— As in Figure 26, but for UGC 6930. The position-velocity diagram contours are from 2 mJy beam^{-1} to 12 mJy beam^{-1} in steps of 2 mJy beam^{-1}.

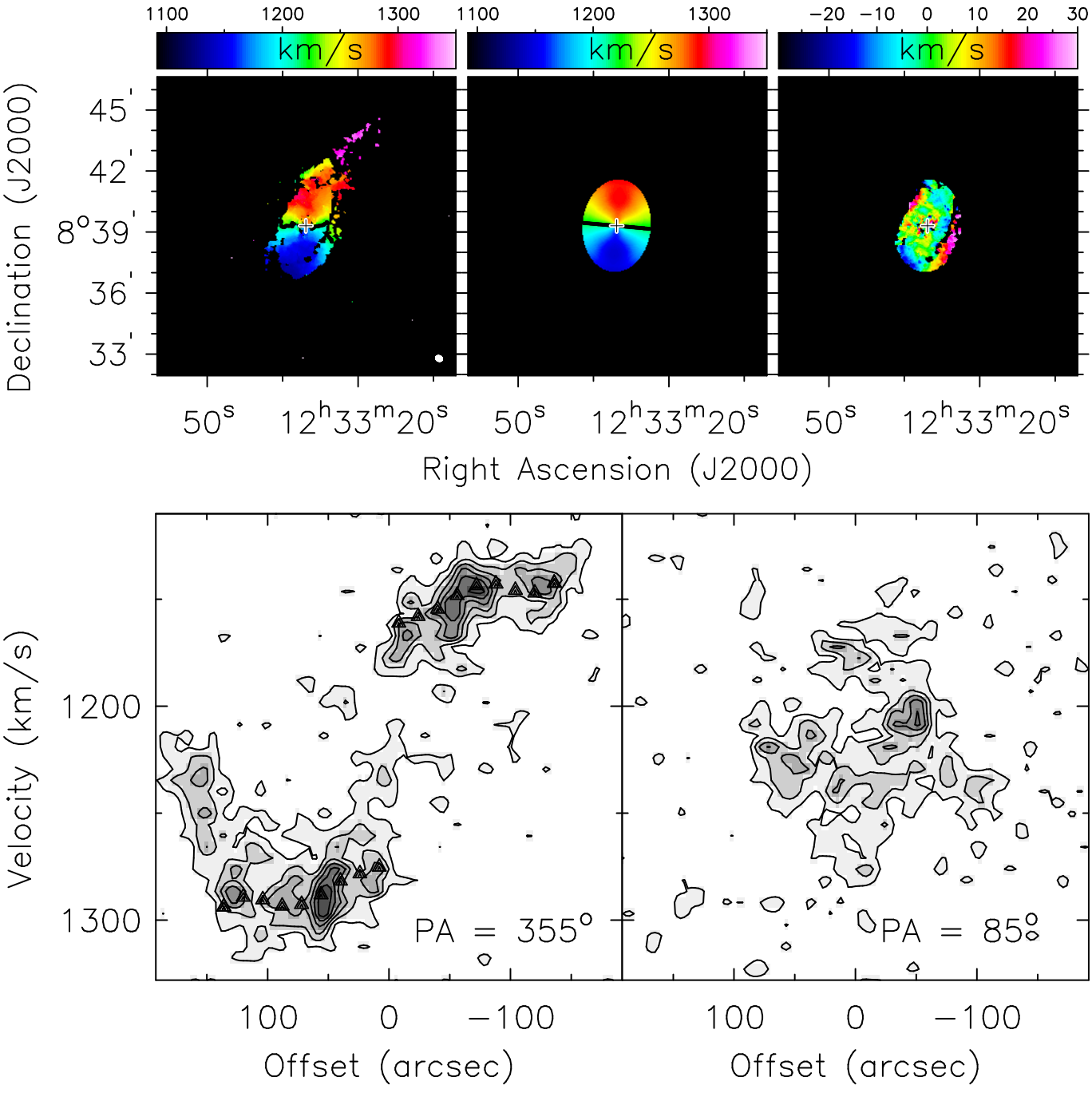

FIG. 39.— As in Figure 26, but for NGC 4519. The position-velocity diagram contours are from 2 mJy beam^{-1} to 16 mJy beam^{-1} in steps of 2 mJy beam^{-1}.

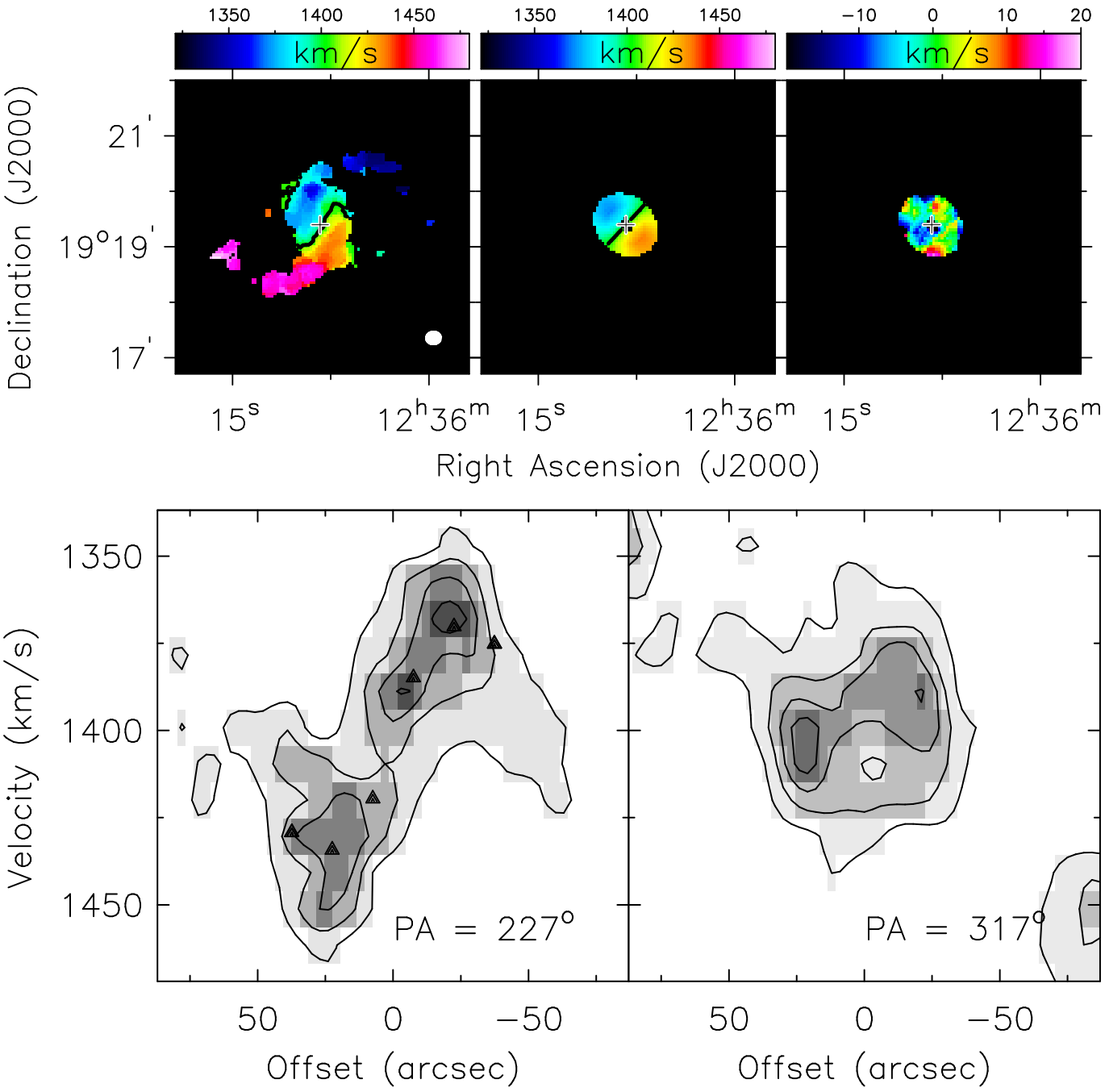

FIG. 40.— As in Figure 26, but for NGC 4561. The position-velocity diagram contours are from 3 mJy beam^{-1} to 17 mJy beam^{-1} in steps of 3 mJy beam^{-1}.

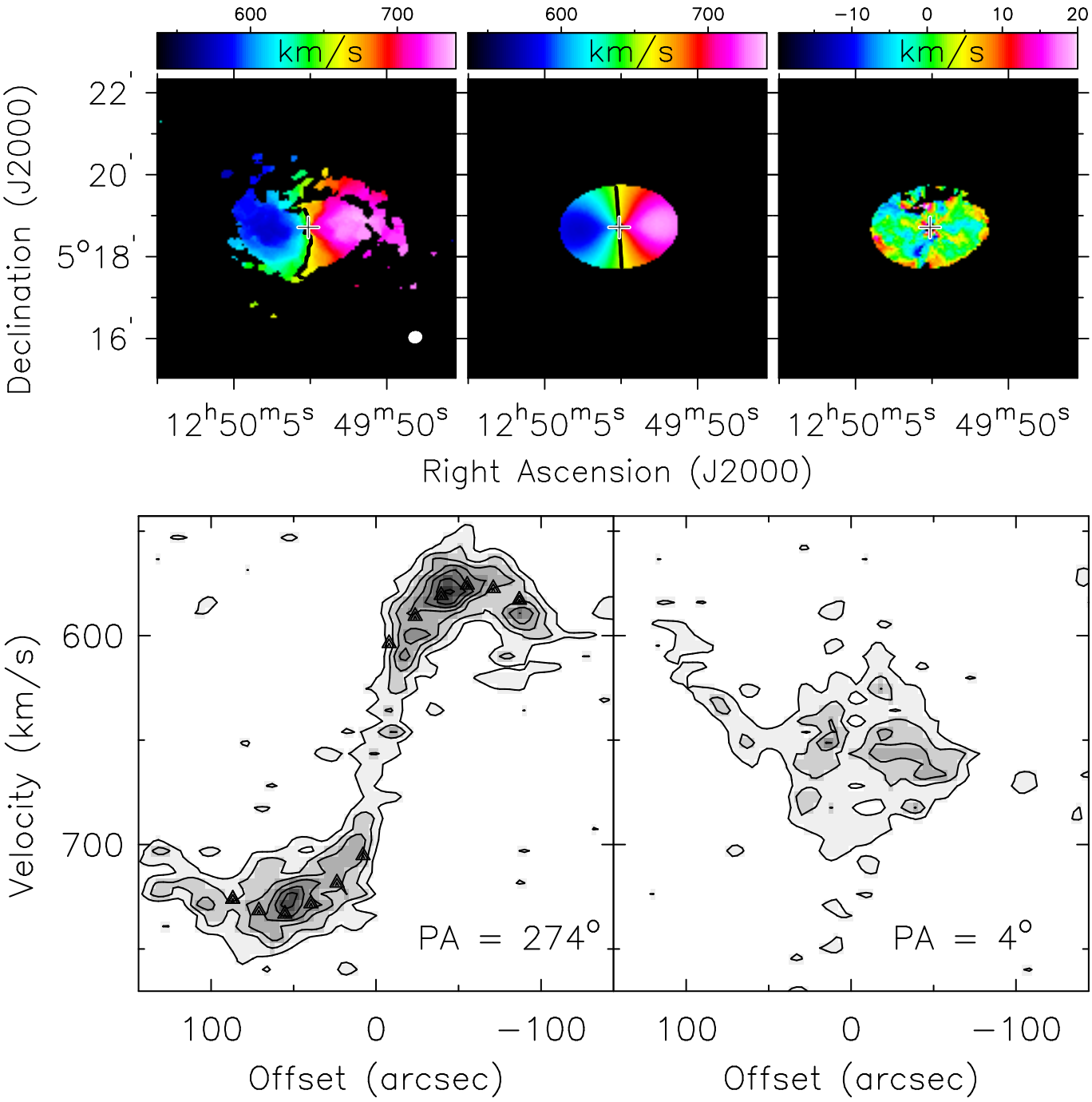

FIG. 41.— As in Figure 26, but for NGC 4713. The position-velocity diagram contours are from 2 mJy beam^{-1} to 16 mJy beam^{-1} in steps of 2 mJy beam^{-1}.

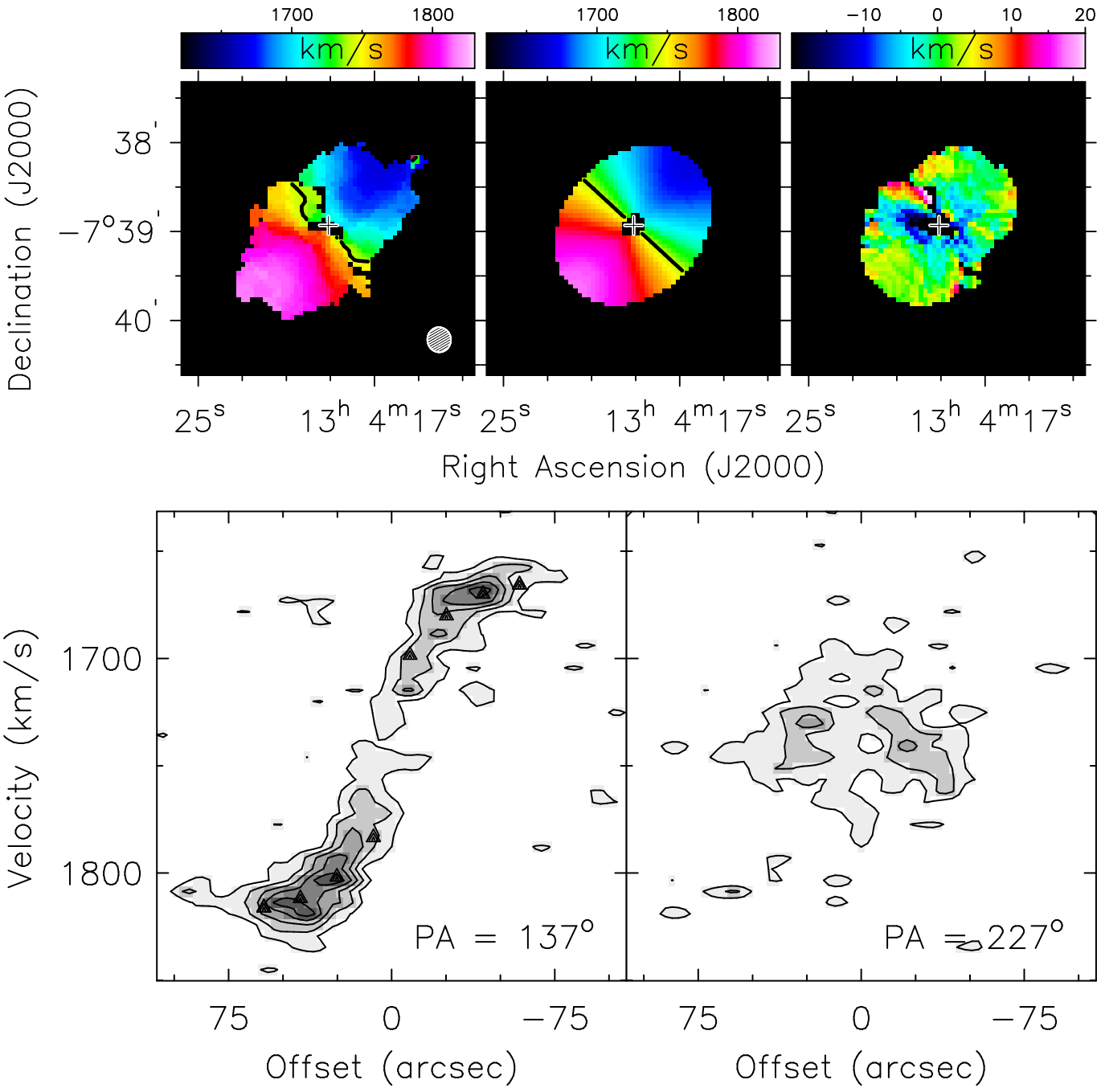

FIG. 42.— As in Figure 26, but for NGC 4942. The position-velocity diagram contours are from 2 mJy beam^{-1} to 14 mJy beam^{-1} in steps of 2 mJy beam^{-1}.

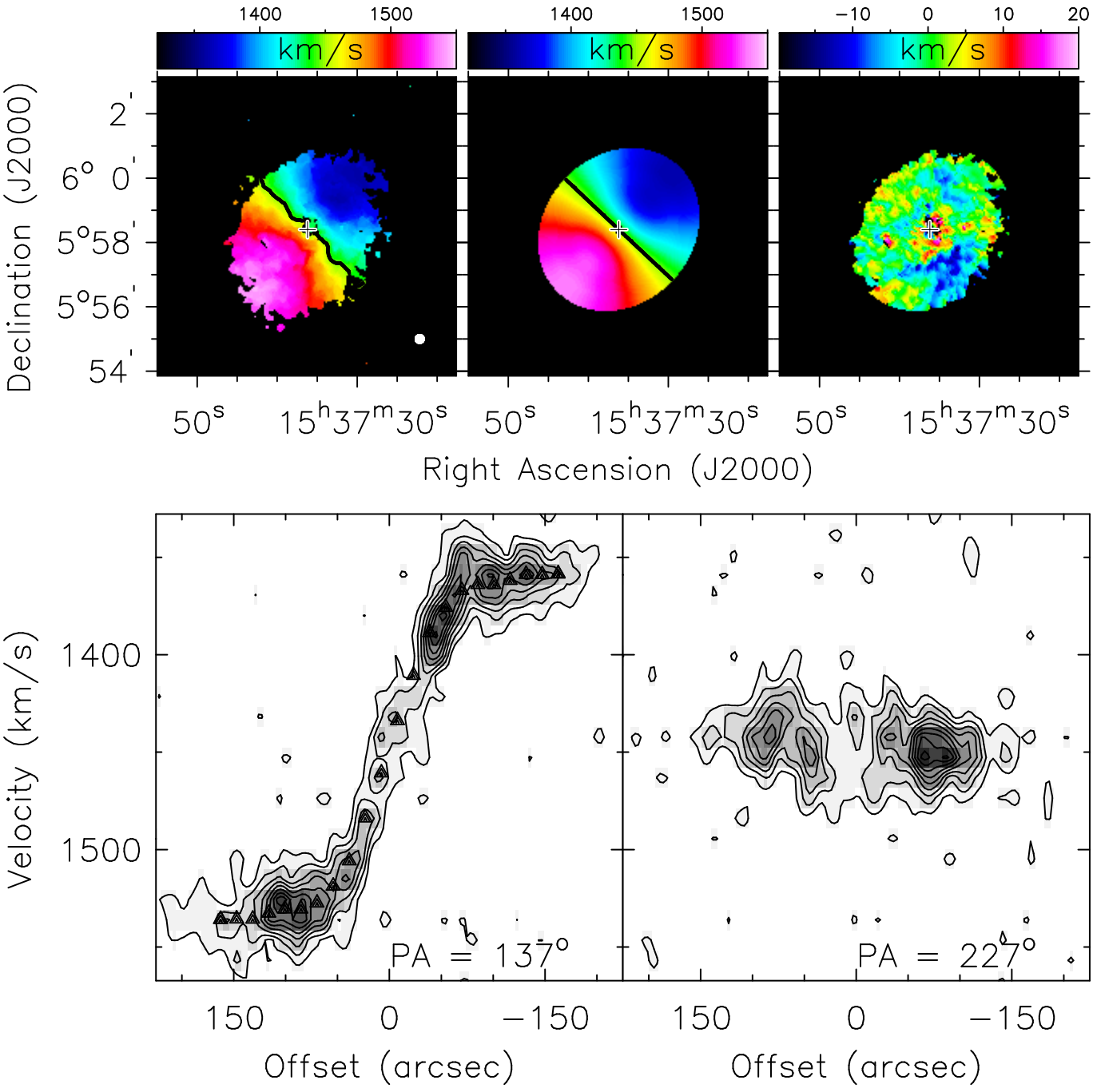

FIG. 43.— As in Figure 26, but for NGC 5964. The position-velocity diagram contours are from 1 mJy beam^{-1} to 10 mJy beam^{-1} in steps of 1 mJy beam^{-1}.

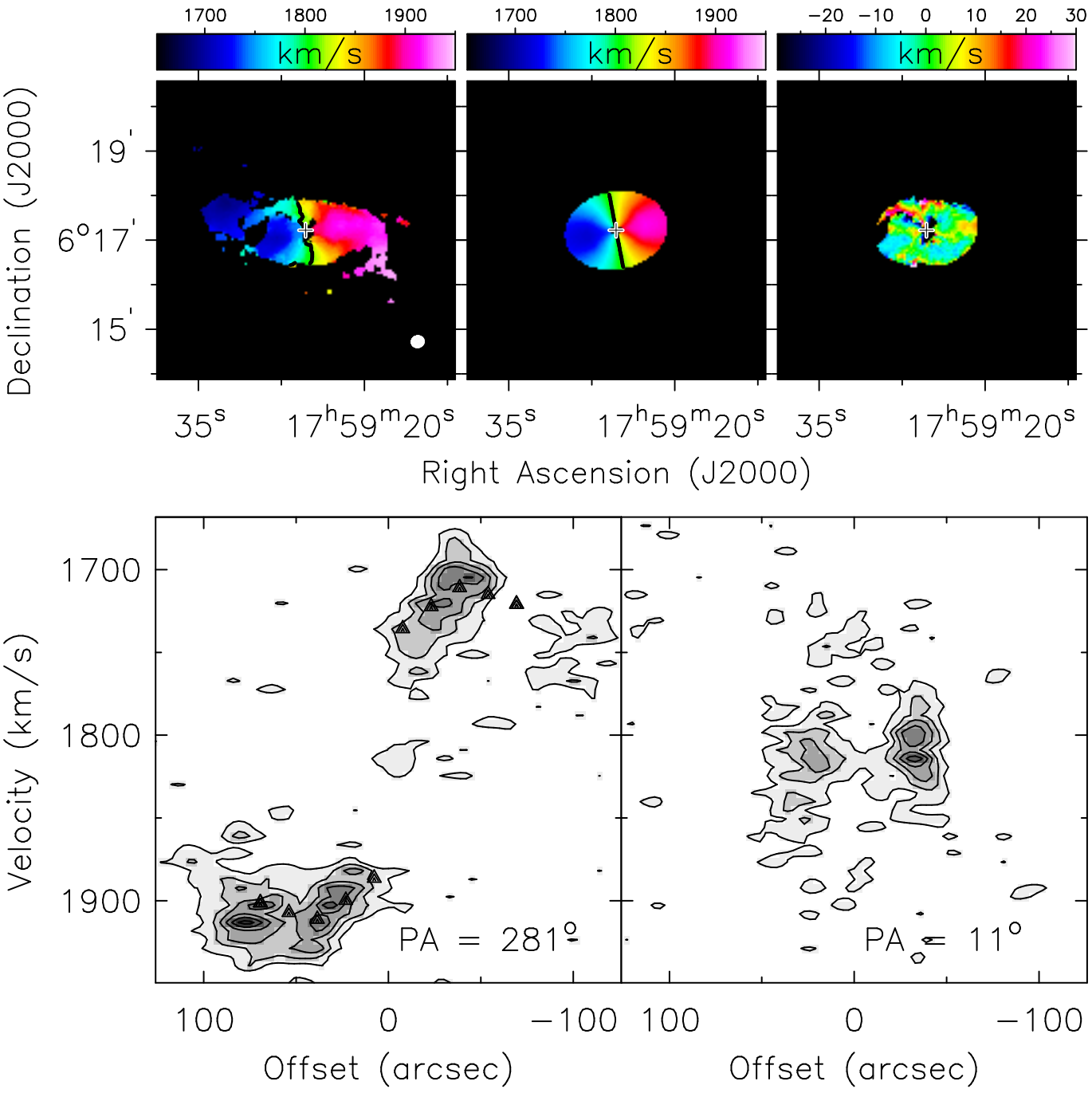

FIG. 44.— As in Figure 26, but for NGC 6509. The position-velocity diagram contours are from 2 mJy beam^{-1} to 15 mJy beam^{-1} in steps of 2 mJy beam^{-1}.

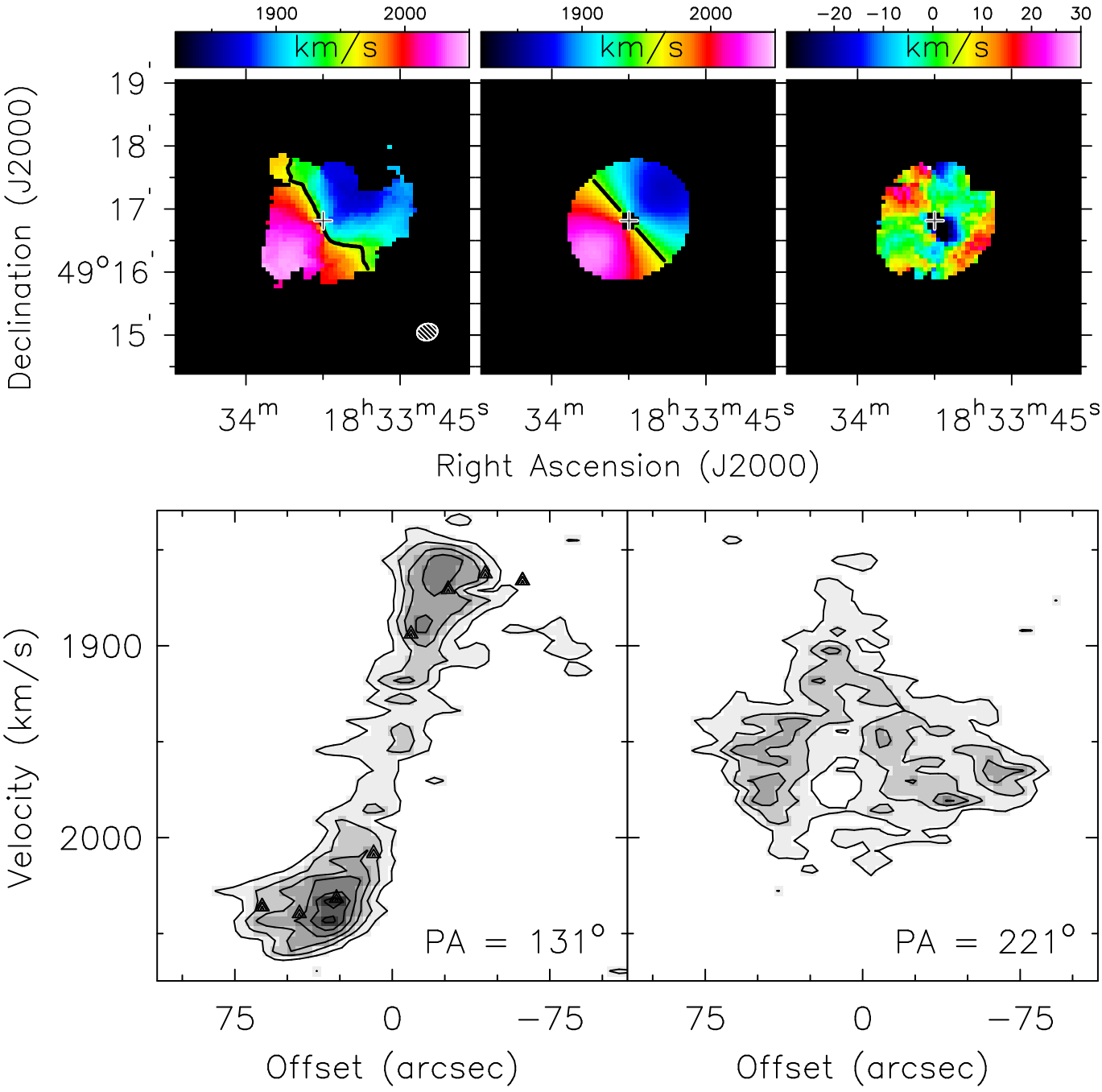

FIG. 45.— As in Figure 26, but for IC 1291. The position-velocity diagram contours are from 2 mJy beam^{-1} to 15 mJy beam^{-1} in steps of 2 mJy beam^{-1}.

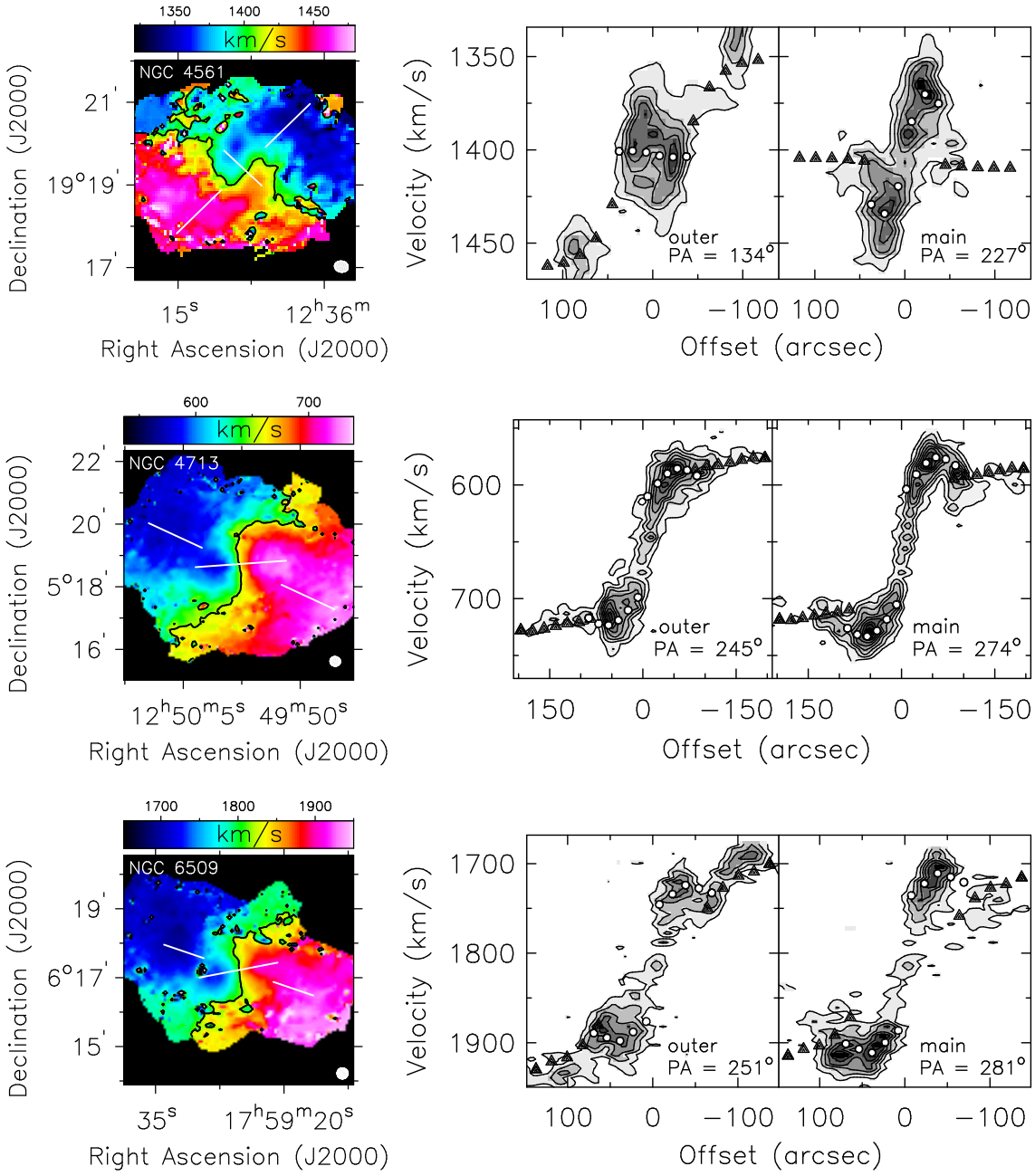

FIG. 46.— First-moment map (*left*) and position-velocity diagrams (*right*) showing the main and outer kinematic components in NGC 4561 (*top row*), NGC 4713 (*middle row*), and NGC 6509 (*bottom row*). These figures were created from the naturally-weighted data cubes that were blanked using the method described in Section 3.1. In the first-moment maps, the beam size is shown in the lower right corner, the black contour shows the systemic velocity of the outer component, and the white lines lie along the major axis of the main and outer components, over the range used in the rotation curve fits. The *middle* (*right*) *panel* of each row shows the position-velocity diagram along the major axis of the outer (main) component. Contours begin at 2σ and end at the maximum surface brightness along the major axis of the outer component plus 2σ, in steps of 2σ, where σ is the image noise. The projected titled ring model fit for the outer (main) component is overplotted as *black triangles* (*white circles*).